Politecnico
di Bari

Department of Mechanics, Mathematics and Management
AEROSPACE SCIENCES AND ENGINEERING
Ph.D. Program
SSD: ING-IND/04
AEROSPACE STRUCTURES AND DESIGN

Final Dissertation

Textile-Based Deployable Structures and Robotic Systems for Aerospace Applications

by
Alessandro Buscicchio:

Supervisors:

Prof. Prof. Maria Cinefra

Prof. Cataldo Guaragnella

Coordinator of Ph.D. Program:

Prof. Marco De Tullio

Course n°36, 01/11/2020-31/10/2023

Table of Contents

1. Introduction

Deployable structures represent a transformative approach to aerospace engineering, offering innovative solutions to challenges such as packaging constraints, launch vehicle limitations, and on-orbit assembly requirements. These structures, capable of compact storage and rapid deployment, have revolutionized spacecraft design and enabled ambitious missions beyond the confines of Earth's atmosphere. In this introduction, we delve into the evolution of deployable structures in aerospace applications, highlighting key missions that have utilized these structures and exploring novel research applications that leverage deployable structures, particularly in the context of origami-inspired designs. The development of deployable structures in aerospace engineering traces its roots to the early days of space exploration, where stringent weight and volume constraints necessitated compact and lightweight spacecraft designs. Deployable structures emerged as a solution to these challenges, allowing spacecraft components to be stowed in a compact configuration during launch and subsequently deployed into their operational configuration in space[1].

One of the earliest examples of deployable structures in aerospace is the solar array, which consists of panels that can be folded or rolled for launch and then unfurled to capture solar energy in space. Solar arrays have been integral components of numerous space missions, including the International Space Station (ISS) [2], the Hubble Space Telescope, and various planetary exploration missions. Another notable application of deployable structures is in the deployment of antennas and communication systems. Deployable antennas enable spacecraft to establish communication links with Earth and other spacecraft over vast distances, facilitating data transmission, navigation, and scientific observations [3].

Several landmark missions in space exploration have relied on deployable structures to achieve their objectives. For instance, the Mars rovers, including Pathfinder, Spirit and Opportunity, utilized deployable solar arrays to power their scientific instruments and communication systems while exploring the Martian surface [4]. The successful deployment of these solar arrays enabled the rovers to operate autonomously for extended periods, conducting groundbreaking research and providing valuable insights into the geology and climate of Mars. Similarly, the deployment of large deployable antennas has been instrumental in enabling global satellite communication networks, weather forecasting, and Earth observation missions. Satellites such as the Hubble Space Telescope [7] and the James Webb Space Telescope [6] have relied on deployable structures to position their sensitive instruments accurately and shield them from thermal fluctuations and debris in space.

In recent years, there has been a growing interest in leveraging origami-inspired designs for deployable structures in aerospace applications. Origami, the ancient art of paper folding, offers a rich source of inspiration for designing compact, lightweight, and mechanically robust structures suitable for space missions. One notable example of origami-inspired deployable structures is the NASA Innovative Advanced Concepts (NIAC) program's investigation into origami-based space telescopes. Researchers are exploring the feasibility of using origami folding techniques to pack large telescope mirrors into compact configurations for launch and then deploying them into their operational configuration in space. These origami-inspired telescopes have the potential to revolutionize space-based observations by enabling the construction of larger and more powerful telescopes than currently feasible with conventional deployment methods.

Furthermore, origami-inspired deployable structures are being explored for applications such as solar panels [7], solar sails [8], antennas, and lightweight structures for planetary habitats [9] and landers. By drawing inspiration from nature and traditional origami designs, researchers are pushing the boundaries of deployable structure technology and opening up new possibilities for future space exploration missions.

In summary, deployable structures have become indispensable components of spacecraft design, enabling ambitious missions and scientific discoveries in space. From solar arrays and antennas to telescopes and planetary habitats, deployable structures continue to push the boundaries of aerospace engineering. With ongoing research into origami-inspired designs, the future of deployable structures in space holds promise for even greater innovation and exploration.

This PhD dissertation encompasses a series of papers dedicated to the exploration of robotics, advanced manufacturing, and origami-inspired structures.

The first paper [10] introduces the FRET (Flexible Reinforced Electronics with Textile) technology. This technology, which combines rigid-flex electronics with textile, was initially developed by the authors at NASA-JPL for the PUFFER robot, a deployable small rover inspired by origami [11]. The paper offers an in-depth evolution and characterization of the technology employed for PUFFER, demonstrating the author's proactive approach in characterizing the technology and in identifying novel applications within the burgeoning space economy. The second paper unveils SolarCube [12], a deployable solar panel for CubeSats applications leveraging FRET technology. The third paper presents a deeper analysis of FRET modelling and material characterization [13]. The fourth paper highlights the author's significant contributions to the Mars2020 mission, specifically in the development of the ground support equipment for the robotic arms of the SCS (Sampling and Caching Systems) of the Perseverance Rover [14]. The last paper presents the work and research done in the field of cooperative robots, specifically for the DARPA SubTerrean challenge within the CoStar NASA-JPL Research Team [15].

The first year of my research was conducted at NASA-JPL in California, within the robotics group. The remaining two years of the research was carried out at the Polytechnic di Bari, in collaboration with Astradyne, an innovative startup co-founded by the author.

The author's research has made substantial contributions to the fields of robotics, advanced manufacturing, and origami-inspired deployable structures. The creation of FRET and SolarCube has broadened the horizons for space exploration. Furthermore, the author's involvement in the Mars2020 mission has laid a solid foundation for future Mars missions. The author's work has underscored the potential of origami-inspired structures in space applications and illuminated the ways in which robotics can be harnessed to pioneer new frontiers.

1.1. Puffer

Inspired by the versatility and efficiency of origami folding, researchers have explored the integration of deployable structures into robotic systems to enable compact storage, rapid deployment, and shape adaptability. One of the earliest applications of deployable structures in robotics is in the development of modular and reconfigurable robots [16][17][18]. These robots consist of interconnected modules that can fold and unfold to adapt their shape and size to different tasks and environments. Deployable structures enable these robots to transition between compact configurations for transportation and expanded configurations for operation, allowing them to perform a wide range of tasks with greater flexibility and efficiency.

Origami-inspired deployable structures have also found diverse applications in robotics, ranging from space exploration and disaster response to medical robotics and search and rescue operations. These structures enable robots to overcome obstacles, traverse challenging terrain, and access confined spaces that would be inaccessible to traditional rigid robots. One notable application of origami-inspired deployable structures in robotics is in space exploration missions. Deployable rovers and landers equipped with folding mechanisms can be compactly packaged for launch and then deployed into their

operational configuration upon reaching their destination. These robots can explore planetary surfaces, collect scientific data, and conduct experiments in remote and hazardous environments, providing valuable insights into the solar system and beyond.

In disaster response scenarios, deployable robots can be released quickly to search for survivors in collapsed buildings, rubble, or hazardous environments. These robots can navigate tight spaces, traverse uneven terrain, and manipulate objects to locate and assist victims, augmenting human rescue efforts and reducing the risk to rescue personnel.

Recent research in origami-inspired robotics has focused on developing novel folding mechanisms, materials, and control strategies to enhance robot performance and versatility[19]. By leveraging advances in materials science, additive manufacturing, and artificial intelligence, researchers are pushing the boundaries of what is possible with deployable structures in robotics.

For example, researchers are exploring the use of smart materials and actuators that respond to external stimuli to achieve self-folding and self-adapting capabilities in origami-inspired deployable structures [20]. By integrating these materials into origami-inspired structures, researchers aim to create systems that can autonomously adapt their shape and behavior to changing environmental conditions or task requirements. Furthermore, advancements in computational modeling and simulation techniques enable researchers to optimize the design and behavior of origami-inspired robots for specific applications. By simulating the folding process and mechanical behavior of deployable structures in virtual environments, researchers can identify optimal folding patterns, materials, and control strategies to maximize robot performance and efficiency [21].

In summary, origami-inspired deployable structures have emerged as a powerful tool for enhancing robot mobility, versatility, and functionality in diverse applications. From space exploration and disaster response to soft robotics and medical applications, these structures enable robots to navigate complex environments and perform tasks with greater flexibility and efficiency. With ongoing research and innovation, the future of origami-inspired robotics holds promise for even more transformative advancements in robot design and capabilities.
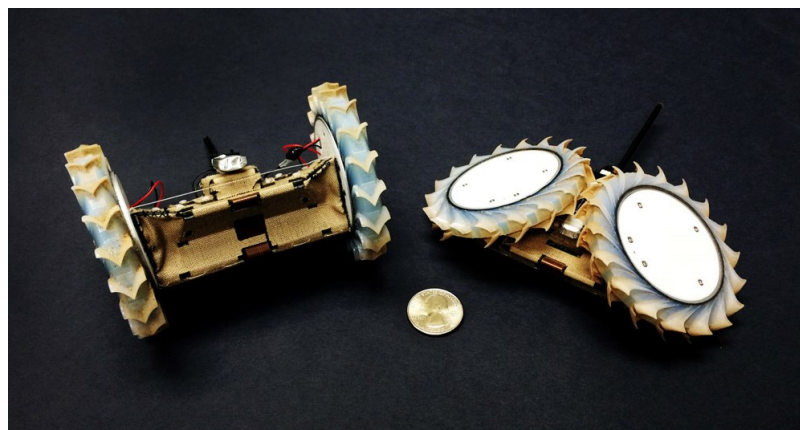
Figure 1-1: PUFFER Rover. Unfolded (left), folded (right).

To advance the robotics exploration and scientific mission in our solar system, in parallel to traditional missions to Mars, NASA has been initiating numerous R&D projects aimed at addressing the challenges faced by conventional robotic applications on Mars. One such initiative is the Pop-Up Flat Folding Explorer Robot (PUFFER) developed by NASA-JPL. PUFFER, shown in Figure 1-1, is a novel robotic explorer designed to overcome some of the limitations of traditional space exploration robotic systems. As a lightweight robot, PUFFER has the unique ability to flatten itself, retract its wheels, and navigate into confined spaces inaccessible to larger rovers. This capabilities where enabled by a novel design

and manufacturing techniques which combined rigid-flex PCB with Nomex textile, allowing the mechanical stresses to be decoupled from the electronics. The result was a robust and reliable electro-mechanical deployable body structure, as shown in Figure 1-2, that allowed the rover to be folded and unfolded several times without performance degradation. It has undergone rigorous testing in diverse and rugged terrains, ranging from the snowy hills of Antarctica to the arid Mojave Desert in California. PUFFER was conceived to operate alongside larger rovers or lander-deployed units, particularly in hazardous terrains. Given its compact size, comparable to the size of smartphone, multiple PUFFER units can be deployed to work cooperatively, thereby enhancing Earth science and future Mars and icy moon science mission concepts in ways a single rover cannot. PUFFER is outfitted with standard sensors and cameras capable of providing real-time environmental data, thereby enabling operators to make informed decisions.
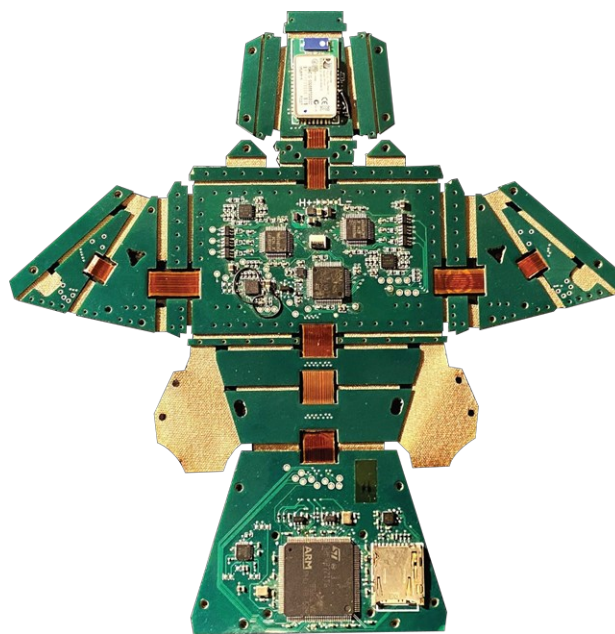
Figure 1-2 PUFFER Electro-Mechanical Body structure

Figure 1-3PUFFER – Project Evolution

In 2017, Alessandro Buscicchio, joined NASA-JPL as a visiting student from Politecnico di Torino. For his master's thesis in Mechatronics Engineering, he was tasked to design the motor controllers of the PUFFER. During his almost six years at JPL, Alessandro worked on several PUFFER's versions and learned to mastered PUFFER's unique electro-mechanical body technology. In the context of the PUFFER Rover, research had been instrumental in the development and testing of the rover's electronics. Additionally, the author delved into the integration and manufacturing aspects of

PUFFER's electro-mechanical body structure, which employs a novel composite material made of rigid-flex PCB and Nomex Textile. The research done on PUFFER, made the way to the creation of additional research project which where a natural evolution of the initial Rover, as shown in Figure 1-3. The PUFFER body structure technology, become one of the milestones of the author's PhD research since it laid the foundation for the realization of FRET technology.

1.2. Fret
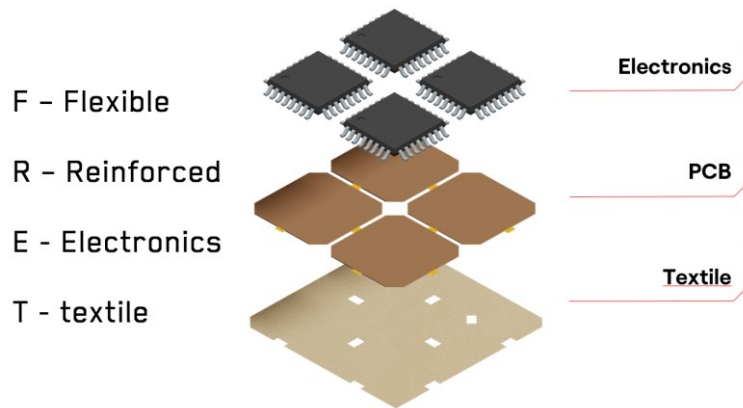
Figure 1-4 FRET Technology

Research on PUFFER has demonstrated how advanced manufacturing capabilities can revolutionize the construction of traditional systems. The innovative combination of rigid-flex PCB and Nomex textile has proven to be a versatile and reliable composite material. This material can create electro-mechanical deployable structures that serve dual purposes: acting as both the mechanical structure and the electronics and sensing device.
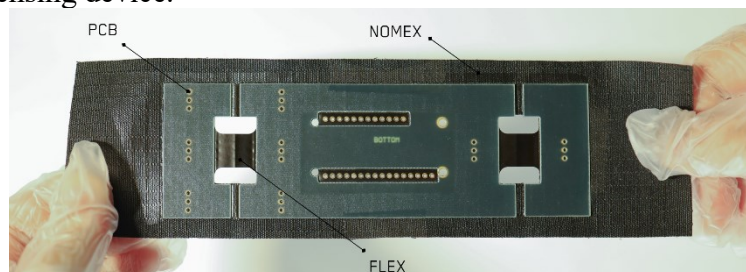
Figure 1-5 – Flat FRET structure

While PUFFER showcased the initial application of these technologies, it was the author's initiative to explore other fields of application that could benefit from such a groundbreaking electro-mechanical composite material. This material has been named FRET (Flexible Reinforced Electronics with Textile).
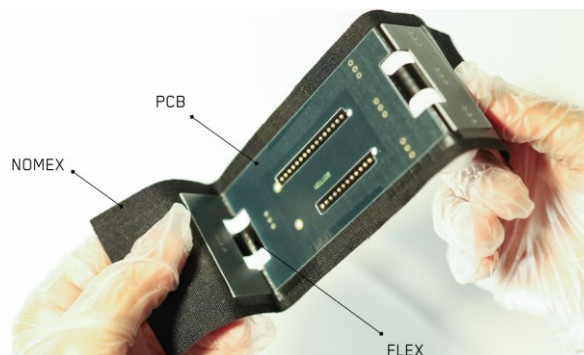
Figure 1-6 – Folded FRET structure

As shown in chapter 2 of this PhD thesis, the work describes an innovative technology enabler named FRET (Flexible Reinforced Electronics Textile), which solves the problem of design and integration of deployable, origami-inspired aerospace systems. FRET leverages two consolidated technologies, rigid-flex PCB electronics, and Nomex®, to create a new product that overcomes the limitations of its components and amplifies their strengths. One of the main challenges of this research has been to manufacture FRET in a reliable and reproducible way. The first attempt at creating FRET within the European supply chain was made possible through collaboration with the PCB manufacturing company ACB and Cibel Group in Belgium and France. The choice of ACB was influenced by the fact that FRET's applications are predominantly in the aerospace field. Therefore, it was crucial to select a industry partner already qualified for space-grade electronics. ACB is among a select few European companies certified by the European Space Agency to produce Rigid-Flex PCBs. Consequently, the collaboration with ACB has been instrumental in ensuring the scalability of FRET technology and its manufacturing method up to flight grade (or TRL 9).

1.3. SolarCube

The dawn of the 21st century has ushered in a new era in space exploration and technology, marked by the emergence of the New Space Economy, the proliferation of CubeSats for interplanetary missions (such as MarCO [22] in Figure 1-7), and the incredible advancements in robotics for space exploration. This convergence of innovation and ambition is reshaping our understanding of space, our ability to access it, and our prospects for expanding human presence beyond our home planet.
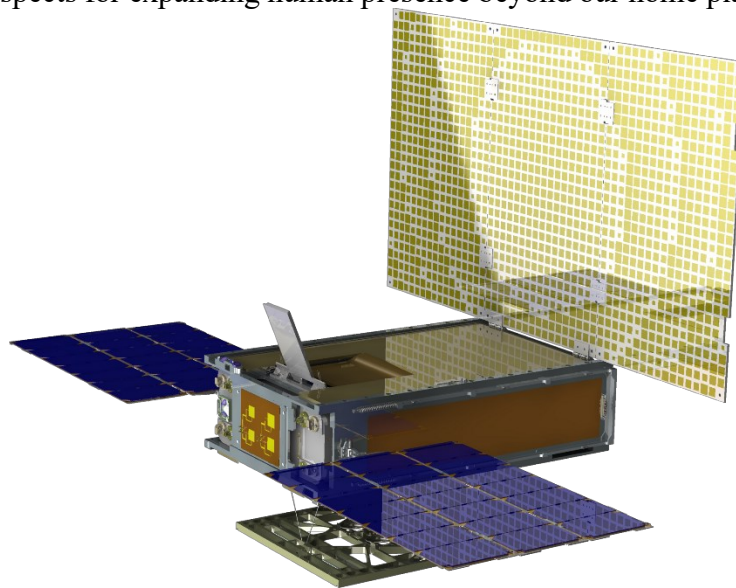
Figure 1-7 Mars Cube One (MarCO) 6U CubeSat.

The New Space Economy represents a paradigm shift in how we conceive, access, and utilize space. Traditional space exploration was once the exclusive domain of superpowers and government agencies, but now, a growing number of private companies are entering the arena. These companies are fostering a vibrant commercial space industry, reducing launch costs, and pioneering new business models in satellite services, space tourism, and resource utilization. This new economy is democratizing access to space, opening up opportunities for a diverse array of enterprises, and sparking unprecedented innovation.

One of the emblematic innovations in this era are the CubeSats, miniature satellites with standardized dimensions of multiple of 1 CubeSat unit (10x10x10 centimeters). CubeSats are becoming increasingly popular due to their affordability and flexibility, allowing academic institutions, startups, and even individuals to engage in space research and technology demonstrations [23]. These small satellites are leading to groundbreaking discoveries in Earth and space sciences, offering invaluable hands-on experience to the next generation of space scientists and engineers, and contributing to an ever-growing

presence in Earth's orbit. Furthermore, these satellites have been used by space agencies in conjunction with bigger spacecraft to provide additional telemetry data and images. Among them the most notable ones are indeed the MarCOs 6U CubeSats, shown in Figure 1-7, utilized for capturing and sending back to earth telemetry data of the NASA InSight spacecraft during its descent into the Mars atmosphere. The other one is the more recent LICIACUBE by the Italian Argotech which has been used to capture the impact on the NASA DART spacecraft into asteroid [24].
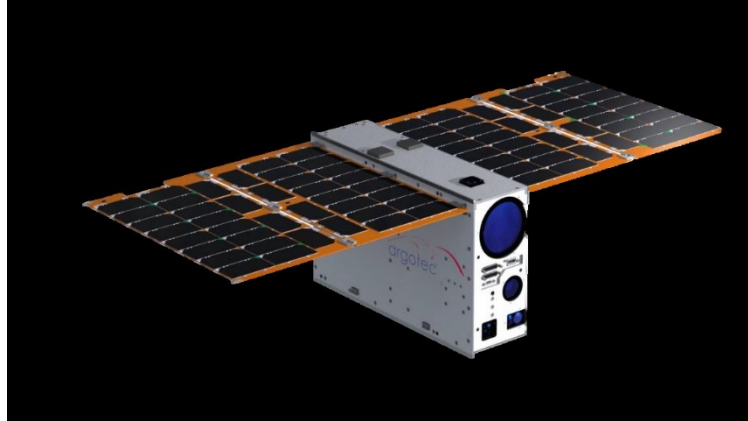
Figure 1-8 LICIACUBE Argotech 6U CubeSat

These tiny CubeSats are mostly powered by batteries and solar panels. When operating farther from the sun, such as on deep space missions, they need special deployable solar panels to collect the sun energy necessary for their survival and operation.

1.3.1. Deployable solar panels

The demand within the space market for compact systems capable of generating high power within confined dimensions is pressing. Power generation is pivotal in shaping satellite payloads, determining their characteristics, lifespan, and mission profile. However, the limited capacity for power generation often poses a substantial bottleneck, impeding ambitious and lucrative space activities.

Solar panels bear the responsibility of supplying power onboard spacecraft and are meticulously sized to meet spacecraft power requirements. The energy output of a solar panel is intricately linked to its surface area, emphasizing the significance of larger panels for generating substantial power. While small, low-power satellites can integrate solar panels directly into the main spacecraft body structure, more demanding missions, such as synthetic aperture radar (SAR) sensing, optical exploration, deep space ventures, and laser communication, rely on deployable solar panels to provide the necessary power-generating surface area.

Deployable solar panels must meet specific criteria:
- Compactness: Systems must align with the confined dimensions of rocket launcher fairings.
- Simplicity in design: The objective is to reduce system complexity and associated manufacturing time.
- Lightweight construction: Every kilogram launched into space incurs a substantial cost in thousands of euros.
- High performance: Systems should exhibit exceptional efficiency, power production, and an extended lifetime in the harsh space environment.
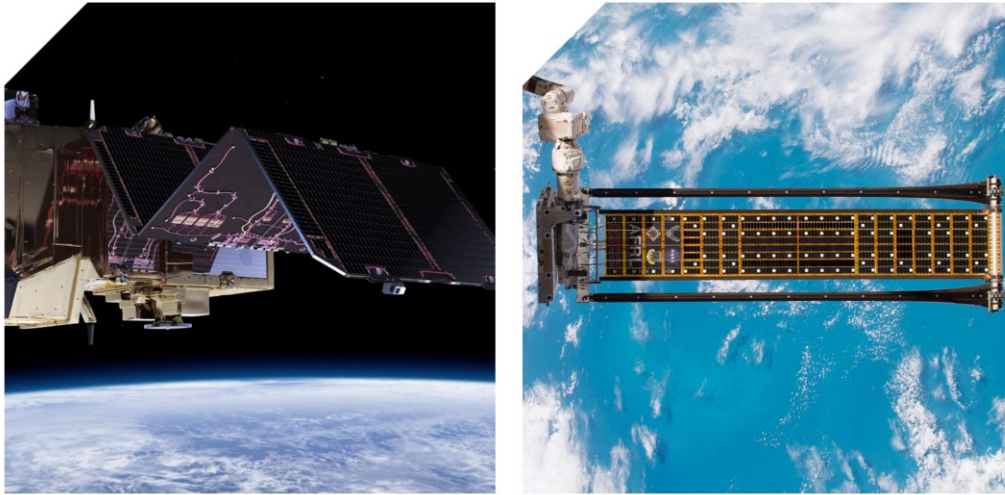
Figure 1-9 Rigid deployable solar Panels (left). Flexible deployable solar Panels (right).

There are two primary types of deployable solar panels: rigid and flexible. Flexible solar panels, although a recent addition to the market, are lightweight, compact, and boast efficiency comparable to rigid solar cells. However, their application is currently limited due to two main reasons. Firstly, the availability of flexible solar cells, primarily IMM solar cells, is limited on the market, with only a few manufacturers worldwide, such as Rocket Lab in the US. Secondly, the complexity of the deployment system associated with their unfolding limits their application to niche scenarios, primarily used for institutional research missions.

In contrast, rigid deployable solar panels represent a mature technology widely adopted in spacecraft. These panels, which use rigid solar cells, have demonstrated efficiency levels reaching up to 28-32%. They have established reliability in the challenging space environment, with several companies worldwide manufacturing space-grade rigid solar cells (e.g., Spectrolab US, CESI Italy, Azur Germany). Since the inception of space exploration, deployable rigid solar panels have been and continue to be the baseline solution for the majority of commercial satellites.

The meticulous design and precision engineering of deployable solar panels are imperative to withstand the harsh conditions of the space environment. Typical materials, such as lightweight composites like carbon fiber-reinforced polymers, strike a balance between strength and weight efficiency, chosen for their ability to endure the rigors of launch and space travel.

Manufacturing techniques for deployable solar panels involve creating robust mechanisms, hinges, and deployment systems. These must be engineered to ensure reliable stowage during launch and consistent deployment in orbit, aligning the solar panels optimally to capture sunlight for power generation.

Solar panels commonly employ triple-junction solar cells [25], known for high efficiency, durability, and radiation resistance. These cells, constructed with multiple semiconductor layers to capture a broad spectrum of light, and silicon solar cells, a well-established and reliable technology, remain popular for their proven performance in space.

Flexible solar cells, used in technologies like Roll-Out Solar Arrays (ROSA), employ thin, lightweight substrates that can be rolled and deployed. Emerging technologies, such as perovskite solar cells [26], have garnered attention for their potential for high efficiency and flexibility. While perovskite cells are still under development for space applications, they hold promise for future missions.

In conclusion, deployable solar panels for CubeSats and small satellites are integral components continually evolving alongside the broader field of space exploration. These panels play a pivotal role in powering compact spacecraft, facilitating a diverse range of scientific and technological missions. As materials, manufacturing techniques, and solar cell technologies advance, the future of deployable solar panels promises even greater efficiency and reliability, contributing significantly to the success of space exploration endeavors.

In Chapter 3, the author describes its research in the field of deployable solar panels which has led to the creation of SolarCube, an origami-inspired deployable solar panel for CubeSat applications leveraging the FRET technology. SolarCube has the main advantage of using textile material for its substrate, making it lighter and more compact than traditional deployable solar panels.

Figure 1-10 SolarCube Rendering. Stowed (left). Deploying (center). Fully Deployed (right).

Research activities, similar to the ones related to SolarCube, have been founded by ESA in the public call "100W DEPLOYABLE SOLAR PANELS FOR NANOSATELLITES", No. 4000133890/21/NL/MM/ra within the ARTES Advanced Technology programme, and have been carried out by the DLR [27] and De-Cubed[28]. Both solutions have leveraged origami-inspired solutions for packaging solar cells within 1U CubeSat volume and leveraged advanced manufacturing technologies for the solar array substrate.

1.3.2. The challenges of origami

SolarCube deployable solar panel relies on the origami pattern knows as the square flasher. In fact, within the vast world of origami, there exists a captivating and intricate pattern known as the "Squared Flasher." This remarkable design combines the principles of traditional origami with a touch of kirigami, producing a visually stunning paper creation that never ceases to amaze.

The Squared Flasher, as a specific origami pattern, has its roots in the broader world of modular origami. Modular origami involves creating complex structures by assembling multiple identical units. The Squared Flasher, in particular, evolved from the more basic Flasher model, which itself is a folded and cut design [29]. The Squared Flasher takes this concept to the next level by adding a grid-like pattern that further enhances its visual appeal. Over time, various artists and engineers have contributed to the development and diversification of the Squared Flasher pattern, resulting in a rich tapestry of variations and interpretations.

However, the transition from paper to engineering materials introduces a fundamental challenge known as the problem of thickness accommodation [30][31].

The problem of thickness accommodation arises from the stark difference in mechanical behavior between thin, flexible materials (such as paper) and thicker, less pliable engineering materials (such as metal, plastic, or composites). While origami patterns designed for thin materials fold with ease and precision, transferring these patterns directly to thicker materials often leads to structural integrity issues, undesired deformations, and difficulties in achieving the intended geometric shapes.

One of the primary challenges associated with thickness accommodation is the inherent stiffness of thick materials. Unlike paper, which readily conforms to intricate folds, thick materials resist bending and folding due to their stiffness, requiring higher folding forces and introducing stress concentrations at fold intersections. These stress concentrations can weaken the structure and compromise its mechanical integrity, posing significant challenges for engineering applications.

Furthermore, the mechanical constraints imposed by thick materials necessitate adjustments in fold angles, patterns, and techniques to ensure proper folding and functionality. Bulky fold intersections and manufacturing limitations further compound the challenge, requiring innovative approaches to optimize origami-inspired designs for thickness accommodation.

To address the problem of thickness accommodation in origami engineering, researchers and engineers employ a variety of approaches spanning materials science, mechanical engineering, and computational modeling. Material selection and modification play a crucial role in enhancing the foldability and flexibility of engineering materials, thereby facilitating their adaptation to origami-inspired designs. By choosing or modifying materials to optimize their mechanical properties, engineers can mitigate the challenges posed by thickness accommodation and improve the performance of origami structures.

Geometric adaptations represent another key strategy for overcoming thickness accommodation. By altering origami patterns and designs to accommodate thicker materials, engineers can minimize stress concentrations, optimize fold angles, and ensure proper folding without compromising structural integrity. Advanced manufacturing techniques, including laser cutting, 3D printing, and precision machining, offer additional avenues for addressing thickness accommodation challenges. These techniques enable the fabrication of complex origami structures with high accuracy and consistency, thereby facilitating the realization of origami-inspired designs in a wide range of engineering applications.

Computational modeling and simulation play a crucial role in the design and optimization of origami structures for thickness accommodation. By leveraging computational tools and simulations, engineers can analyze the behavior of origami structures under various conditions, predict their mechanical performance, and optimize their designs to meet specific requirements.

In conclusion, the problem of thickness accommodation poses a significant challenge for origami engineering, necessitating innovative approaches to adapt origami principles to diverse engineering materials and applications. By understanding the underlying causes of thickness accommodation and exploring potential solutions through interdisciplinary collaboration and advanced technologies, researchers and engineers can unlock the full potential of origami-inspired solutions across a wide range of fields. Through continued research and development, we can overcome the challenges posed by thickness accommodation and harness the transformative power of origami for future engineering innovations.

1.4. Mars Exploration

The Mars 2020 mission represents a significant milestone in planetary exploration, aiming to investigate the geology and habitability of Mars while paving the way for future human missions to the Red Planet. A crucial component of the Mars 2020 rover is its robotic arm, equipped with a suite of scientific instruments for conducting geological studies, analyzing samples, and collecting data to further our understanding of Martian history and potential for life.

The robotic arm of the Mars 2020 rover exemplifies the concept of deployable structures, as it can be stowed compactly during launch and transportation to Mars, then released and deployed upon arrival on the Martian surface. This deployable feature is essential for optimizing the spacecraft's packaging constraints within the limited confines of the launch vehicle while ensuring the arm's functionality and structural integrity during the mission.

The Mars 2020 robotic arm, as show in Figure 1-11, consists of several articulated segments, resembling a human arm, each equipped with motors, joints, and scientific instruments such as cameras, spectrometers, and a coring drill. These instruments enable the rover to analyze surface materials, collect samples, and conduct detailed geological studies to uncover clues about Mars' past environment and potential for life.
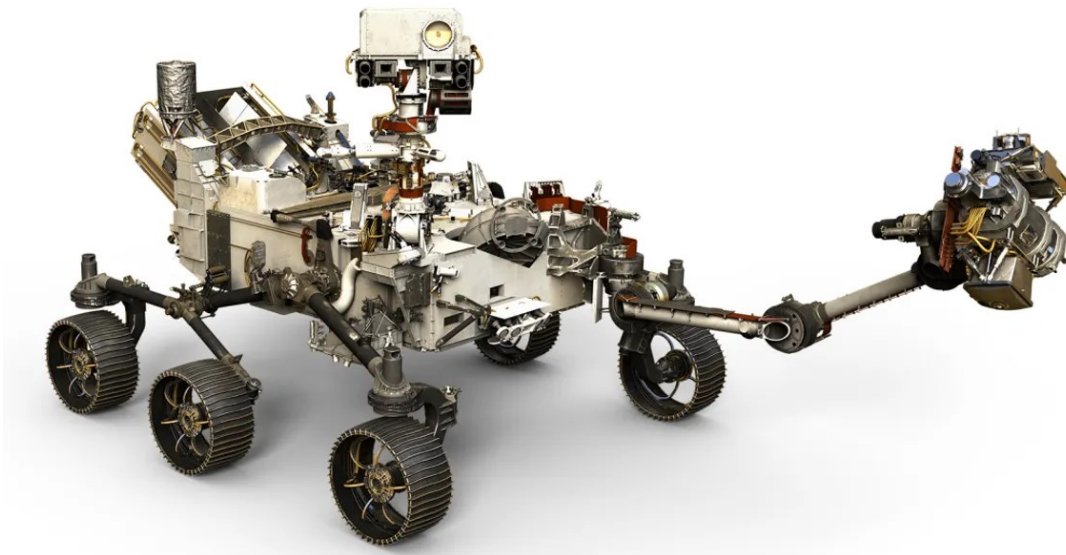
Figure 1-11 Mars2020 Perseverance Rover and Robotic Arm

During the journey from Earth to Mars, the robotic arm is securely stowed and restrained within the rover's structure to protect it from vibrations, thermal fluctuations, and other environmental stresses associated with space travel. Once the rover lands safely on the Martian surface, the robotic arm is released from its stowed configuration and deployed into its operational position, ready to begin its scientific mission.

The deployment process involves unfolding the robotic arm's segments and extending them to their full length, allowing the scientific instruments to reach and interact with the Martian terrain. Precision mechanisms and actuators control the movement and articulation of the arm, enabling it to position instruments accurately, collect samples, and manipulate objects with dexterity and precision.

The Mars 2020 robotic arm's deployable structure is a testament to the ingenuity and engineering prowess of the mission's team, enabling the rover to conduct groundbreaking scientific research and

exploration on the Martian surface. By incorporating deployable structures into the design of the robotic arm, engineers have optimized the spacecraft's functionality, efficiency, and adaptability, ultimately enhancing the mission's scientific return and advancing our understanding of Mars' past and present conditions.

In the context of my PhD work, I made significant contributions to the Mars2020 project, specifically in the developing the Electrical Ground Support Equipment (EGSE) for testing the Perseverance' rover robotic arms. Detailed description of the EGSE and its role in the mission's success is comprehensively detailed in chapter 4 of my dissertation.
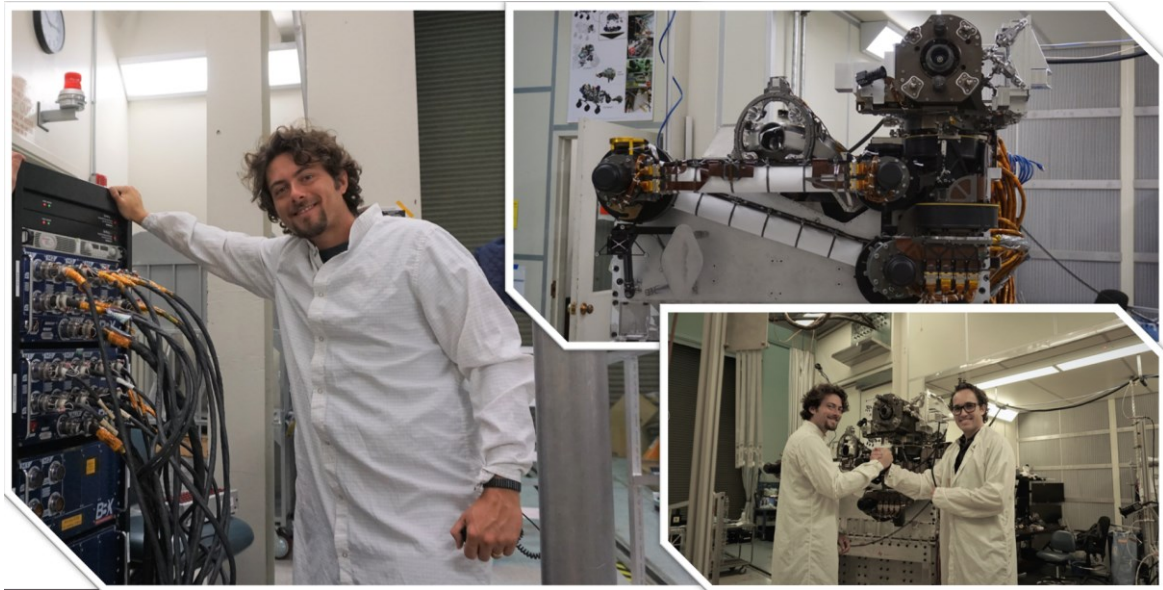
Figure 1-12 – The author troubleshooting anomalies on the MARS2020 Robotic Arm.

1.5. Underground Robotic Exploration

Autonomous robots have been increasingly instrumental in exploring uncharted territories on Earth, the Moon, and Mars. Surface exploration, whether through satellite observation or local ground and terrestrial robots, has long been the primary instrument for investigating unknown environments. Recently, however, focus has shifted to what lies beneath the surface, such as tunnels and caves. This dual scope, applicable to both Mars and the Moon, aims to explore natural caves and tunnels. On Earth, the development of autonomous robots for underground applications holds the potential to transform our exploration and interaction with subterranean environments. These advanced robotic technologies have a multitude of potential applications, including search and rescue operations, mining, civil applications, exploration techniques, mapping, and more.

It is therefore unsurprising that The Defense Advanced Research Projects Agency (DARPA) has initiated the Subterranean Challenge. This competition is designed to foster the development of autonomous robotic solutions for first responders in underground environments where GPS and direct communications are unavailable. The challenge encourages teams to showcase innovative approaches for robotic systems to swiftly map, navigate, and search complex underground environments, including man-made tunnel systems, urban underground, and natural cave networks. The objective of the challenge is to develop robots capable of autonomous operation in complex and dynamic environments, such as urban settings, mines, and caves, where human access is limited or impossible.

Figure 1-13 – Some of the NASA-JPL CoStar Autonomous and Cooperative Robots

The advent of autonomous robots for underground applications could revolutionize our exploration and interaction with subterranean environments. However, there is a pressing need for the development of new robotic architectures that enable robots to cooperate and operate autonomously in hostile environments. Recent advancements in system architecture, design, vision, and data technologies, such as artificial intelligence, the Internet of Things, communications, and signal processing, have facilitated the development of more advanced and intelligent robotic systems. In this context, there has been a growing interest in research and development for robotic and autonomous systems to enable their operation in volatile environments and to enhance their cooperative capabilities. These technologies and systems encompass areas such as perception, localization, locomotion and navigation, communication, and cooperative control and interactions. The DARPA Subterranean Challenge represents a significant stride towards developing autonomous robots capable of operating in complex and dynamic environments, and the work undertaken by NASA's JPL-led Team CoSTAR has been instrumental in paving the way for future advancements in this field.
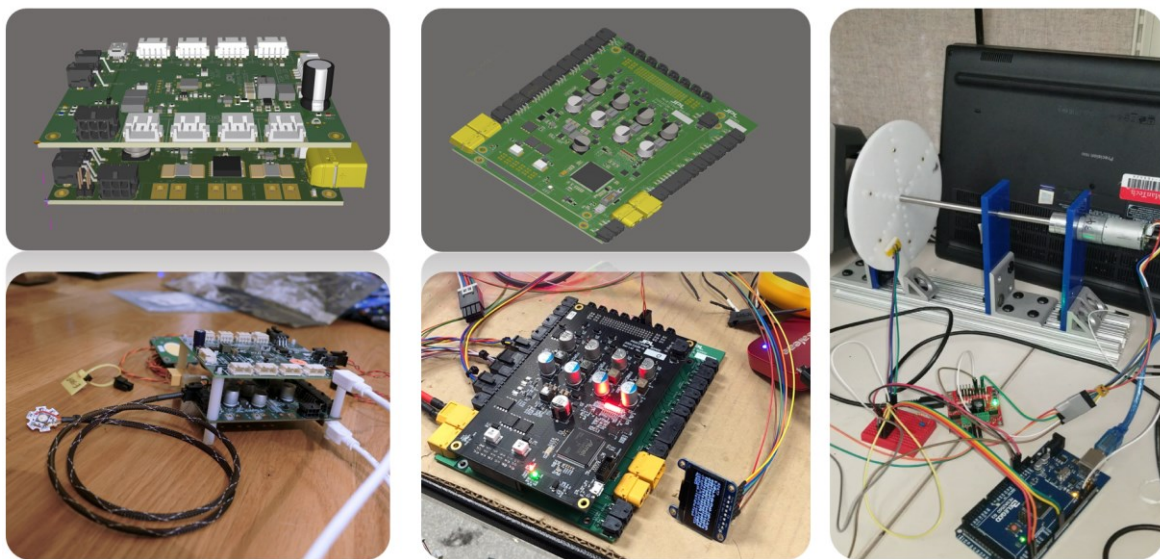
Figure 1-14 Some of the electronics Designd by the author for the CoSTAR DARPA Team.

NASA's Jet Propulsion Laboratory (JPL) has assembled a team of autonomous robots with diverse locomotion methods to compete in the intricate underground environments of the SubT Challenge, as shown in Figure 1-13. CoStar has achieved one of the most diverse robotic fleets. For instance, one of the robots, NeBula-Spot, employs a quadrupedal locomotion system to explore hard-to-access locations, while another robot, Rollocopter, utilizes a quadrotor system to fly or roll along on two passive wheels. The JPL-led Team CoSTAR (Collaborative SubTerranean Autonomous Robots) has demonstrated their collection of driving, walking, and flying robots that could potentially be used to explore extreme terrains on the surface as well as inside caves and lava tubes on other worlds without human assistance.

My PhD and research contribution to the NASA-JPL Team CoSTAR, has been in the development of the Nebula payload in which the author has investigated novel hardware architecture, distributed sensing technique and advanced communication and localization methods, as presented in chapter 6.

1.6. Reference

[1]   Kiper, Gokhan, and Eres Soylemez.""Deployable space structures"" In 2009 4th International conference on recent advances in space technologies, pp. 131-138. IEEE, 2009.

[2]   Spence, Brian R., Steve White, Matt LaPointe, Steve Kiefer, Peter LaCorte, Jeremy Banik, David Chapman, and John Merrill.""International space station (ISS) roll-out solar array (ROSA) spaceflight experiment mission and results"" In 2018 IEEE 7th World conference on photovoltaic energy conversion (WCPEC)(a Joint Conference of 45th IEEE PVSC, 28th PVSEC & 34th EU PVSEC), pp. 3522-3529. IEEE, 2018.

[3]   Abulgasem, Suhila, Faisel Tubbal, Raad Raad, Panagiotis Ioannis Theoharis, Sining Lu, and Saeid Iranmanesh.""Antenna designs for CubeSats: A review"" IEEE Access 9 (2021): 45289-45324.

[4]   Stella, Paul M., Richard C. Ewell, and Julie J. Hoskin.""Design and performance of the MER (Mars Exploration Rovers) solar arrays"" In Conference Record of the Thirty-first IEEE Photovoltaic Specialists Conference, 2005., pp. 626-630. IEEE, 2005.

[5]   Greenfield, Herbert T.""Appendange deployment mechanism for the Hubble Space Telescope program"" In NASA. Ames Research Center 19th Aerospace Mech. Symp. 1985.

[6]   Lightsey, Paul A., Charles Atkinson, Mark Clampin, and Lee D. Feinberg.""James Webb Space Telescope: large deployable cryogenic telescope in space"" Optical Engineering 51, no. 1 (2012): 011003-011003.

[7]   Shah, Syed Imran Hussain, Shahid Bashir, Mubashir Ashfaq, Ahsan Altaf, and Hatem Rmili.""Lightweight and low-cost deployable origami antennas—A review"" IEEE Access 9 (2021): 86429-86448.

[8]   Lappas, Vaios, Nasir Adeli, Lourens Visagie, Juan Fernandez, Theodoros Theodorou, Willem Steyn, and Matthew Perren.""CubeSail: A low cost CubeSat based solar sail demonstration mission"" Advances in Space Research 48, no. 11 (2011): 1890-1901.Xxx

[9]   Gruber, Petra, Sandra Häuplik, Barbara Imhof, Kürsad Özdemir, Rene Waclavicek, and Maria Antoinetta Perino.""Deployable structures for a human lunar base"" Acta Astronautica 61, no. 1-6 (2007): 484-495.

[10]   A. Buscicchio, D. Vittori, V. Netti, A. Troise, N. Mangialardi, D. Guaragnella, and M. Cinefra, "FRET (flexible reinforced electronics with textile): A novel technology enabler for deployable origami-inspired lightweight aerospace structures," in AIAA SCITECH 2023 Forum, 2023, p. 2081.

[11]   J. T. Karras, C. L. Fuller, K. C. Carpenter, A. Buscicchio, D. McKeeby, C. J. Norman, C. E. Parcheta, I. Davydychev, and R. S. Fearing, "Popup mars rover with textile-enhanced rigid-flex pcb body," in 2017 IEEE International Conference on Robotics and Automation (ICRA). IEEE, 2017, pp. 5459–5466.

[12]   A Buscicchio, G Alessandrino, A Troise, T Sironi, A Gloder, "SolarCube: An Origami-Inspired Lightweight Deployable Solar Panel for Nanosatellites", 2023 13th European Space Power Conference (ESPC), 1-9

[13]   Troise, A, Buscicchio, A, Netti, V, & Cinefra, M. "Finite Element Modeling on F.R.E.T. for Origami-Inspired CubeSat Applications." Proceedings of the ASME 2023 Aerospace Structures, Structural Dynamics, and Materials Conference. ASME 2023 Aerospace Structures, Structural Dynamics, and Materials Conference. San Diego, California, USA. June 19–21, 2023. V001T02A006. ASME.

[14]   Mier-Hicks, F., Buscicchio, A., Pailevanian, T., Elsdon, M., Sirota, A., Aguilar, E., Brooks, S. and Levine, D., 2022, March. "Electrical ground support equipment for the Sampling Caching System of the Mars 2020 rover". In 2022 IEEE Aerospace Conference (AERO) (pp. 1-12). IEEE.

[15]   Agha, Ali, Kyohei Otsu, Benjamin Morrell, David D. Fan, Rohan Thakker, Angel Santamaria-Navarro, Sung-Kyun Kim et al. "Nebula: Quest for robotic autonomy in challenging environments; team costar at the darpa subterranean challenge." arXiv preprint arXiv:2103.11470 (2021).

[16]   Haldane, Duncan W., Carlos S. Casarez, Jaakko T. Karras, Jessica Lee, Chen Li, Andrew O. Pullin, Ethan W. Schaler et al.""Integrated manufacture of exoskeletons and sensing structures for folded millirobots"" Journal of Mechanisms and Robotics 7, no. 2 (2015): 021011.

[17]   Hoover, Aaron M., and Ronald S. Fearing. "Analysis of off-axis performance of compliant mechanisms with applications to mobile millirobot design." In 2009 IEEE/RSJ International Conference on Intelligent Robots and Systems, pp. 2770-2776. IEEE, 2009.

[18]   Karakadıoğlu, Cem, Mohammad Askari, and Onur Özcan. "Design and operation of miniaq: An untethered foldable miniature quadruped with individually actuated legs." In 2017 IEEE international conference on advanced intelligent mechatronics (AIM), pp. 247-252. IEEE, 2017.

[19]   Rus, Daniela, and Michael T. Tolley. "Design, fabrication and control of origami robots." Nature Reviews Materials 3, no. 6 (2018): 101-112.

[20]   Felton, Samuel, Michael Tolley, Erik Demaine, Daniela Rus, and Robert Wood. "A method for building self-folding machines." Science 345, no. 6197 (2014): 644-646.

[21]   Zhu, Yi, Mark Schenk, and Evgueni T. Filipov. "A review on origami simulations: From kinematics, to mechanics, toward 19ultiphysics." Applied Mechanics Reviews 74, no. 3 (2022): 030801.

[22]   Schoolcraft, Josh, Andrew Klesh, and Thomas Werne. "MarCO: interplanetary mission development on a CubeSat scale." Space Operations: Contributions from the Global Community (2017): 221-231.

[23]   Chin, Alexander, Roland Coelho, Ryan Nugent, Riki Munakata, and Jordi Puig-Suari. "CubeSat: the pico-satellite standard for research and education." In AIAA Space 2008 Conference & Exposition, p. 7734. 2008.

[24]   Dotto, Elisabetta, Vincenzo Della Corte, Marilena Amoroso, Ivano Bertini, John R. Brucato, Andrea Capannolo, Biagio Cotugno et al. "LICIACube-the Light Italian Cubesat for Imaging of Asteroids in support of the NASA DART mission towards asteroid (65803) Didymos." Planetary and Space Science 199 (2021): 105185.

[25]   Takamoto, Tatsuya, Hidetoshi Washio, and Hiroyuki Juso. "Application of InGaP/GaAs/InGaAs triple junction solar cells to space use and concentrator photovoltaic." In 2014 IEEE 40th photovoltaic specialist conference (PVSC), pp. 0001-0005. IEEE, 2014.

[26]   Tu, Yongguang, Jiang Wu, Guoning Xu, Xiaoyu Yang, Rong Cai, Qihuang Gong, Rui Zhu, and Wei Huang. "Perovskite solar cells for space applications: progress and challenges." Advanced Materials 33, no. 21 (2021): 2006545.

[27]   Sproewitz, Tom, Patric Seefeldt, Siebo Reershemius, Marta Tokarz, Piotr Torchala, and Tim Kubera. "A Deployable Membrane-Based 100W Solar Array for SmallSats." In *2023 13th European Space Power Conference (ESPC)*, pp. 1-12. IEEE, 2023.

[28]   Pedivellano, Antonio, Thomas Sinn, Ambre Raharijaona, Michael Kringer, Joram Gruber, Thomas Lund, Alexander Titz et al. "PowerCube: Design and Development of a 100 W Origami-Inspired Deployable Solar Array for NanoSatellites." (2022).

[29]   Morris, Elissa, Daniel A. McAdams, and Richard Malak. "The state of the art of origami-inspired products: A review." In International Design Engineering Technical Conferences and Computers and

Information in Engineering Conference, vol. 50169, p. V05BT07A014. American Society of Mechanical Engineers, 2016.

[30]   Lang, Robert J., Kyler A. Tolman, Erica B. Crampton, Spencer P. Magleby, and Larry L. Howell. "A review of thickness-accommodation techniques in origami-inspired engineering." *Applied Mechanics Reviews* 70, no. 1 (2018): 010805.

[31]   Zirbel, Shannon A., Robert J. Lang, Mark W. Thomson, Deborah A. Sigel, Phillip E. Walkemeyer, Brian P. Trease, Spencer P. Magleby, and Larry L. Howell. "Accommodating thickness in origami-based deployable arrays." Journal of Mechanical Design 135, no. 11 (2013): 111005.

2. Paper #1. Fret (flexible reinforced electronics with textile): a novel technology enabler for deployable origami-inspired lightweight aerospace structures.

2.1. Abstract

Limited space inside the rocket requires payloads to be as compact as possible to satisfy mechanical constraints and optimize available space. For this reason, deployable mechanisms are essential for the payload design that otherwise would not be able to fit inside the rocket's cargo area. Stowed during launch and cruise, these systems are released and deployed once the rocket has reached its final destination. The present work describes an innovative technology enabler named FRET (Flexible Reinforced Electronics Textile), which solves the problem of design and integration of deployable, origami-inspired aerospace systems. FRET leverages two consolidated technologies, rigid-flex PCB electronics, and Nomex®, to create a new product that overcomes the limitations of its components and amplifies their strengths. The robustness and resilience of FRET enable the creation of reliable origami-inspired deployable structures. This is made possible by the unique mechanical properties offered by the textile material, which protects and reinforces the flexible joints allowing the implementation of reliable valley folds, which is the fundamental element for creating an origami folding pattern. Compared to traditional flex PCBs, FRET has shown significant mechanical robustness in bending cycles and tensile strength. An experimental method conducted on a prototype of FRET is presented to evaluate its tensile strength compared to traditional rigid-flex PCBs. Finally, an application of FRET for the design and manufacturing of lightweight origami-inspired solar panels is proposed.

2.2. Introduction

CUBESATS[1] [2], telecommunication satellites [3], observation satellites, and orbital telescopes all have in common deployable structures. Solar panels are the most common but also the most challenging from an engineering standpoint since their performance is directly proportional to their surface area. Stowed during launch, they need to deploy smoothly and reliably once the spacecraft has reached its orbit. Although many deployable solar panels have been proposed using rigid PCBs (printed circuit boards) [4] [5] [6], a technology enabler specifically realized to allow the design and manufacturing of lightweight origami-inspired structures was still missing. FRET (Flexible Reinforced Electronics Textile) allows origami-inspired patterns to be converted into reliable lightweight structures thanks to the unique properties offered by Nomex® textile materials combined with rigid-flex PCBs. Combined with rigid-flex electronics, the textile is well suited to support collapsible joints, known as valley fold, the fundamental element for developing origami-inspired structures. Polyimide, the most common material utilized for the fabrication of flex PCBs, is not well suited for the design of collapsible and origami-inspired structures since it cannot achieve acute bending radius. Such bending capability is essential to obtain valley and mountain folds. FRET allows the implementation of origami designs since the flex electronics are subject to lower mechanical stress and a smaller bending radius, making FRET structures much more resilient during folding, unfolding, and bending cycles.
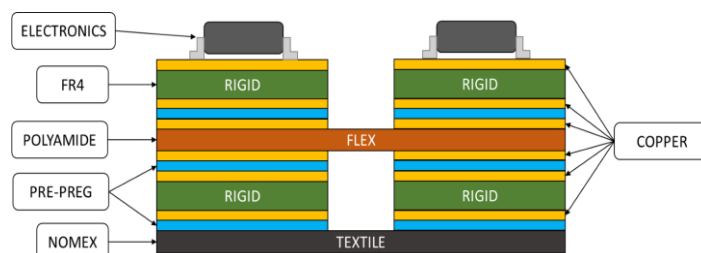

Figure 2-1 Example of 6 layers FRET rigid flex board
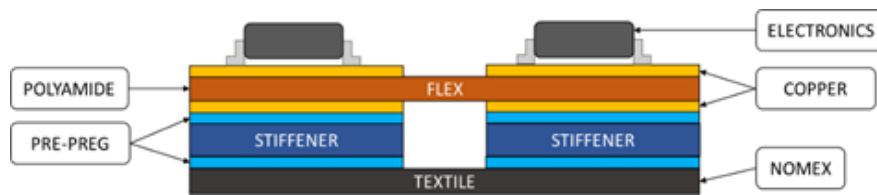
Figure 2-2 Example of 2 layers FRET flex board with stiffeners

2.3. Technology

2.3.1. Scientific and technical quality

Several technological challenges impede sensing and control of dynamic systems and deployable structures, specifically in the integration phases. State-of-the-art techniques mainly rely on two technologies: cabling and flex PCB. The issue with the former is that cables are heavy, challenging to integrate, and can get tangled during the system deployment and operation. On the other hand, while flex PCBs are lighter, thinner, and easier to integrate, they are subject to elevated failure rates due to the fragility of polyamide and copper traces under dynamic and cyclical loads. FRET solves these issues by combining two well-known and well-established technologies in the aerospace industry, namely rigid-flex PCB and flight-grade Nomex® textile material. This enables the integration of electronics into dynamic structures thanks to the unique mechanical properties offered by textile materials. The textile protects and reinforces the electronic components, specifically the flexible portions, increasing their robustness when bending, collapsing, and expanding. Since both rigid-flex PCB and Nomex® are vastly adopted in the aerospace industry, the technology readiness level (TRL) of FRET is estimated at TRL 5.

2.3.2. Innovation potential

Conventional rigid-flexible PCBs are made of polyimide-based material due to it is exceptionally flexible properties. Despite excellent tensile strength, it is very vulnerable to shear stress and tear propagation, specifically in the transition from a rigid to a flex area. Although silicones, hot-melt glues, and epoxy resins can be added to the flex-to-rigid joins to prevent tearing, their application needs to be done manually, increasing costs and manufacturing time. Furthermore, in applications where the flex is subject to continuous bending cycles, the copper is likely to suffer from hardening and fatigue, with severe consequences to the reliability of the circuit itself. For these reasons, today's flex PCBs are mostly adopted in quasi-static applications where conventional rigid-flex PCBs have mainly two complementary functions. The first is to affix electronic components in designated rigid locations, and the second is to provide reliable electrical connections between the component's terminals in a controlled manner. Typically the rigid portion of the PCB is fixed to a mechanical structure by screws, while the flex area is used to connect the electrical traces to other rigid areas or connectors. FRET overcomes these limitations because the integration of a textile layer into the PCB stack-up allows the mechanical and electrical functions of the rigid-flex joints to be decoupled, overcoming the limitations observed in the conventional polyimide-only flexures. With FRET, ideal joints, also known as valley and mountain folds, are implemented using very short textile sections, while the flex connections are implemented with a larger bending radius. A technology similar to FRET was prototyped at NASA Jet Propulsion Laboratory [7]. Initially created for the design and manufacturing of origami-inspired robots, this technology has further been investigated to solve both the electronics and sensor integration problem and the need for a technology enabler for the design and manufacturing of complex electro-mechanical lightweight origami-inspired structures. Although FRET leverages two existing and consolidated technologies, rigid-flex PCB electronics and Nomex® textile, the level of innovation

remains substantial since it creates a new product that benefits from both its primitives, overcoming their limitations and amplifying their strengths.
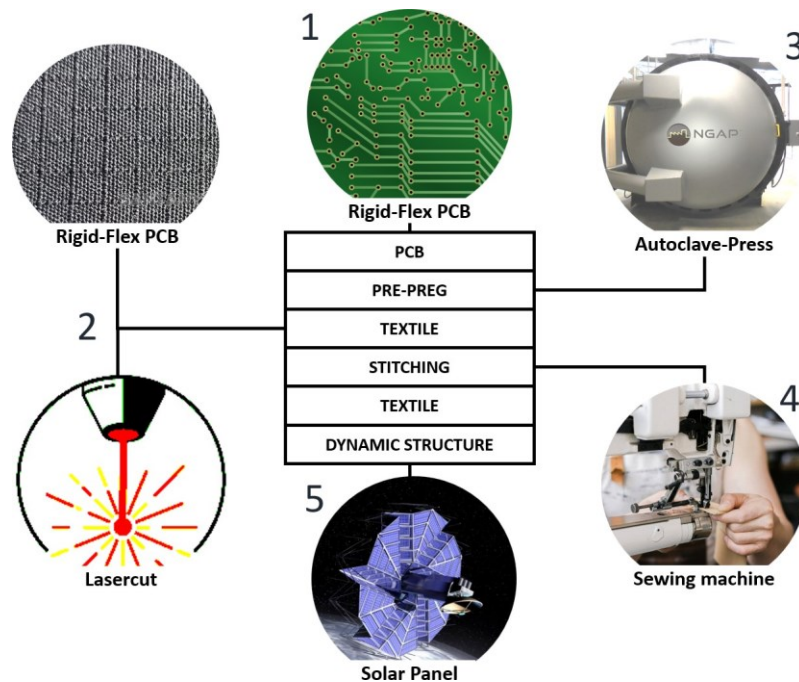
*Figure 2-3 **FRET manufacturing workflow***

Individually these two components have already been used for flight missions; therefore, the path to flight of FRET will be relatively short compared to entirely novel technologies. FRET represents a milestone to succeed in a novel integration of electronics and sensors within deployable and aerospace dynamic systems, especially in contexts that already leverage textile materials.

2.3.3.   Manufacturing

FRET's fabrication relies on the same tools and machines used for PCB manufacturing. The only addition is the laser cutter required to cut and shape the textile. The steps required to produce FRET are the following:

1) Rigid-Flex PCB is fabricated using the standard PCB manufacturing process.
2) The textile material is cut and shaped using a laser-cut machine.
3) PCB and Nomex® are bonded together using an adhesive prepreg material and either a high-pressure autoclave or mechanical press (both common machines in the PCB manufacturing Industry).
4) The obtained product produced with the FRET technology can now be used independently or easily integrated into a textile structure using stitching, bonding, and welding.

The possible Stack-up configurations are countless since conventional rigid-flex PCBs can count stack-up to 40 layers, figure 2-1 and 2-2 are an example of two FRET's designs. Figure 2-1 shows the stack-up of a six-layers rigid-flex PCBs, two rigid cores plus one flex core, where the textile is attached to the opposite side of the electrical components. Figure 2-2 shows a cheaper implementation of FRET using a two-layers flex PCB, with only one flex core, where stiffeners are attached to the bottom of the flex core to provide structural rigidity.

The typical thickness of a FRET stack-up ranges between 1 to 2 millimeters.

2.3.4. Prototype

Figure 2-4 shows an earlier FRET prototype. It was designed using FRET technology with the same stack-up illustrated in Figure 2-2. A flex layer is distributed over the whole PCB design while stiffeners are attached to the bottom layer to obtain rigidity. The textile is bonded to the top layer directly to the flex PCBs. Cut-outs are applied to the textile to expose the flexure and the electronics.

Figure 2-5 shows a detail of FRET's prototype when folded to obtain a valley fold. Mechanical stresses are absorbed by the textile (2), allowing the flex to have a more gentle bending radius (3). Electronics can be soldered directly on rigid areas (1).
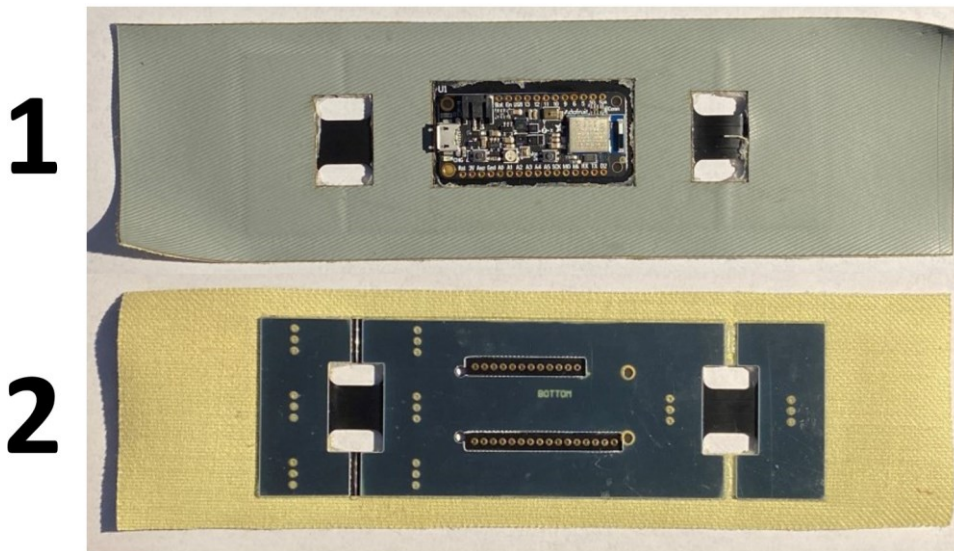
Figure 2-4 Earlier FRET prototype. 1) Top layer (textile attached to the top layer) 2) Bottom Layer.
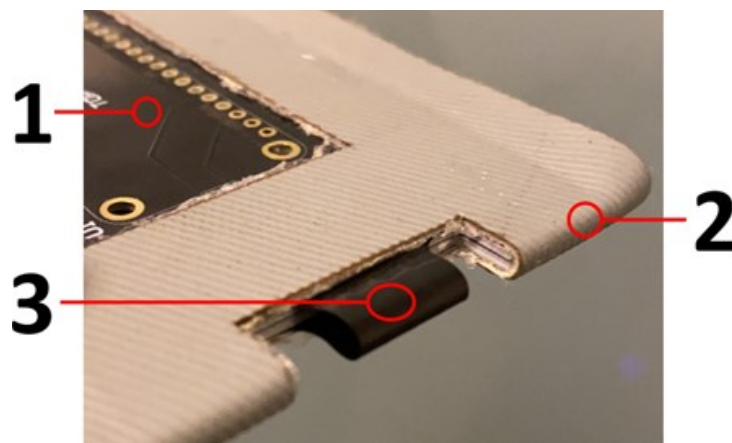
Figure 2-5 Folded FRET Prototype. 1) Electronics soldering pads. 2) Textile mechanical hinge. 3) Flex PCB.

2.3.5. Mechanical tests

Although FRET technology has already been tested for robustness over bending cycles [7], and similar solutions have been modeled to investigate the response to impact loads [8] or finite element analysis [9], the mechanical properties of FRET under tensional stress have not been tested yet. The main goal of the proposed tests is to demonstrate that FRET is more tolerant to tensile stress than a regular rigid-flex polyimide-based PCB. Nomex® nominal tensile strength is 340 MPa, while polyimide nominal tensile strength is limited to 231 MPa. The hypothesis is that FRET will maintain a nominal tensile strength similar to the Nomex® textile. The following mechanical tests have been conducted on FRET Prototypes:

· Pull mechanical stress test on Nomex® Ripstop Textile samples

- Pull mechanical stress test on Rigid-flex PCB samples
- Pull mechanical stress test on FRET samples

The proposed test is carried out by subjecting a specimen of standard dimensions of the material under examination to
an initially null uniaxial load F that is increased up to a maximum value that determines the rupture of the material. This procedure is used to highlight the different structural characteristics of the material under test, including mechanical strength (Rm), Young's modulus or modulus of elasticity (E), unit yield strength, percent elongation, and percent creep. The test consists of applying a displacement at a constant speed to the end of a test specimen, taking care to measure the elongation of the specimen and the tensile force applied. It ends with the breakage, i.e., the physical separation of the two ends of the sample. The breakage occurs under quasi-static conditions since the load is applied slowly, allowing, therefore, to determine the constitutive law of the material.

2.3.5.1. Test settings

A total of six specimens were tested for the uniaxial tensile test of FRET specimens:
- P0: Home-made specimen manufactured using a fabric with Nomex®-like characteristics
- P1, P2, P3: FRET specimen.
- P4, P5: Specimen consisting of the single Nomex® fabric suitably cut to verify the mechanical characteristics of the textile material.
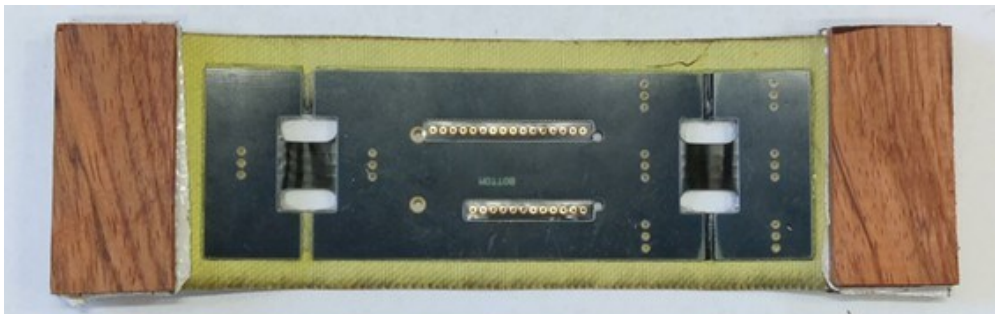
Figure 2-6 FRET specimen ready for the Tensile test

Figure 2-7 Traction test station

Since the thickness of the prototypes was insufficient to allow them to fit in the vice, small wooden boards were attached to the ends of each specimen to increase their thickness. The result can be seen in figure 2-6.

The tests were carried out at the University of Salento using the tensile and torsion testing machine "Instron 8850". A station consisting of a lamp and a camera was also set up at the foot of the machine to document the test as shown in figure 2-7.

In the setup, the machine was set to save data for each cycle with a sampling rate of 100Hz. Four samples have been tested with a displacement rate of 5mm/min (P0, P1, P2, P3).

2.3.6.   Analysis of results

The following outcomes resulted from the tests:

Considering the results obtained from the various tests, the following considerations can be made:

- P0: one of the two flexible parts of the PCB and the fabric has broken at the top wooden tab. Bonding resisted effectively even though the Bonding method is not usable for aerospace applications.
- P1: The adhesive used has broken down, causing the PCB to fall off, PCB and fabric intact. It has proved to be a failure because it broke under rather low tension.
- P2: Glue and PCB intact; the fabric is broken at the wooden tab. It has proved to be very strong, to the point of verifying the prior breakage of the fabric.
- P3: Intact fabric, breakage of the adhesive, and flexible part of the PCB at the bottom of the specimen. Despite having withstood higher tensile stress, it sustained considerable damage to the flexible part of the PCB.
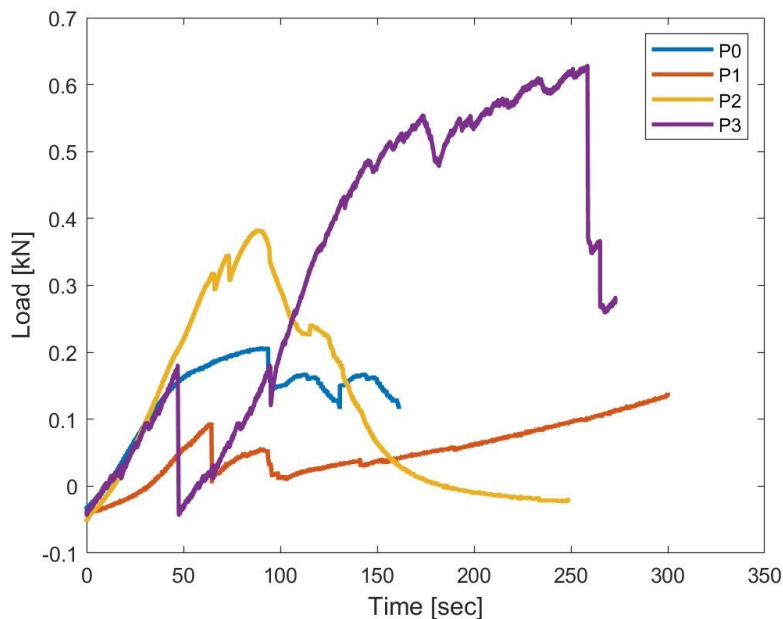
Figure 2-8 -Tension trend over time for the 4 FRET specimens tested

From the graph in Figure 2-8 we can see that the specimen that reaches fracture at the highest tension is P3. However, it should be noted that P2 is the only specimen on which both the PCB and the adhesive have been received intact.

In Figure 2-9 it is possible to visualize the photos of the samples after the completion of the tests.

The results obtained from the tensile tests showed the bonding procedure presents some weak points. In two specimens out of four, the detachment of the PCB from the fabric occurred. This, in any case, does not devalue the validity of FRET, which has all the potential to revolutionize electronics in aerospace, thanks to its applications for a new generation of deployable structures and integrated sensors. In fact, the inclusion of the textile material provides excellent strength to the entire FRET

structure. However, the results show the need for further investigation of the bonding phase to obtain a product with increased strength, and resistance, and to prevent delamination.

2.4. Space applications

FRET technology is a space technology enabler for electro-mechanical, origami-inspired deployable structures, such as solar panels, antennas, robotic systems, and more [10] [11] [12] [13]. The first application of FRET has been the PUFFER by NASA-JPL, an origami-inspired collapsible tiny rover for Mars Exploration [7]. This paper presents how FRET's technology could be used to design and manufacture deployable solar panels.

2.4.1. Deployable solar panels

Space-grade solar panels are sized to comply with the power budget and demand of the spacecraft. As a general rule, the energy produced by the solar panel is directly proportional to the solar panel surface area. Although in low-power satellites the solar panels can be directly installed on top of the Satellite's body, in more demanding applications, such as SAR, deep space missions, communication and laser applications, deployable solar panels are the only possible way to obtain large solar panel surface area. Several technologies have been proposed for the design and manufacturing of deployable solar panels, but they can be mainly narrowed down to two types: rigid and flexible solar panels. Flexible solar panels are a more recent technology, lighter and more compact, which leverages flexible solar cells. It has several advantages over rigid solar panels, but its application is mostly limited to government-founded research missions, such
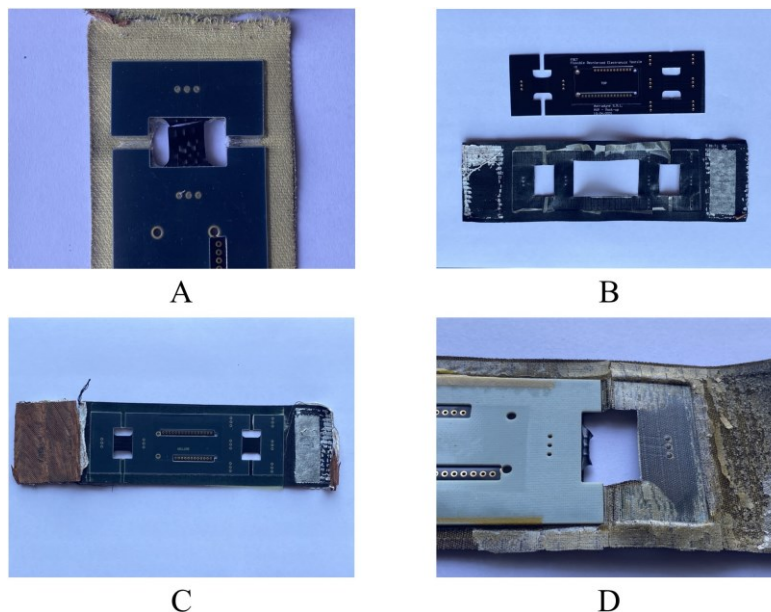
Figure 2-9 A) P0 Prototype The flex PCB break after tensile stress B) P1: Delamination of prototype after tensile stress test C) P2 prototype Successfully survive the tensile stress test D) P3: Break of the polyimide flex PCB and delamination after the tensile stress test

as international space station and deep space missions. Thus, its application in commercial spacecraft will continue to remain sparse in the immediate future. On the other hand, rigid deployable solar panels are the most consolidated technology which is used for the majority of spacecraft both in the private and public sectors. The main advantage of rigid solar cells is that they can reach an efficiency up 28-32%, their main drawback relies upon the weight. From a manufacturing standpoint, In rigid solar panels, strings of rigid solar cells are bonded to rigid honeycomb panels. The thickness and density of the honeycomb vary based on the particular solar panel design, configuration and application, it also

contributes up to 80% of the total mass of the solar panel. To allow rigid panels to fold on themselves in a stowed configuration, mechanical hinges are used, while a hard-drop-release mechanism keeps the system stowed during launch and then releases it once the spacecraft has reached space. The deployment can be obtained passively by spring elements or actively by electric motors both inserted inside the hinges. Furthermore, in order to connect the solar panels and relative sensors, such as temperature sensors, harnesses must be routed all along the solar panels and hinges. Malfunctions in the deployment mechanism, hinges and harnesses are among the main reason for solar panel failures in outer space. Despite the above limitations, deployable solar panels have been, and will continue to be, an essential key enabler for the majority of commercial and research spacecraft. For this reason, the research associated with this technology has been constantly pushed in order to reduce weight, size, efficiency and reliability. The main innovation of those technologies, investigated by all the major agencies, is represented by the application of origami-inspired patterns that could largely optimize the stowed-to-deployed area ratio of rigid panels and relative weight. For this reason, many types of deployable solar panels inspired by the origami technique have been proposed over the years, mostly by government agencies such NASA and ESA, but so far no solution made it to the commercial market due to technical constraints and elevated manufacturing cost. In this context, a technology enabler specifically designed to allow the design and manufacturing of lightweight origami-inspired structures, while maintaining it competitive in regard to rigid solar panels, was missing. FRET (Flexible Reinforced Electronics with Textile) is the so-far missing technology enabler, that does not require either a honeycomb or metal mechanical hinges and cables. For solar panels, FRET consequently permits the manufacturing of origami systems that can benefit from the most extreme and complex bending conditions. Origami-inspired patterns can be converted into reliable lightweight structures thanks to the unique properties of FRET, which combines Nomex® textile with rigid-flex PCBs.

2.4.2. Conclusions

This paper presents a novel technology enabler named FRET (Flexible Reinforced Electronics with Textile) and its unique electro-mechanical properties that allow the design and manufacturing of lightweight origami-inspired deployable structures. In the paper, mechanical tensile tests of some of FRET's prototypes are presented. Results show that it has been possible to successfully transfer the mechanical properties of the Nomex® to the flex PCB. In fact, the inclusion of the textile material provides excellent strength to the entire FRET structure. However, the results show the need for further investigation of the bonding phase to obtain a specimen with increased strength and resistance. Future developments planned for FRET include the realization of models based on finite element techniques to obtain more insights into the structural properties and potential of the technology. The analysis will aim the determination of the natural frequencies of the prototype with the objective of validating the results through experimental procedures. Moreover, a new traction testing phase must be carried out with the objective of reaching results statistically relevant, which will be used to numerically evaluate the properties of FRET.

2.4.3. References

[1]   Plaza, J. M. E., VilanVilan, J. A., Agelet, F. A., Mancheno, J. B., Estevez, M. L., Fernandez, C. M., and Ares, F. S., "Xatcobeo: Small Mechanisms for CubeSat Satellites Antenna and Solar Array Deployment," 2010.

[2]   Passaretti, M., and Hayes, R. D., "Development of a Solar Array Drive Assembly for CubeSat," 2010.

[3]   Ambrosini, C., Bellina, A., Bogo, L., Di Marco, S., Marconi, F., Netti, V., Soso, D., and Tesser, G., "SPRING DRIVEN EXPANDABLE REFLECTOR FOR DEPLOYABLE ANTENNAS," 2018.

[4]   Asundi, S., Mahin, M., Nagabhushan, V., Lin, T., and Fitz-Coy, N., "Composite and PCB Based Implementations of a Solar Panel Design for SwampSat," 2010. https://doi.org/10.13140/RG.2.1.2345.9040.

[5]   Bhattarai, S., Kim, H., Jung, S.-H., and Oh, H.-U., "Development of Pogo Pin-Based Holding and Release Mechanism for Deployable Solar Panel of CubeSat," *International Journal of Aerospace Engineering*, Vol. 2019, 2019, pp. 1–13. https://doi.org/10.1155/2019/2580865.

[6]   Park, T.-Y., Kim, S.-H., Kim, H., and Oh, H.-U., "Experimental Investigation on the Feasibility of Using Spring-Loaded Pogo Pin as a Holding and Release Mechanism for CubeSat's Deployable Solar Panels," *International Journal of Aerospace Engineering*, Vol. 2018, 2018, pp. 1–10. https://doi.org/10.1155/2018/4854656.

[7]   Karras, J. T., Fuller, C. L., Carpenter, K. C., Buscicchio, A., McKeeby, D., Norman, C. J., Parcheta, C. E., Davydychev, I., and Fearing, R. S., "Pop-up mars rover with textile-enhanced rigid-flex PCB body," *2017 IEEE International Conference on Robotics and Automation (ICRA)*, 2017, pp. 5459–5466. https://doi.org/10.1109/ICRA.2017.7989642.

[8]   Zhang, B., Shan, G., and Su, F., "Impact reliability analysis of a rigid-flex PCB system under acceleration loads," *Microelectronics Reliability*, Vol. 127, 2021, p. 114374. https://doi.org/10.1016/j.microrel.2021.114374.

[9]   Bell, J., Redmond, L., Carpenter, K., and de la Croix, J.-P., "Finite Element Modeling of Rigid-Flex PCBs for Dynamic Environments," *Journal of Microelectronics and Electronic Packaging*, Vol. 19, No. 1, 2022, pp. 25–38. https://doi.org/10. 4071/imaps.1655356, URL https://doi.org/10.4071/imaps.1655356.

[10]   Xu, Y., and Guan, F.-L., "Structure–electronic synthesis design of deployable truss antenna," *Aerospace Science and Technology*, Vol. 26, No. 1, 2013, pp. 259–267. https://doi.org/https://doi.org/10.1016/j.ast.2012.05.004, URL https://www.sciencedirect. com/science/article/pii/S1270963812000867.

[11]   *Bioinspired Origami: Case Studies Using a Keyword Search Algorithm*, International Design Engineering Technical Conferences and Computers and Information in Engineering Conference, Vol. Volume 10: 44th Mechanisms and Robotics Conference (MR), 2020. https://doi.org/10.1115/DETC2020-22228.

[12]   Arya, M., Lee, N., and Pellegrino, S., "Ultralight Structures for Space Solar Power Satellites," 2016. https://doi.org/10.2514/6. 2016-1950.

[13]   Kiper, G., and Söylemez, E., "Deployable space structures," 2009, pp. 131 – 138. https://doi.org/10.1109/RAST.2009.5158183.

3. Paper #2. Solarcube: an origami-inspired lightweight deployable solar panel for nanosatellites

3.1. Abstract

Deployable space structures have played a pivotal role in the past, and their significance will only grow in the future. They serve as a crucial facilitator for a wide array of cutting-edge space applications. This is particularly essential given the constraints imposed by the limited space available within a rocket's fairing, which restricts the size of the payloads it can carry. Among these deployable structures, satellite solar panels stand out as one of the most formidable challenges. The reason lies in the direct correlation between the surface area of these panels and the energy they can generate. In energy-intensive applications like Synthetic Aperture Radar (SAR), deep space missions, communication systems, and laser applications, the deployment of solar panels becomes the sole viable solution to attain a sufficiently powerful energy-producing surface while maintaining a compact form factor. This paper introduces "SolarCube," a groundbreaking deployable solar panel designed specifically for nanosatellites, drawing inspiration from origami principles. SolarCube is a commercially available solar panel unit that incorporates the ingenious flasher origami pattern. Remarkably, it can be comfortably accommodated within a 1U volume while possessing the capacity to power even the most energy-demanding 3U CubeSat platforms. Despite its foldable origami design, SolarCube leverages rigid triple junction solar cells, capable of producing approximately 70W of power in Low Earth Orbit (LEO), all while maintaining an estimated mass of under 0.8 kg. What sets SolarCube apart is its innovative design and manufacturing process known as FRET, which stands for "Flexible Reinforced Electronics with Textile." FRET seamlessly merges flexible electronics with textile materials, resulting in a solar panel that boasts an unprecedented resistance to bending, stretching, and folding cycles. This unique combination of origami folding techniques and FRET technology empowers SolarCube to achieve an exceptionally high stowed-to-deployed surface ratio. In this work, we present the concept and formulation of SolarCube, along with its preliminary design encompassing both the solar panel and its deployment system. Furthermore, we delve into the modeling and simulation of SolarCube using Finite Element Method (FEM) in stowed configuration. Finally, we propose a mission scenario aimed at evaluating the performance and thermal stability of SolarCube in real-world space conditions.

3.2. Introduction

The volume limitations given by rocket launchers, especially for small satellites, represent a key constraint for space structures, which have become more and more compact as technology progresses. A research topic that has been heavily influenced by these constraints concerns deployable space structures, which represent a key enabler for a wide range of innovative space applications. Deployable structures cover a wide range of implementations and are represented by many different technological solutions. This paper focuses on a deployable solar panel for a CubeSat application, called SolarCube. Conventional space-grade solar panels on the market are designed with solar cells mounted on rigid substrates and sized to the maximum dimension allowed by the spacecraft form factor and launcher constraints. The rigid panels can be folded on the satellite or on themself, in a stowed configuration, thereby deploying to their final size using mechanical hinges commonly operated by spring elements and release mechanisms. A drawback of this solution is that every single hinge of the panel potentially possesses multiple failure points. Moreover, deployable solar panels are connected electrically through wires and cables, which need to be properly routed to allow bending and to avoid tangling. Since multiple actuators, either active or passive, usually operate the deployment, this solution requires a perfectly synchronized action operated by a mechanically complex system. It can be concluded that conventional space-grade solar panels are (i) constrained in size and in the amount of

power that can be generated (ii) have complex subsystems with multiple failure points, and (iii) are heavy and bulky, due to the presence of the rigid substrate. SolarCube overcomes these problems and meets the increasing power needs of high-performing payloads, while also requiring less space and mass on the satellite unit.

3.3. SolarCube

3.3.1. Description

SolarCube, illustrated in Figure 3-1, is an origami-inspired lightweight deployable solar panel fitting inside the dimensions of one CubeSat unit (100x100x100mm).

It is characterized by an exceptionally high stowed-to-deployed surface ratio of 1:7, a thickness close to 1 mm, and an overall mass (including the deployment system) of less than 1 kg. These results can be achieved thanks to SolarCube's core technological enabler, FRET (Flexible Reinforced Electronics with Textile), that reinforces the flexible printed circuit boards (Flex PCBs) with flight grade Nomex® textile [1] [2]. Thanks to the properties of high-strength fabric materials such as Nomex®, FRET overcomes the crucial problem of the fragility of flex PCBs when applied to folding patterns. Through FRET, SolarCube will thus be the first deployable solar panel for the aerospace industry to use textile materials. Its stowed-to-deployed volume and mass will be unmatched amongst traditional solar panels, with weight savings estimated at 30%. Moreover, thanks to the larger surface to weight ratio, and therefore higher energy generated, SolarCube will support more power-demanding and higher-performing systems in space. SolarCube is based on a modified flasher square origami pattern, which has historically been considered one of the best origami patterns for solar panel applications due to its high stowed-to-deployed ratio.
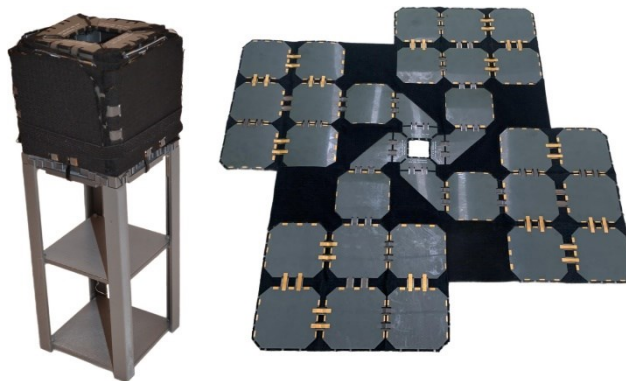
Figure 3-1 SolarCube mockup stowed (left) and deployed (right).

3.3.2. Manufacturing

SolarCube consists of an origami solar panel manufactured with FRET technology, a deployment system, an energy storage unit, and an electronics module as shown in Figure 3-2. SolarCube introduces a novel manufacturing and integration paradigm. As depicted in Fig. 3, FRET makes it possible to obtain the following advantages:

- COTS solar cells can be soldered directly onto the rigid area of the PCBs.
- Flex bridges provide robust electrical connections for all the solar cells.
- The textile material feels the gap between rigid parts, behaving as mechanical hinges and reducing the mechanical stress to the electrical flex bridges.

SolarCube is currently moving from TRL 3, proof of concept, to TRL 4, functional prototype. Fig. 4 shows some details of the SolarCube mockup which was built with representative materials in order to demonstrate the manufacturing process and the folding capability from planer to cubical. Furthermore,

Figure 3-4 shows the rigid PCB board used for qualifying and testing the footprint of two different solar cell models, the Azur TJ 3G30C 80x80 mm and a pair of CESI CTJ-LC 69x39 mm.
The functional prototype is currently in production and expected to be manufactured by the end of 2023.
The solar cells Azur TJ 3G30C, 80x80 mm, have been selected for this design since they offer a squared shape and an efficiency up to 30%.
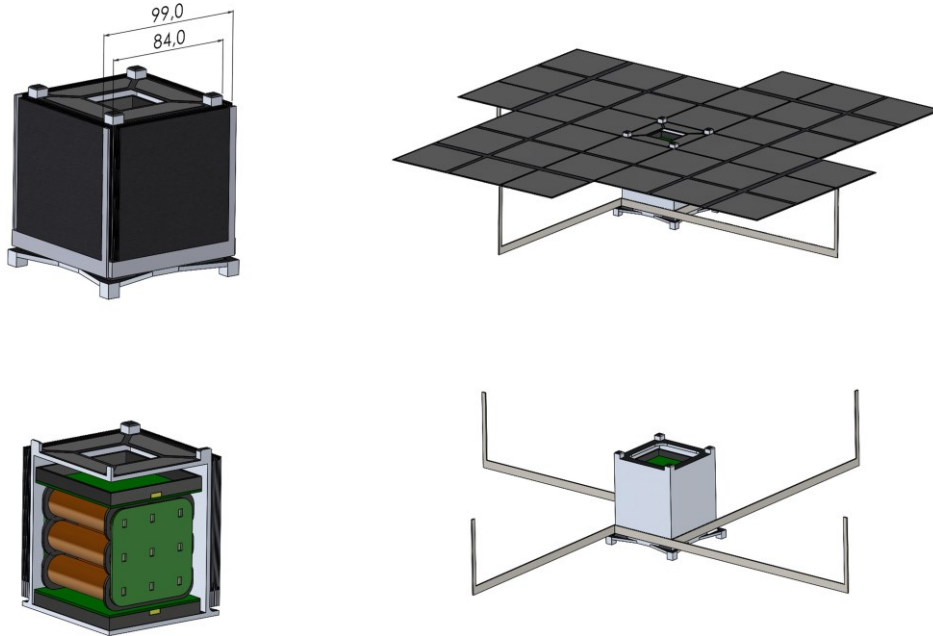
Figure 3-2 SolarCube stowed configuration (left top). SolarCube deployed configuration (right top). SolarCube internal components: electronics, batteries, and a release mechanism (left bottom). Preliminary concept of the deployment system (right bottom).
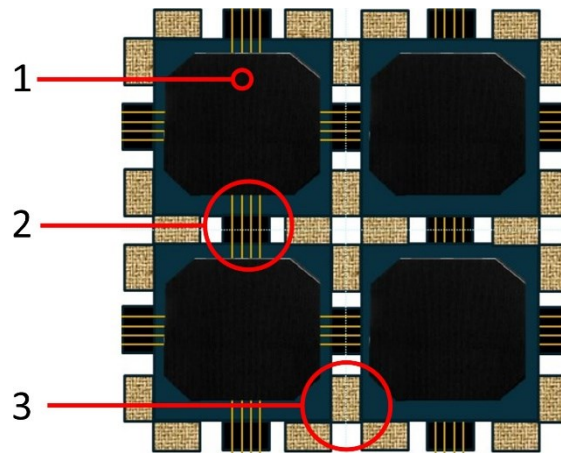
Figure 3-3 Some of the benefits of using FRET technology for the designing and manufacturing of SolarCube
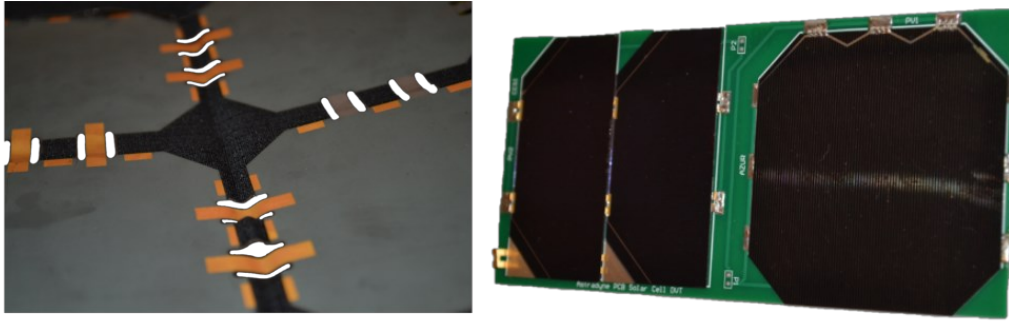
Figure 3-4 SolarCube textile substrate, with FRET technology (left) and a rigid PCB with space grade AZUR and CESI solar cells (right).

3.3.2.1.   Market analysis

Table 3-1 outlines some of the leading solar panel suppliers for Cubesats presently in the market, along with their competitive products in relation to SolarCube.

The four reported solutions (Endurosat, DCubeD, AAC Clyde Space, and MMA Design) are tailored for compatibility with 3U CubeSat modules. Similarly to SolarCube, these solutions feature deployment characteristics and stand out for their high power-to-mass ratios, ensuring remarkable performance within stringent spatial constraints. In particular, Endurosat's panel is extremely lightweight and compact in terms of volume, but offers modest performance. DCubeD's PowerCube, along with AAC Clyde Space's Photon-SD, ranks among the best products on the market in terms of the power-to-mass ratio. The former is compatible with a 1U CubeSat unit, but unlike SolarCube, it occupies the entire available volume of the unit. Regarding the second, the maximum power provided by Photon-SD is below SolarCube's performance. It is evident, therefore, how SolarCube's textile substrate allows for a reduction in the subsystem's weight compared to currently available market solutions, without sacrificing high power values. MMA Design's HAWK 17A-42, among the four mentioned, exhibits the highest specific power values (W/kg), offering a standard solution at 99W/kg and a high-performance option at 127W/kg. This latter value is in line with that of the SolarCube panel, excluding the deployment system.

Expanding the perspective to other solutions, an internal analysis highlights that SolarCube firmly positions itself well above the prevailing average of specific power values provided by the current solutions in the market. SolarCube's objective is to introduce a high-performance power generation system and secure a prominent position among the leading solutions in terms of power per kilogram. This achievement extends to reaching values of 100 W/kg when considering the deployment system.

Competitor	Mass [g]	Power [W]	Power density [W/kg]
SolarCube (Astradyne)	**515***	**66.5**	**129**
3U deployable solar array [3] (Endurosat)	270	8.4	31.1
PowerCube 100W [4] (DCubed)	1200	100	83.3
Photon-SD [5] (AAC Clyde Space)	310	27.8	89.5
HAWK 17A-42 [6] (MMA Design)	400	42	99-127

*Table 3-1 SOLARCUBE VS. SOME MAIN COMPETITORS. *Deployment system mass not included, it is currently under development.*

3.4. Structural analysis

3.4.1. Background on modal analysis

Vibration tests of satellite components are of paramount importance for determining relevant information about the assembly. They are carried out both on the individual components and on the whole structure depending on the specific case. Some of the most important considerations about vibration tests are enumerated below:

- They help to determine the frequency response of the structure for the attachment of electrical components.
- Allow to verify the structural reliability and assembly precision of bracing elements.
- Help check the functionality of release and deployment devices under dynamic loading.
- Permit the verification of the transfer coefficient not only under launch conditions but also for air or land transportation.

The satellite structure can be divided into primary, secondary, and tertiary components. The primary components constitute the "backbone" of the structure, supporting major loads and the launch vehicle adapter. The secondary components include the main sub-structures together with solar arrays and panels. Tertiary components assort all the connecting elements such as brackets and screws or rivets. Modal analysis is the analytical procedure of determining the natural frequencies of the device. It is necessary for the definition of the modes having the most relevant contribution to a forced vibration response.

3.4.2. Workflow

The model of the SolarCube unit in closed configuration was built in Solidworks and successively exported as a .step file in the Patran software. The analysis has been carried out only considering elements of the primary and secondary level and without the inclusion of the deployment system. The discretization procedure of the components in the finite element software was developed using tetrahedral elements with 10 nodes (Tet10). The characteristic dimension of the element was chosen to guarantee an acceptable aspect ratiofor the solver together with good accuracy of the analysis.
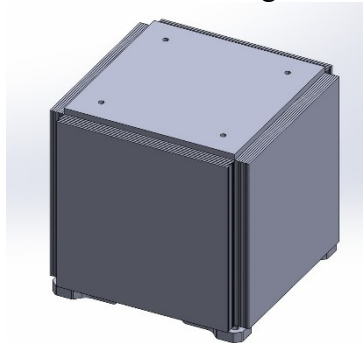
Figure 3-5 SolarCube CAD model in closed configuration. P.S. Deployment system not shown.

The number of elements in the closed model is equal to 23495 with 46206 nodes.
Figure 3-5 presents the model ready for import in the Patran software. The solar panel of the SolarCube is made of a FRET stack up, therefore the first layer of the textile is bonded to the PCB, and this was modeled through separated solids joined together with an ideal connection made through the node equivalencing procedure. In Patran environment, the properties and thickness of the Nomex® and the PCB were chosen following the results of a first campaign of mechanical tests of the substrate. The central hub to which the solar panel is bonded was considered to be made of an aluminum alloy 6061T6, commonly used for CubeSats.
The analysis was carried out after imposing as boundary conditions complete rotational and translational displacement constraints on the lower surface of the central hub.

3.4.3. Results of the modal analysis

The modal analysis yielded the frequencies present in Table 3-2. Here higher-order modes are referred to as "partial modes" since their modal shapes are complex combinations of bending and twisting around the various axes. The study highlighted natural frequencies in the range 19.0177 ÷ 71.1021, the first three modes are visible Figure 3-6.

Modal steps	Normal frequency [Hz]	Modal shape
1	19.0177	Twist on y axis
2	25.2452	Bend on y axis
3	27.9539	Bend on y axis
4	40.2545	Twisting
5	51.5869	Partial mode
6	54.9474	Partial mode
7	54.9474	Partial mode
8	61.3172q	Partial mode
9	66.4077	Partial mode
10	71.1021	Partial mode

Table 3-2 MODAL FREQUENCIES IN CLOSED CONFIGURATION

It could happen that experimental tests do not match the modal frequencies obtained from the simulations. In that case, the typical procedure consists of modifying the characteristic parameters of the materials until convergence, therefore avoiding jeopardizing the analysis carried out before the experimental results. A common reason for this phenomenon relevant contribution to a forced vibration response.

is the presence of residual stresses at a microscopic level in the structure. A benchmark value for the lowest modal frequency of the closed configuration is around 20÷40 Hz, the necessary value is a function of the typical frequencies of the launch vehicle. Considering the user manual of the Ariane 5 spacecraft, the closed CubeSat structure needs to have a fundamental lateral frequency of at least 10 Hz and a fundamental longitudinal frequency of at least 31 Hz.
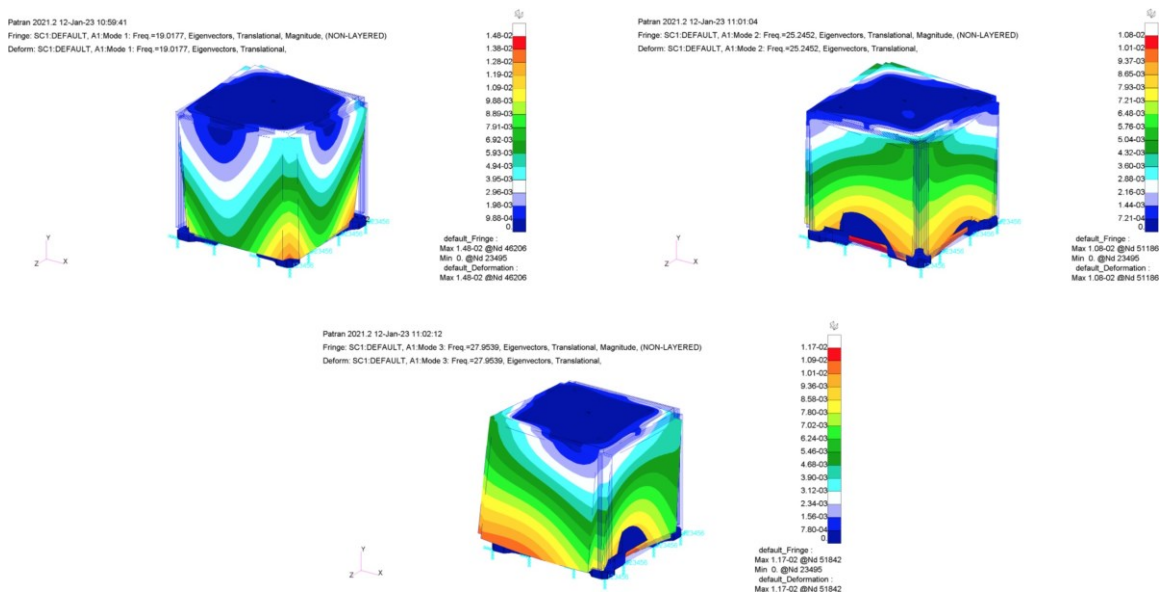
Figure 3-6 First three modes of the closed configuration.

3.4.4. Future steps for the structural analysis

In this section, the mechanical dynamical performances of a SolarCube unit were investigated by simulating the first ten natural frequencies of a hypothetical assembly of the solar array in its closed configuration. The results highlighted values inside the expected range and in line with the requirements obtained by the user manual of various spacecraft, used as a reference. To obtain these

results, a novel approach for modeling FRET technology had to be established due to the lack of previous dynamical simulation methodology. The modal analysis results are a key step to performing harmonic response analysis and dynamical stress (fatigue) analysis for the assembly. Future developments will be represented by simulations of the system in the deployed configuration and during the opening phase [7], to obtain precious information concerning the dynamical behavior of the structure.

3.5. Mission simulation

To compare the performance of SolarCube with those of the main state-of-the-art solutions currently in orbit, several simulations were carried out to effectively reproduce typical operational scenarios of Low Earth Orbit (LEO) missions based on 3U-sized spacecraft. In this instance, it was chosen to report the simulation related to the implementation of the SolarCube technology for a typical Earth Observation (EO) mission. Table 3-3 shows the main orbital parameters of the selected Helio synchronous operational orbit. The choice of the orbit is defined by the benchmark case, identified by the main operator in the field of 3U satellite constellations for EO missions.

Type	LTDN*	Altitude
Circular, Sun-Synchronous Orbit (SSO)	09:30 AM	515 km

*Table 3-3 ORBIT PARAMETERS. *Local Time at Descending Node.*

Within the simulations, the same attitude considerations are made: Nadir Pointing to maximize ground imaging quality and with Sun constraint to maximize the solar array area exposed to sunlight. Figure 3-7 shows a representation of the SolarCube in operational conditions.
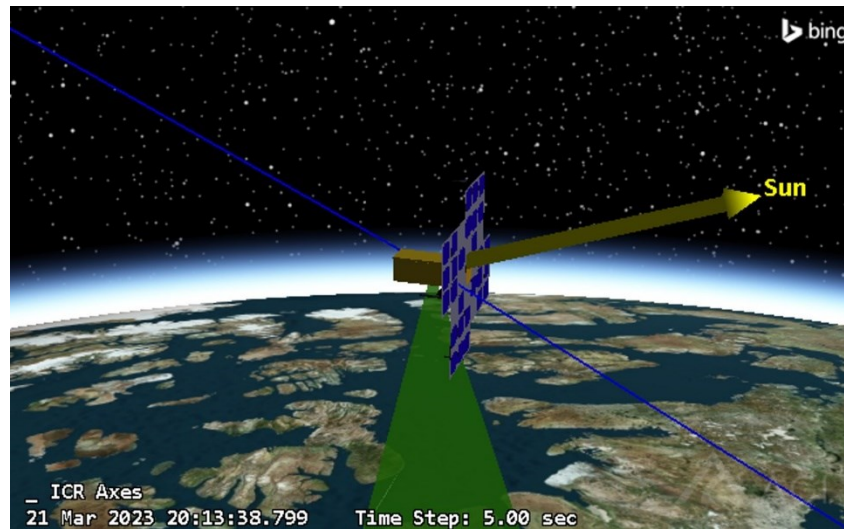
Figure 3-7 Visualization in STK environment of SolarCube during Earth Observation operation in LEO.

The benchmark satellite exhibits an effective power generation area of approximately $0.15 m^2$, which is inferior to that ensured by SolarCube, despite a simultaneous reduction in overall mass [8]. Table 3-4 reports the total energy produced by the array over one orbit period, while Figure 3-8 illustrates a comparison of the electric power generation trends between the benchmark and the SolarCube, considering the same period of the year.

	Total Energy Production	Δ
Benchmark	53.74 Wh	-
SolarCube	68.42 Wh	+27%

Table 3-4 Energy output over one-period orbit comparison

The advantage of implementing the FRET technology is unequivocal: the higher power density allows for a larger panel surface area, leading to an inevitable increase in the energy-producing area and, consequently, a higher number of solar cells. As shown by the simulation results, this guarantees an increase in power production and a boost of approximately 27% in total energy output.
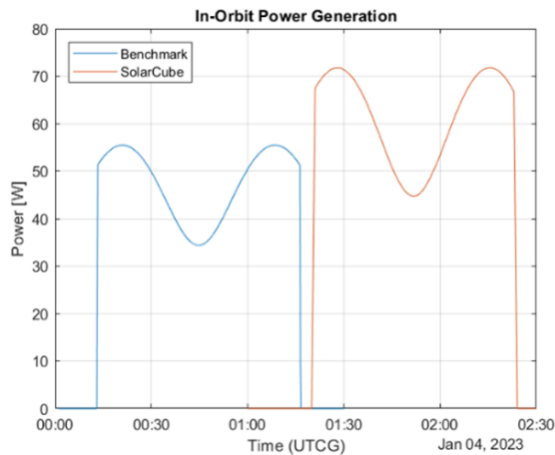
Figure 3-8 Visualization of In-Orbit Power Generation of SolarCube during Earth Observation operation in LEO.

In this example, the increased availability of power production and total energy can be translated into the adoption of more effective optical sensors (e.g. lower Ground Separation Distance), resulting in an enhanced quality of the captured images and consequent increase in their market value, thereby endowing the imaging constellation company with an inevitable competitive advantage. In general, the higher power to weight ratio achievable with SolarCube has the potential to revolutionize operational capabilities of nano satellites, opening the doors to payloads and missions that, as today, are tied to the bigger, more expensive and complex classes of satellites. Not only that, but the higher power availability on board leads to a greater computational capacity, which can be leveraged to introduce or enhance on-board data pre-processing capabilities, or to implement artificial intelligence systems aimed at realizing formation or swarm flight capabilities [9] [10] [11]. The latter represents a domain of research that is rapidly advancing, and its exponential growth is progressively enhancing the efficiency and effectiveness of micro and nano satellite constellations.

3.6. Thermal assessment

The thermal analysis is of utmost importance for the mission due to the following reasons:
- Ensuring mission feasibility: the thermal analysis proves that the mission is feasible from a thermal perspective, ensuring that the system can handle the temperature variations during all phases of the mission.
- Supporting design valuation: the analysis supports the valuation process during the design phase, providing crucial insights into thermal considerations for the spacecraft.
- Establishing environmental verification criteria: it helps define the criteria and parameters necessary for conducting environmental verifications.

The primary purpose of thermal control is to maintain the temperature of the entire system and its subsystems within the specified temperature limits throughout the mission phases. There are two types of temperature limits:
- Operational Limits: these define the temperature ranges that the subsystem or component should not exceed during operations.
- Survival Limits: these specify the range within which the component must be maintained, even when not in operation, to ensure its survival [12].

For reference, in Table 3-5 examples of typical thermal requirements for spacecraft components are listed [13].

In the specific case of the SolarCube panel, since it does not utilize conventional materials, being based on FRET technology, it is necessary to evaluate the operating and survival temperature ranges of each component material. Said ranges are listed in Table 3-6.

Components	Operational Range [°C]	Survival Range [°C]
Batteries	0 to 15	-10 to 25
Power Box Baseplates	10 to 50	-20 to 60
Star Trackers	0 to 30	-10 to 40
Gyros/IMUs	0 to 40	-10 to 50
Reaction Wheels	-10 to 40	-20 to 50
Antennas	-100 to 100	-120 to 120
C&DH Box	-20 to 60	-40 to 75
Solar Panels	-150 to 110	-200 to 130

Table 3-5 – Typical thermal requirements for spacecraft components

Components	Operational Range [°C]	Survival Range [°C]
Nomex®	-196 to 204	up to 370
Rigid-PCB	-120 to 130	-150 to 180
Flex-PCB	TBD to 180	TBD to 220
Pre-peg	up to 140	up to 170
Solar Cells	up to 110	up to 150
Glue	-105 to 150	-180 to 200

Table 3-6 Thermal requirements for SolarCube components

The Nomex® substrate's minimum operational temperature, as presented in the table, corresponds to the lowest temperature achieved during laboratory testing. This testing regime showcased exemplary performance characteristics. Although the tested sample differed from the Nomex® variant utilized as SolarCube substrate, the study revealed that the sample exhibited increased brittleness, yet maintaining an elongation at break of approximately 3% [14]. This retention rate outperforms the majority of inorganic materials at room temperature, underscoring Nomex®'s aptitude for cryogenic applications. Furthermore, additional substantiation of Nomex®'s robustness in low-temperature environments stems from the outcomes of NASA's MISSE missions, wherein no deleterious effects were documented in Nomex® fibers even under prolonged exposure to severely cold temperatures [15]. The maximum operational temperature is recommended by DuPont for prolonged and/or repetitive cycles, while the maximum survival temperature refers to the point beyond which the material starts to degrade rapidly [16].

For the rigid-PCB, the stiffener is made of an innovative multifunctional epoxy resin system, with a high-performance 180°C Tg (glass transition temperature) FR-4 design, tailored for the demands of multilayer Printed Wiring Board (PWB) applications where optimal thermal performance and unwavering reliability are paramount. This material is produced, incorporating the high performance multifunctional epoxy resin with E-glass glass fabric, ensuring exceptional resistance against Conductive Anodic Filament (CAF) formation. The stiffener material stands out for its exceptional thermal efficiency marked by a minimal Coefficient of Thermal Expansion (CTE), and its mechanical, chemical, and moisture-resistant properties not only match but exceed the capabilities of conventional FR-4 materials. The material's minimum operational temperature is not explicitly provided by the manufacturer. As a result, typical values for other high-performance FR-4s have been taken into consideration for the time being. The indicated temperature represents a threshold below which the material can develop brittle cracks and stress.

The flexible component of the rigid-flex PCBs is made of a double-sided, copper-clad laminate and an all-polyimide composite of polyimide film bonded to copper foil. This material system has been already

used in space applications due to its advanced performance, temperature resistance, and high reliability. In particular, it is designed to have higher maximum operating and glass transition temperature with respect to other polyimide flexible laminate products. No data is provided by the manufacturer regarding minimum operating and survival temperature. Future investigation and thermal cycling testing needs to be carried out on the material to determine the loss of flexibility and eventual cracks appearing due to prolonged low temperature exposure.

The connection between the rigid-PCBs and the Nomex substrate is established using a low-flow epoxy pre-preg, specifically formulated for bonding multilayer epoxy rigid-flex circuits or affixing heat sinks to multilayer epoxy PCBs. With an elevated glass transition temperature of 170°C, this pre-preg is well-suited for demanding high-performance and high-temperature scenarios, outperforming standard epoxy low-flow alternatives.

Regarding the adhesive used to bond the solar cells and the rigid PCB, data reported refers to a widely used in space applications low-outgassing silicon-based rubber. It's important to note that the manufactor's datasheet for this adhesive specifies the glass transition temperature, and thus the minimum survival temperature, as -105°C, whereas databases from space agencies report a usage temperature range with a lower margin down to -180°C.

3.7. Model Characterization

The thermal analysis is performed using Thermal Desktop (TD), software developed by Cullimore and Ring Technologies, utilizing a FED (Finite Difference Method) thermal model of SolarCube. To determine radiation interchange factors between surfaces and energy absorbed on spacecraft external surfaces, the Monte Carlo approach is employed. The model uses optical and thermophysical properties of the constituent materials, summarized in Table 3-7 and Table 3-8 [17] [18].

Name	Conductivity [W/mK]	Density [kg/m3]	Specific Heat [J/kgK]
Al7075	173	2810	960
Rigid PCB	0.4	1900	1200
Solar Cell	64	5323	322
Nomex®	0.25	433	1256
Stainless Stell	17	7750	480

Table 3-7 Thermophysical properties

Name	Solar Absorptivity	IR Emissivity
Al7075 Alodine	0.30	0.10
Al7075 Anodized	0.65	0.88
Rigid PCB	0.40	0.90
Black Painting	1	1
Solar Cell	0.90	0.80
Stainless Stell, Polished	0.37	0.075

Table 3-8 Optical properties

The spacecraft's surfaces are represented using Finite Difference elements. The mesh's edge nodes are distributed on the surfaces, with the number chosen to strike a balance between analysis accuracy and execution time. Figure 3-9 illustrates the mesh. To differentiate between the external and internal faces, two nodes at the same location have different properties. Coincident nodes belonging to different surfaces have been merged to prevent analysis errors.
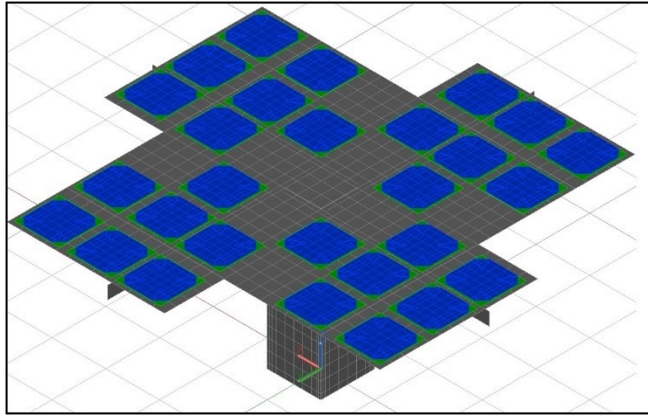
Figure 3-9 FD mesh visualization in Thermal Desktop.

For simplicity, the main structure of the satellite is entirely made of aluminum AL7075. The SolarCube, on the other hand, features a central hub made of aluminum AL7075, deployment system booms made of stainless steel, and the panel is composed of Nomex®, rigid PCB and solar cells.

The outer faces of the main body are alodine, while the outer surfaces of the rails are anodized, as prescribed by the CubeSat design specifications. Inside, the faces of the main body are painted completely black to maximize radiative heat exchange and temperature balancing within the satellite. As for the SolarCube itself, the central hub is also coated with black paint both internally and externally, and the booms are polished. The Nomex® material is also black, while the optical properties of the PCB and solar cells are unique to each of them and are described in the previous table. The information on orbital position and attitude is imported from STK and reflects the hypothetical mission described in the previous chapter. Currently, no internal heat loads have been considered since the payload(s) and on-board computer specifications will vary depending on the bus and mission in which the SolarCube will be employed. As a result, it is not possible to assume heat dissipation from these electronic components at this stage.

A transient analysis is performed starting on Jan 04 2023 at 00:01:00 and lasting about 3 orbital periods, until 4:31:00.

3.7.1.   Results

In Figure 3-10, the temporal behavior of the average temperature on the upper surface of Nomex® is depicted.
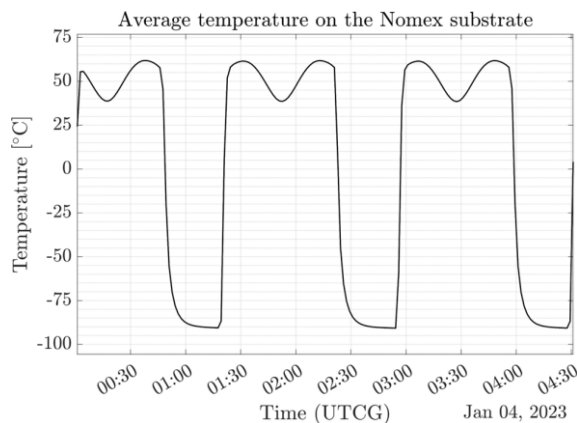
Figure 3-10 Temporal profile of the mean Nomex® surface temperature throughout tree orbit periods.

The trend aligns with power generation, exhibiting peaks when the panel is perpendicular to solar rays and dropping during eclipse periods. In shaded regions, heating comes from terrestrial albedo and planet IR emission. The highest average temperature is 61.87 °C, and the lowest is -90.76 °C.

40

3.7.2. Worst hot case

Figure 3-11 presents the spatial distribution at the time of maximum average temperature. Max temperatures are:
- Nomex®: 78.68 °C
- PCB: 66.65 °C
- Solar Cell: 67.85 °C

These temperatures remain within operational limits. A cooler area (5°C) at the center results from thermal contact with the satellite, modeled as Nomex®-aluminum interface.

Limited by Nomex®'s low conductivity, this causes a notable thermal gradient. Enhancing heat transfer via conductive traces or insulating material could resolve this.
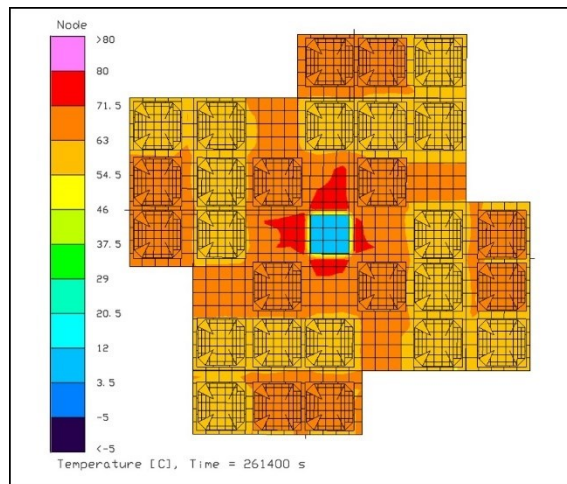
Figure 3-11 Worst Hot Case temperature spatial distribution, frontal view.

3.7.3. Worst cold case

Figure 3-12 displays spatial distribution at min average temperature.
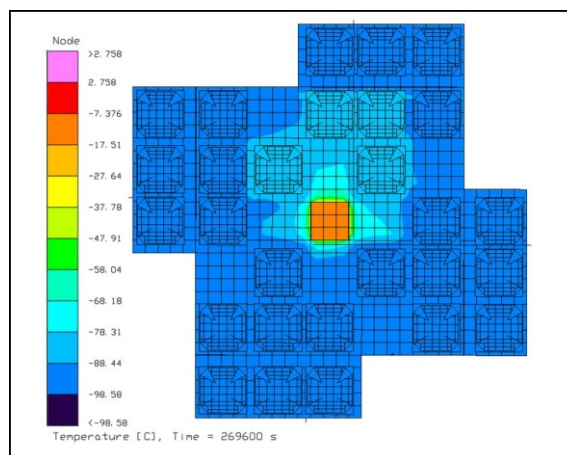
Figure 3-12 Worst Cold Case temperature spatial distribution, frontal view.

Minimum temperatures are:
- Nomex®: -98.87 °C
- PCB: -96.39 °C
- Solar Cell: -96.39 °C

Temperatures are generally within limits but near adhesive glass transition for PCBs and cells. The central hub contacts show higher temperatures. Nomex®'s low conductivity restricts radiative capacity,

limiting heat transfer from satellite to space via the panel area. Rest of the satellite maintains an average of -17°C.

3.7.4.   Internal hub considerations

Fig. 13 illustrates temperature trend inside the hub, relevant for battery control. The hub space will house the battery and Power Distribution Unit (PDU). Temperatures range from 11°C to 5°C, necessitating an active heating system to keep it within battery operational range. This system's impact on other satellite structures will be evaluated.
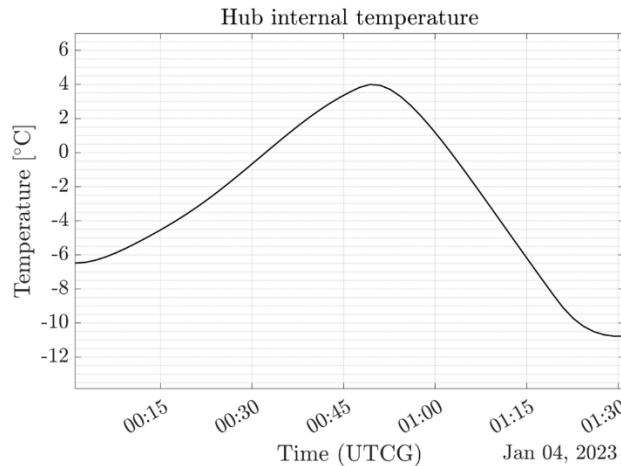
Figure 3-13 Temporal distribution of the hub's internal temperature throughout one orbit period.

3.8. Conlusions

In conclusion, the preliminary analyses presented in this paper underscore the technical efficacy and promising potential of SolarCube. Fueled by the innovative FRET technology, SolarCube opens up new avenues for the creation of deployable, origami-inspired lightweight solar panels tailored for nanosatellites.

To further solidify SolarCube's readiness for space deployment, future endeavors will focus on refining our models across structural, mission analysis, and thermal dimensions. These forthcoming models will encompass both static and dynamic analyses of the deployment system, seeking to bridge the gap between theory and practical application.

Our ultimate goal is to substantiate the theoretical findings with empirical evidence, advancing us closer to the in-orbit demonstration of SolarCube, slated for completion before 2025. Currently, a TRL 4 functional prototype is in active production, with plans for its completion by 2024.

The roadmap for the In-Orbit Demonstration (IOD) includes the finalization of the development system and an exhaustive analysis and testing phase for SolarCube. This comprehensive testing regimen encompasses vibrational and thermal vacuum tests. In parallel, we are actively collaborating with potential launch providers to identify the additional tests required for SolarCube and align them with platform requisites. These efforts are critical steps toward realizing the full potential of SolarCube in the near future.

3.9. References

[1]   A. Buscicchio, D. Vittori, V. Netti, A. Troise, N. Mangialardi, D. Guaragnella, and M. Cinefra, "Fret (flexible reinforced electronics with textile): A novel technology enabler for deployable origamiinspired lightweight aerospace structures," in AIAA SCITECH 2023 Forum, 2023, p. 2081.

[2]   J. T. Karras, C. L. Fuller, K. C. Carpenter, A. Buscicchio, D. McKeeby, C. J. Norman, C. E. Parcheta, I. Davydychev, and R. S. Fearing, "Popup mars rover with textile-enhanced rigid-flex pcb body," in 2017 IEEE International Conference on Robotics and Automation (ICRA). IEEE, 2017, pp. 5459–5466.

[3]   Endurosat. (2023) 3U Z Deployable Solar Array. [Online]. Available: https://www.endurosat.com/cubesat-store/cubesat-solar-panels/3uz-deployable-solar-array/buy-product

[4]   DCubeD. (2023) Origami solar array. [Online]. Available: https://dcubed.space/products/origami-solar-array/

[5]   AAC Clyde Space. (2023) Solar arrays. [Online]. Available: https://www.aac-clyde.space/what-we-do/space-productscomponents/photon-solar-arrays

[6]   MMA Design. (2023) High watts per kilogram "hawk" solar arrays. [Online]. Available: https://mmadesignllc.com/products/solar-arrays/

[7]   A. Troise, P. Celli, M. Cinefra, V. Netti, and B. Alessandro, "Reducedorder modelling of the deployment of a modified flasher origami for aerospace applications," in AIDAA XXVII International Congress. AIDAA, 2023.

[8]   Cosmogia. Dove-2 orbital debris assessment report (odar). [Online]. Available: https://apps.fcc.gov/els/GetAtt.html?id=123425x=

[9]   Y. Yao, Y. Zhou, C. Yuan, Y. Li, and H. Zhang, "On-board intelligent processing for remote sensing images based on 20kg micro-nano satellite," in 2021 IEEE International Geoscience and Remote Sensing Symposium IGARSS, 2021, pp. 8107–8110.

[10]   M. Ghiglione and V. Serra, "Opportunities and challenges of ai on satellite processing units," in Proceedings of the 19th ACM International Conference on Computing Frontiers, ser. CF '22. New York, NY, USA: Association for Computing Machinery, 2022, p. 221–224. [Online]. Available: https://doi.org/10.1145/3528416.3530985

[11]   S. Bandyopadhyay, G. P. Subramanian, R. Foust, D. Morgan, S.-J. Chung, and F. Hadaegh, A Review of Impending Small Satellite Formation Flying Missions. [Online]. Available: https://arc.aiaa.org/doi/abs/10.2514/6.2015-1623

[12]   J. Meseguer, I. Pe´rez-Grande, and A´. Sanz-Andre´s, "Spacecraft thermal control," 2012. [Online]. Available: https://api.semanticscholar.org/CorpusID:106639023

[13]   W. J. Larson and J. R. Wertz, "Space mission analysis and design," 1 1992. [Online]. Available: https://www.osti.gov/biblio/7369177

[14]   DuPont. Nomex®410 thecnical datasheet. [Online]. Available: https://www.dupont.com

[15]   M. M. Finckernor, "Comparison of high-performance fiber materials properties in simulated and actual space environments," 2017. [Online].

[16]   Available: https://api.semanticscholar.org/CorpusID:136512141

[17]   DuPont. Nomex® fiber, technical guide. [Online]. Available: https://www.dupont.com

[18]   J. H. Henninger, "Solar absorptance and thermal emittance of some common spacecraft thermal-control coatings," NASA Reference Publication 1121, 4 1984. [Online]. Available: https://ntrs.nasa.gov/citations/19840015630

[19]   C. R. F. Finckenor M. M, "Optical properties of nanosatellite hardware," NASA/TM—2014–218195, 6 2014. [Online]. Available: https://ntrs.nasa.gov/citations/20140010335

4. Paper #3. Finite element modeling on fret for origami-inspired cubesat applications

4.1. Abstract

Modelling of multi-layer rigid-flex printed circuit boards (PCB) for origami structures can be carried out with several different strategies, often resorting to models that either require a considerable amount of computational power, resulting excessively complex, or descending to oversimplifications that do not grasp the structural dynamics. Among these strategies, finite element modelling results the most convenient because it seizes the behavior of the system with an eye on computational efficiency. This study exploits a finite element approach to model the dynamics of a novel technology enabler for aerospace structures called FRET (Flexible Reinforced Electronics with Textile) applied in a CubeSat project (SolarCube). SolarCube is a deployable solar panel prototype system based on the flasher origami pattern, which possesses a large ratio of stowed-to-deployed diameter. Two finite element analyses were carried out, the first one with the prototype undeployed to analyze the dynamics in the launch phases, during which vibrations, impact shocks and thermal cycles become relevant. The second analysis was performed on the fully-deployed model to investigate the response of the solar panel substructure to the various solicitations relevant for the working phase. The results allow to evaluate the effectiveness of the finite element technique and also to explore the possibilities of the FRET technology, together with its efficiency in optimizing the available volume of the payload.

4.2. Introduction

Finite Element Method (FEM) is a numerical method for solving physics and engineering problems. It is particularly useful for elements possessing complicated geometry patterns and specific material properties or subject to loadings that make the problem difficult to solve with analytical methods. The body is modelled through a discretization of the geometry in many smaller units named finite elements, interconnected at common points called nodes. FEM has become a fundamental instrument in the analysis and optimization of engineering structures. An essential step in the design process for aerospace systems is represented by their modal analysis. In this study, the NASTRAN solver is used in PATRAN environment. The determination of the natural frequencies of the assembly is necessary to compare them with the operating frequencies of the working phase and is strictly correlated to the stiffness demand of the structure [1]. If natural and operating frequencies are too close, resonance and damaging events could come into play. The modal analysis also helps to determine the successive steps in a design layout, such as the most sensible locations, useful for a study on the position of sensors.

4.3. Project overview and technology enabler description

Origami-based applications require high flexibility of the components, which for deployable implementations are typically represented by cabling and flex-PCB. The assembly must also ensure the protection of the electronics from mechanical and thermal stresses. The traditional rigid-flex PCB lacks these properties due to its sensitivity to shear stress and tear propagation. FRET is the technology enabler exploited for manufacturing the CubeSat studied in the present dissertation. It decouples the stresses from the electronics through the integration of a textile layer, mastering the limitations of exclusively polyamide-based elements. Some preliminary studies investigated the effectiveness of FRET [2] or similar solutions [3] through four traction tests. The results of the tests represented the initial assessment for the performance of this innovative technology. This study mainly comprised two steps: in first phase the experimental results were compared to the ones obtained from the simulations in

PATRAN environment, this was done to validate the effective properties of the materials considered in the software, successively the analysis was scaled to the structure of the CubeSat in the open and closed configurations to obtain the first ten modal frequencies of the said layouts.

4.4. Experimental tests and modelling validation

Four different specimens of FRET were built to carry out the test. The specimens consisted of a three-layer structure, comprising textile, stiffener and electronics. The "Instron 8850" machine was used for the traction tests which imposed a constant displacement rate of $5\,mm/min$ to the blocked prototype and obtained the data with a sampling rate of $100\,Hz$. The assembly of the specimen is visible in Figure 4-1 The textile has a width of $0.55\,mm$, and a tensile strength of $374\,N/cm$.

An equivalent model of the specimens, visible in Figure 4-2 was designed in SolidWorks and exported as a STEP file inside the Patran environment. The traction test was simulated by imposing a full translational and rotational constraint on one side together with an imposed displacement on the second side. The imposed displacements span in the range from zero to ten millimeters, which was chosen following an analysis of the experimental results. In the Patran environment, it was chosen to use an ideal connection between the PCB and the textile by meshing the two solids individually and successively equivalencing the common nodes. This approximation was chosen since the analyses were performed below the ultimate adhesive strength of the glue. Some previous studies [4] [5] analyzed a similar assembly of textile and rigid-flex PCBs, and resulted very important as a reference value for the correct implementation of Young's modulus, density and Poisson ratio values in the simulation environment.
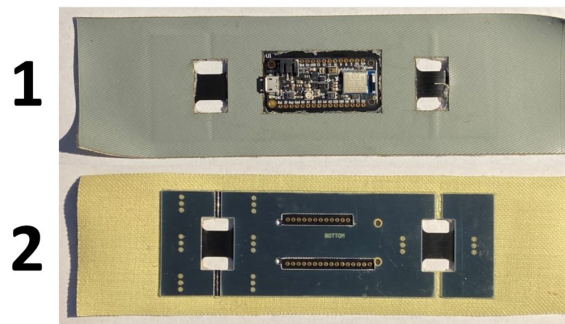
Figure 4-1 - ONE OF THE SPECIMENS USED IN THE TRACTION TEST 1)TOP LAYER 2)BOTTOM LAYER
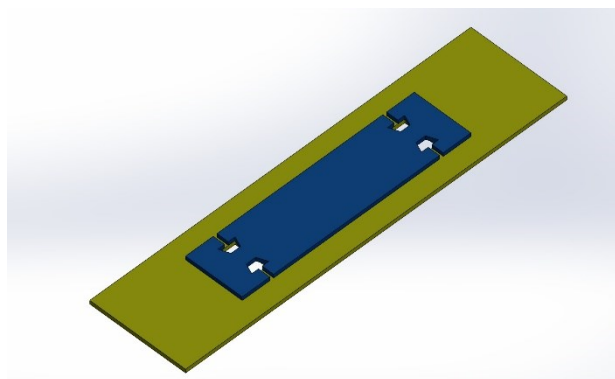
Figure 4-2 - 3d model of the specimen recreated in solid- works environment, textile in yellow and rigid-flex pcb in blue

4.4.1. Results of the validation procedure

The traction test shown in Figure 4-3 comprised six prototypes, the first four (P0,P1,P2,P3) are FRET specimens, while the last two (P4,P5) are Nomex-only specimens used as reference. The values of stress

obtained from the simulation of FRET in PATRAN are also visible in the plot. Out of the four FRET specimens, P2 showed an issue in the bonding substrate, while the specimen considered the closest representation of the final assembly is P0, even though it can be noticed that some delamination phenomena showed up at around $8mm$ of displacement.

The computations for the validation procedure were therefore carried out using as a reference the curves P4 (Nomex-only), P0 (FRET) and the values obtained from the simulations in PATRAN environment. To define the error between the experimental values and the simulation values two root mean square error indexes were used, one between the simulation values and the P4 values, called ($RMSEf\ ret$) and the other between the P4 trend and the experimental values of P0, called ($RMSEmeas$).

A key performance indicator (KPI) was defined in order to numerically estimate the quality of the simulation compared to the experimental data. It was defined as:

$$KPI = \frac{RMSE_{fret} - RMSE_{meas}}{RMSE_{meas}}$$

This KPI can be described through the three extreme possible condition:
1. $KPI = -1$ - Is the best case and implies that $RMSEf\ ret$ is zero and the simulation of FRET is perfectly identical to its experimental values (the ideal case)
2. $KPI = 0$ - Is the worst case and implies that $RMSEf\ ret$ is identical to $RMSEmeas$, therefore the simulation of FRET does not capture any difference between itself and Nomex textile.
3. $KPI = \infty$ - Is the case in which the simulation moves away from both the experimental values of FRET and Nomex,

and is the less interesting condition from a practical point of view.

Through the use of the aforementioned KPI, the results high- lighted a value of:

$$KPI = -0.6271$$

Which guarantees that the simulation values are sufficiently closer to the FRET case than the Nomex one. This is because the KPI implies that acceptable values are represented by any negative number. More specifically good values lie in the range from -0.5 to -1. This results allowed to consider the simulation an acceptable representation of the assembly, therefore bringing the study in its second phase.
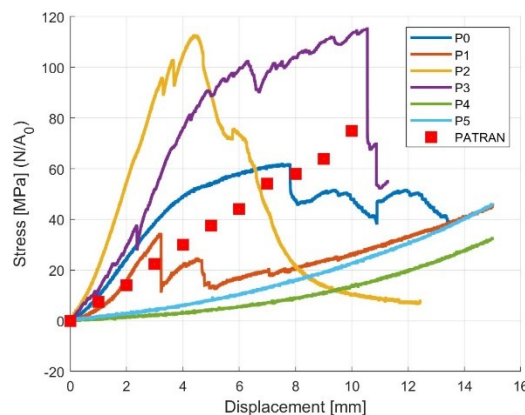
Figure 4-3 - Displacement vs stress plot of the traction test
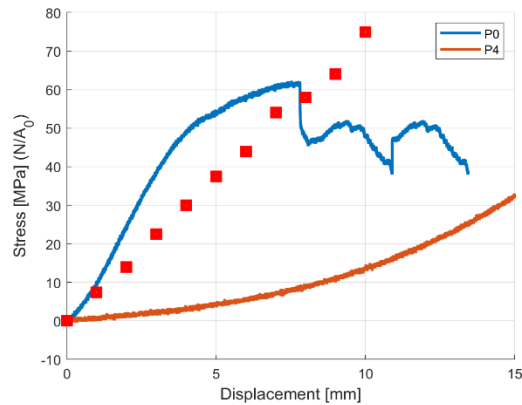
Figure 4-4 - most representative experimental plots of fret and nomex, together with patran results

4.5. Finite element model of the cubesat

The model of the CubeSat in open and closed configuration was built once again in the SolidWorks environment and successively exported as a STEP file in the Patran software. Its dimensions correspond to a 1U volume, therefore it is compatible to a $100x100x100mm$ launcher, and its respective scaled-up versions.

The meshing of the components was developed using tetrahedral elements with 10 nodes (Tet10). The characteristic dimension of the element was chosen to guarantee an acceptable aspect ratio for the solver together with good accuracy of the analysis. The number of elements in the open model was 751241, with 1244390 nodes. In the closed case, on the other hand, the number of elements resulted equal to 23495 with 46206 nodes. The smaller number of elements in the closed model case is explained by the inherent reduced complexity in the analysis.
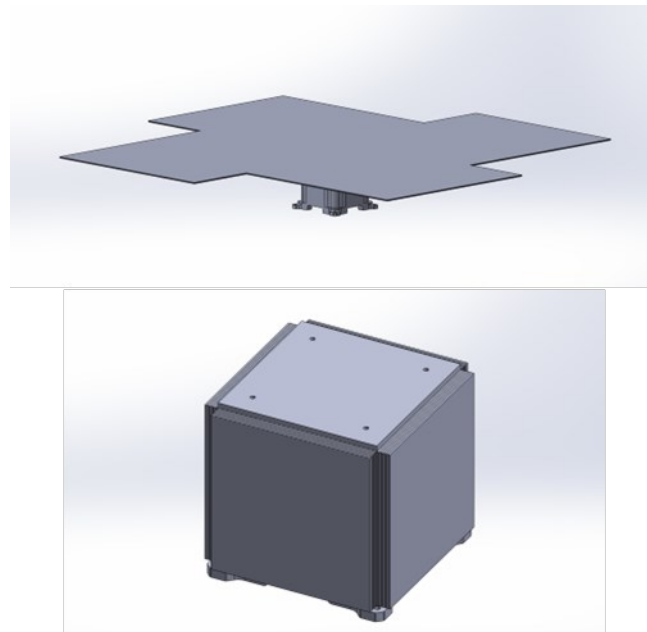
Figure 4-5 - SOLIDWORKS MODEL OF THE CUBESAT UNIT IN OPEN AND CLOSED CONFIGURATION

In Figure 4-5 the two models ready for import are visible. The "sail" of the CubeSat is made of a FRET stack up, therefore the first layer of the textile is bonded to the PCB, and this was modelled through separated solids joined together with an ideal glue, once again thru the nodes equivalencing procedure. In Patran environment the properties and thickness of the Nomex and the PCB were chosen to be the

same as the FRET prototype, with the addition of the central hub to which the "sail" is bounded, which was considered as aluminum alloy 6061-T6, commonly used for CubeSats. The analyses, both in the open case and in the closed one, were carried out by imposing as boundary conditions complete rotational and translational constraints on the lower surface of the central hub, to which the sail is joined. The modal analysis has the objective of determining the natural frequencies of the device, it is an analysis of primary importance and it is necessary for the definition of the modes having the most relevant contribution in a forced vibration response.

4.5.1. Results of the modal analysis

The modal analysis of the open configuration yielded the frequencies present in Table 4-1 while The frequencies for the closed case are present in Table 4-2.

Modal steps	Normal frequency [Hz]	Modal shape
1	0.21826	Bend along x axis
2	0.23705	Bend along z axis
3	0.273034	Bend along y axis
4	0.300871	Twisting
5	0.493482	Partial mode
6	0.816179	Partial mode
7	0.820591	Partial mode
8	1.13176	Partial mode
9	1.33542	Partial mode
10	1.53667	Partial mode

Table 4-1 - First ten modes of the open configuration of SolarCube

Modal steps	Normal frequency [Hz]	Modal shape
1	19.0177	Twist around y axis
2	25.2452	Bend along y axis
3	27.9539	Bend along y axis
4	40.2545	Twisting
5	51.5869	Partial mode
6	54.9474	Partial mode
7	59.9706	Partial mode
8	61.3172	Partial mode
9	66.4077	Partial mode
10	71.1021	Partial mode

Table 4-2 - First ten modes of the closed configuration of SolarCube

The open case presents, as expected, much lower frequencies lying in the range 0.21826 ÷ 1.53667.

The closed case, instead, highlighted natural frequencies in the range 19.0177 ÷ 71.1021.

It can happen that experimental tests do not match the modal frequencies obtained from the simulations, in that case, the typical procedure consists in modifying the characteristic parameters of the materials until convergence, therefore avoiding to jeopardize the analysis carried out before the experimental results. A common reason for this phenomenon is the presence of residual stresses at the microscopic level in the structure.

Vibration tests in satellite components are of paramount importance for determining much information about the assembly, they are carried out both on the individual components and on the whole structure depending on the specific case. Some of the most important considerations about vibration tests are enumerated below:

1. They help to determine the frequency response of the structure for the attachment of electrical components

2. Allow to verify the structural reliability and assembly precision of bracing elements

3. Help check the functionality of release and deployment devices under dynamical loading

4. Permit the verification of the transfer coefficient not only under launch conditions but also for air or land transportation

The satellite structure can be divided into primary, secondary and tertiary components. The primary components comprise the "backbone" of the structure, supporting major loads and the launch vehicle (LV) adapter. The secondary components include the main sub-structures together with solar arrays and panels. Tertiary components assort all the connecting elements such as brackets and screws or rivets. The analysis has been carried out only comprising elements of the primary and secondary level and without the inclusion of the deployment system. A benchmark

value for the lowest modal frequency of the closed configuration is around $20 \div 40 Hz$, the necessary value is a function of the typical frequencies of the launch vehicle. Considering the user manual of the Ariane 5 spacecraft [6], the closed CubeSat structure needs to have a fundamental lateral frequency of at least $10 Hz$ and a fundamental longitudinal frequency of at least $31 Hz$. The aforementioned values comprise also the presence of the outer shell, an element that typically increases the natural frequencies of the structure. For the study case in this dissertation, it has not yet been designed since once again it depends on the specifics of the LV. Overall, the values fall in a reasonable order of magnitude.

4.6. Conclusions and future developments

Modal analysis represents a fundamental tool in the design procedure of mechanical components. In this study, an innovative way of implementing the electronics exploiting textile combined with rigid-flex PCB (FRET) was presented as a possible technology enabler for deployable origami structures.

The key parameters used in the PATRAN simulation environment were validated through the comparison between benchmark values obtained from experimental traction tests, which have been analyzed introducing also a key performance index (KPI). Then, the dynamic performances of a CubeSat volume were investigated by obtaining the first ten natural frequencies of a hypothetical assembly of the solar array, both in its closed and open configuration. The results highlighted values inside the expected range and also in line with the requirements obtained by the user manual of Ariane 5 spacecraft, used as a reference. These analyses resulted in one of the first approaches to the modelling phase the FRET, which represents a difficult task having very little previous studies on said technology. FRET could represent an efficient method to increase energy harvesting properties without breaking the volume constraints typical of CubeSats. The modal analysis results are a key step to performing harmonic response analysis and dynamical stress (fatigue) analysis for the assembly. Future developments could be represented by an implementation of the deployment system in the assembly, together with other analyses useful for the inspection, qualification and testing procedures of spacecraft assembly.
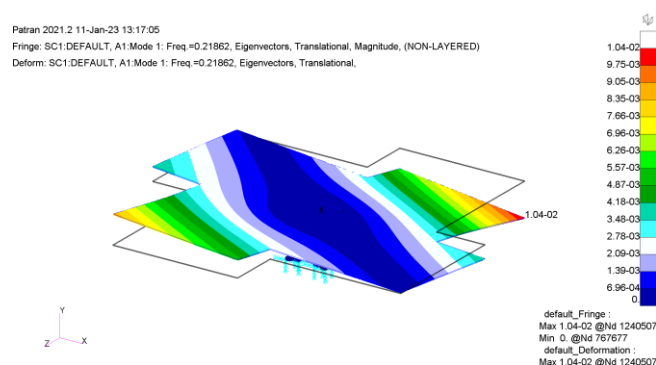
Figure 4-6 - first mode of the open configuration
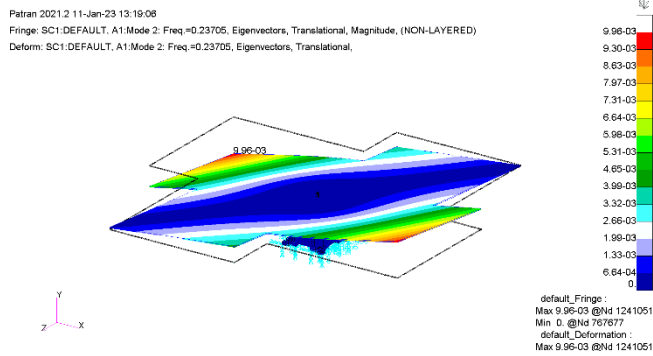
Figure 4-7 - second mode of the open configuration
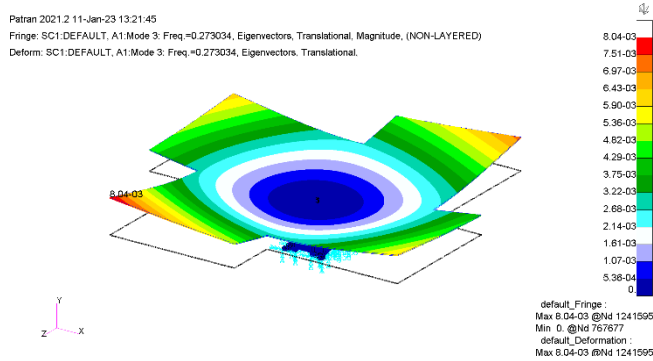
Figure 4-8 - third mode of the open configuration
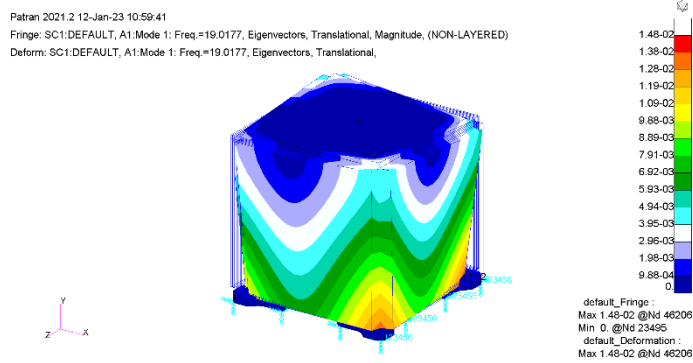
Figure 4-9 - : first mode of the closed configuration
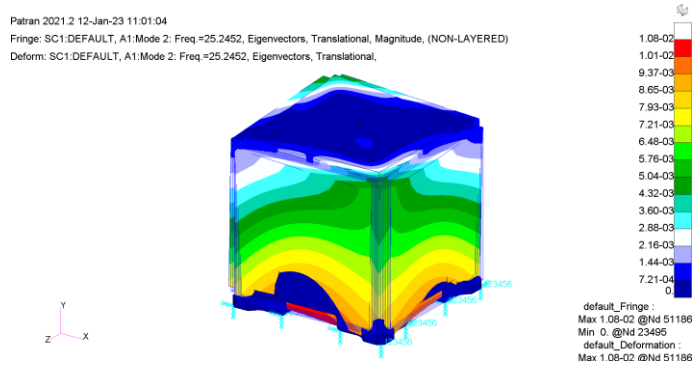
Figure 4-10 - second mode of the closed configuration
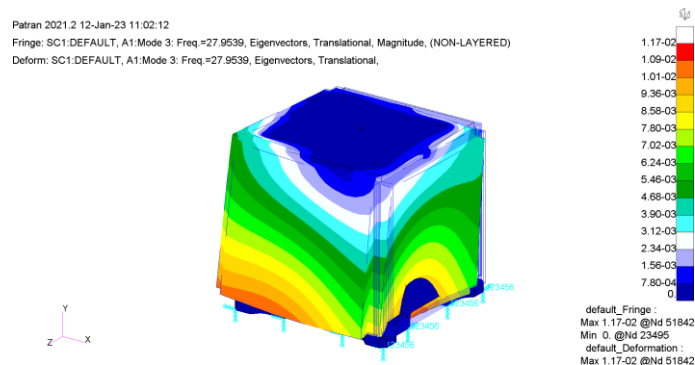
Figure 4-11 - third mode of the closed configuration

4.7. References

[1] Bai, Zhengfeng, Zhao, Yang, Ma, Wenlai and Tian, Hao. "Modal analysis for small satellite system with finite element method." *2008 2nd International Symposium on Systems and Control in Aerospace and Astronautics*: pp. 1–5. 2008. DOI 10.1109/ISSCAA.2008.4776403.

[2] A., Buscicchio, D., Vittori, V., Netti, A., Troise, N.A., Mangialardi, C., Guaragnella and M., Cinefra. "FRET (Flexible Reinforced Electronics with Textile): A novel technology enabler for origami-inspired lightweight aerospace structures." (2022). Under review.

[3] Karras, Jaakko T., Fuller, Christine L., Carpenter, Kalind C., Buscicchio, Alessandro, McKeeby, Dale, Norman, Christopher J., Parcheta, Carolyn E., Davydychev, Ivan and Fearing, Ronald S. "Pop-up mars rover with textile-enhanced rigid-flex PCB body." *2017 IEEE International Conference on Robotics and Automation (ICRA)*: pp. 5459–5466. 2017. DOI 10.1109/ICRA.2017.7989642.

[4] Bell, John, Redmond, Laura, Carpenter, Kalind and de la Croix, Jean-Pierre. "Finite Element Modeling of Rigid-Flex PCBs for Dynamic Environments." *Journal of Microelectronics and Electronic Packaging* Vol. 19 No. 1 (2022): pp. 25–38. DOI 10.4071/imaps.1655356.

[5] Bell, J., Redmond, Laura, Carpenter, K. and Croix, J. "Experimental Dynamic Characterization of Rigid-Flex PCB Systems." *Experimental Techniques* (2022): pp. 1–15DOI 10.1007/s40799-022-00559-4.

[6] Arianespace. "Ariane 5-User's Manual Issue 5 Revision 2." (2016). URL https://www.arianespace.com/wp-content/ uploads/2011/07/Ariane5_Users-Manual_October2016.pdf.

[7] Abdelal, Gasser, Abuelfoutouh, Nader and Gad, Ahmed. *Finite Element Analysis for Satellite Structures*. Springer London (2013): pp. 251–270. DOI 10.1007/978-1-4471-4637- 7_6.

[8] Bathe, Klaus-Jürgen. *Finite Element Method*. John Wiley & Sons, Ltd (2008): pp. 1–12. DOI https://doi.org/10.1002/9780470050118.ecse159.

5. Paper #4. Electrical ground support equipment for the sampling caching system of the mars 2020 rover

5.1. Abstract

In this work we describe in detail the architecture, design, testing and operation of the Electrical Ground Support Equipment (EGSE) "Blue Box" used to test and validate the Sampling Caching System (SCS) of the Mars 2020 Perseverance rover. The Blue Box architecture is centered around COTS motor controllers and COTS input-output modules communicating over an EtherCAT bus. A custom, low-level safety subsystem ensures no harm can be done to the flight articles. The modular architecture of the EGSE reduces cost and complexity while expediting assembly time. The Blue Box drives the 19 actuators of the SCS which span the main robotic arm, the corer system, the internal sample handling arm, the sample tube sealing system and the gas dust removal tool; mimicking the Rover Motor Control Assembly (RMCA). Due to the limited availability of RMCA's, the EGSE enabled and performed the bulk of testing activities for SCS. The majority of the SCS actuators are composed of a 3-phase DC brushless motors, hall sensors for commutation, dual resolvers for output angular measurement, brakes, heaters and platinum thermistors. Additionally, the EGSE read 12 strain gauges forming part of a force torque sensor, and switches used for external positioning references. Over the 3-year span of the V&V campaign for the SCS, over 32 EGSE systems were built, tested and deployed to test venues at JPL and externally. The EGSE tested several families of the SCS subsystem, ranging from engineering units, life test units and two flight units. Test venues that this EGSE supported included lab benches, ultra-clean cleanrooms, ATLO facilities, and thermal vacuum chambers. Together with the test software systems, SSDEV and SSDEV-ECAT, the Blue Box EGSE enabled the team to efficiently test flight hardware and flight software together. We go over the safety features and fault management techniques employed to protect flight hardware. The effects of the long, 50-feet, EGSE harnesses on motor performance, EMI, electrical noise, and motor control performance are explained. Mitigations to these unwanted effects, including shielding strategy and inductance compensation, are summarized. We go over an excerpt of notable anomalies that this EGSE suffered through its operation, along with investigations and resolutions. Lessons learned, areas of improvement as part of future work, and recommendations for future implementations for similar EGSE's, are shared.

5.2. Introduction
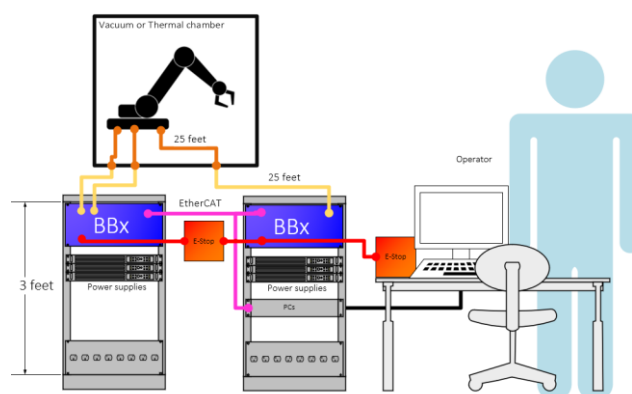
Figure 5-1 High level diagram of the Blue Box EGSE

The extensive verification and validation (V&V) campaign that space missions require necessitate the need for concurrent testing of multiple subsystems at different levels of maturity. Since flight electronics are usually in short supply, Electrical Ground Support Equipment (EGSE) is utilized in-place of the spacecraft flight electronics to control and characterize multiple electrical and mechatronic

subsystems prior to final integration onto the spacecraft. The JPL-NASA Mars 2020 (M2020) rover mission "Perseverance" was no exception to this approach. M2020's primary mission is to core and seal samples of Martian rock as the first step of a planned sample-return campaign. Perseverance is the first leg of several spacecraft that would need to fly to Mars in order to bring these samples back to Earth for extensive analysis. The Sampling and Caching Subsystem (SCS) in M2020 is responsible for all sampling operations including coring, sample transferring, sample inspection, sample tube sealing and storage. The SCS is composed of 17 actuators that span two robotic arms, a drill, a bit carousel and a tube sealer. Over the 3-year span of the V&V campaign for the SCS, over 32 EGSE systems were built, tested and deployed to test venues at JPL and externally.

5.2.1. Heritage

The large number of robotic research projects at JPL have continuously pushed the requirements for the EGSE driving mechatronic systems. Since early 2000's, several generations of EGSE have been designed and implemented, each better than the previous one. In early 2017, when the V&V of SCS commenced, the EGSE used by research robotic projects at JPL was the Research Blue Box (RBx) [1]. RBx was based on the high bandwidth communication protocol EtherCAT, developed by Beckhoff. This communication bus allowed to daisy chain multiple COTS modules, each with a specific function, to achieve high frequency control and telemetry with a single RJ45 cable.

In RBx, the ELMO Gold Solo Whistle motor controller, EtherCAT compatible, was utilized to actuate 3-phase brushless motors via hall and optical encoders. A wide range and number of Beckhoff EtherCAT I/O terminals were used to acquire and drive different types of analog and digital signals. The flexibility allowed by the endless combination of several different types of compact Beckhoff terminals made RBx an easy-to-reconfigure EGSE. Since the bulk of the electronics in RBx are Commercial Off the Shelf (COTS), it reflected in low cost and rapid implementation cycles. RBx was not designed with a flight mission V&V campaign in mind, therefore it did not include an extensive set of safety and protection circuitry.

The EGSE for SCS, a flagship flight mission, required robust circuity with multiple layers of safety and protection, as stated by JPL principles. Testing procedures and formalized documentation of each EGSE system were also necessary to ensure proper traceability during V&V. These requirements triggered the development of the SCS EGSE which inherited several aspects from RBx, mainly the EtherCAT bus, ELMO motor controllers and Beckhoff I/O terminals. The chassis housing the electronics for the SCS EGSE also shared the royal blue hue of its predecessor and eventually became known as simply "Blue Box" (BBx) by its more than 40 operators. A flight-like software version interfacing onto the Blue Box EtherCAT bus was developed [2].

5.3. Blue Box EGSE

5.3.1. Requirements

The Blue Box EGSE high level requirements stated:

Do no harmSingle point failures on the Blue Box electronics shall not cause damage to the flight article under test. This safety philosophy lead to several layers of protection culminating on a Failure Mode Effects and Criticality Analysis (FMECA).

Actuator: Although there were different designs and configurations for the 17 actuators in SCS, a global, representative set of sensors and driving requirements were used to architect the Blue Box and ensure compatibility with all actuators. For each actuator the EGSE interfaced with:

Auxiliary devices: SCS housed several sensors and devices not specifically tied to a single actuator. A global, representative list of sensors was composed in order to ensure Blue Box could interface with these auxiliary devices. Each Blue Box EGSE could interface to:

Communication: The EGSE shall communicate with the high-level software using the EtherCAT bus. Since EtherCAT is a daisy chain communication bus, multiple EGSE racks could be connected together to form a cohesive system. EtherCAT allowed modularity at the rack level.

Emergency Stop: The EGSE shall interface with an Emergency Stop Button (ESTOP) allowing the daisy chain of multiple such ESTOPs as required. This allowed the testbed operator and the "test buddy" to each have an ESTOP placed at different locations.

Harnessing: The EGSE shall interface to the flight article via numerous sets of two, 25-feet long, harnesses. The two harnesses provided the capability to drive test articles inside a vacuum or thermal chamber by breaking the connection at the chamber bulkhead. The 25-foot length ensured ample room to physically locate the EGSE on the test venue and the flight article inside a chamber. The ease of placement allowed by the long harnesses came at a cost of increased EMI/EMC.
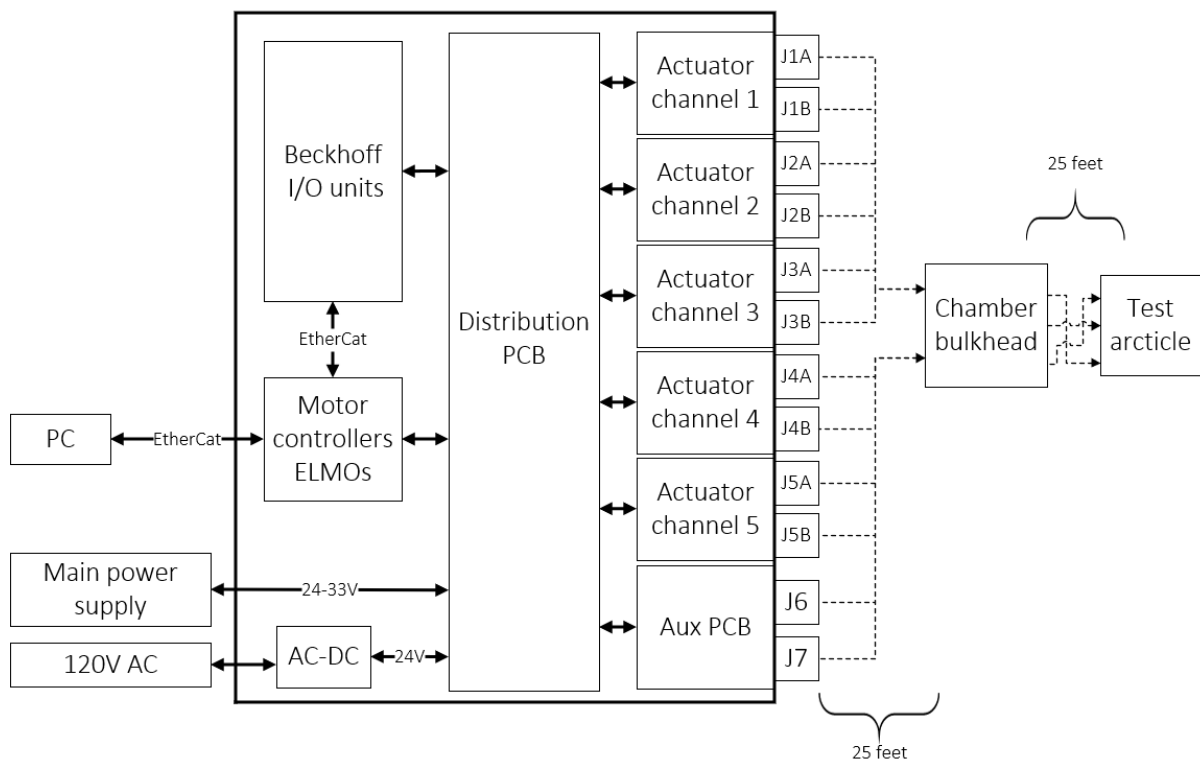
Figure 5-2 Architecture of Blue Box EGSE. Dashed lines represent long harnesses. Solid black periphery is the Blue Box chassis. J# are circular connectors.

5.3.2. Architecture

With knowledge that the EGSE would deploy to 30-plus testbeds, each with different testing goals and a particular subset of SCS actuators, forced the team to produce a highly configurable architecture based on different levels of modularity. For the lowest level of modularity, the design employed a group of Printed Circuit Boards (PCBs) that provided full functionality for either an "actuator channel" as described in Figure 5-2, or an "auxiliary channel", Table 5-2.

Qty.	Device	Notes
1	3-phase	

Qty.	Device	Notes
	brushless motor	
1	Hall encoder	Composed of 3 hall sensors producing 6 different states of commutation.
1	Dual resolver	A single excitation coil with one 1/16 revolution feedback coil and
2	Resistive heaters	Quantity two used for redundancy. Only one heater active at a time.
2	Motor-Brake coils	Solenoid based brakes for motors. Quantity two used for redundancy. Only one brake active at a time.
4	Platinum Resistance Thermometer (PRT)	Distributed temperature sensing in different locations of the mechanism.

Table 5-1 Blue Box capabilities for each actuator channel

Qty.	Device	Notes
12	Strain gauges	Full bridge strain gauges usually arranged as a force torque sensor.
4	Platinum Resistance Thermometer (PRT)	Distributed temperature sensing in different locations of the SCS.
2	Resistive heaters	Quantity two used for redundancy. Only one heater active at a time.
1	Dual resolver	A single excitation coil with one 1/16 revolution feedback coil and one full revolution feedback coil.
8	Switches	Used for binary detection of mechanism positioning or interactions with the environment.

Table 5-2 Blue Box capabilities for its auxiliary channel

A single, large PCB, the "Distribution PCB", was then used to merge and route all signals interfacing to the actuator channel stacks, the auxiliary channel, motor controllers, I/O acquisition units, power rails and emergency stop signals.

The actuator channel PCB stack was composed of three separate PCBs:

1. The "Adapter PCB" was used to house two, board mounted, circular connectors that attached to the Blue Box front panel and provided the main interface to the harness leading to the test article. Directly mounting the connectors onto a PCB eliminated workmanship errors. The circular connectors are of the MIL-C-26482 specification, shell size of 24, 61 contacts (BRANDEX 74L24-61). The external interface of these connectors employed bayonet fastening with normal clocking. The connector attached to the Blue Box front panel via a lug nut. The two connectors used opposite genders to avoid damage to the test article on user misconnection. Female sockets were used for the "power outputs" (motor phases, heaters and brakes), and male pins for the inputs to the Blue Box (Halls, PRT's and resolvers). The pinout in these connectors grouped common signals together and left spare pins around them to separate different groups. This spacing was introduced to avoid shorts in case of workmanship issues. The Adapter PCB also housed the circuitry to excite and read the dual-resolver.
2. The "motor PCB" stacked onto the adapter PCB via board to board connectors (SAMTEC PowerStrip), which allowed flexibility on connecting power and low voltage signals. The motor PCB housed the electronics interfacing to the dual-brakes, dual-heaters, halls and PRT's. The

motor PCB interfaced with the rest of the Blue Box electronics (Distribution PCB) via a 40-pin ribbon connector and a power connector (MOLEX ULTRAFIT).

3. The "inductor PCB" is the third and final PCB on the actuator channel stack. It houses the relatively bulky surface mount inductors used to optimize driving the brushless motors over the long harnesses. The inductor PCB interfaced directly to the motor controller output (ELMO's) via a custom harness employing pluggable screw terminals (Phoenix COMBICON). This ensured minimum crosstalk between noisy motor phases and the rest of the Blue Box circuitry. The inductor PCB then fed the compensated motor phase signals to the Motor PCB which then routed them to the Adapter PCB finally making their way to the front panel connector.
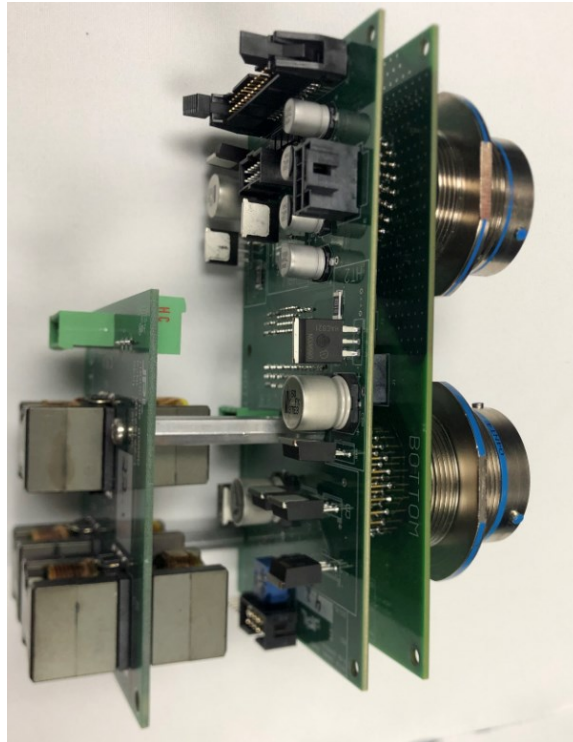
Figure 5-3 -Actuator channel PCB stack. From right to left, Adapter PCB, Motor PCB, Inductor PCB.

For the auxiliary channel, a single PCB, the "Aux PCB", housed the two circular connectors (identical to the circular connectors on the actuator channel PCB stack but with W clocking) that interfaced to the test article. The Strain gauge excitation circuitry was housed on this PCB. To reduce EMI/EMC on the unamplified strain gauge signals, the number of active components on this PCB was minimized. For this reason, the heater, resolver, PRT and switch electronics were housed on the Distribution PCB. The strain gauges connected directly to an EL3602 Beckhoff I/O unit via a six-inch run of double-shielded, twisted pairs on a RJ45 cable.

The distribution PCB functioned as the main routing board and housed all box-level electronics. All actuator channels interfaced onto the distribution PCB which then routed the relevant signals to the motor controllers and Beckhoff I/O units. A peripheral PCB, "ESTOP PCB" used to interface and condition the Emergency Stop button and power supply control signals also interfaced to the distribution PCB.

5.3.3. Electrical design

Figure 5-4 Front interface of Blue Box EGSE. Actuator channels are labeled M1 through M5. Top cover removed.
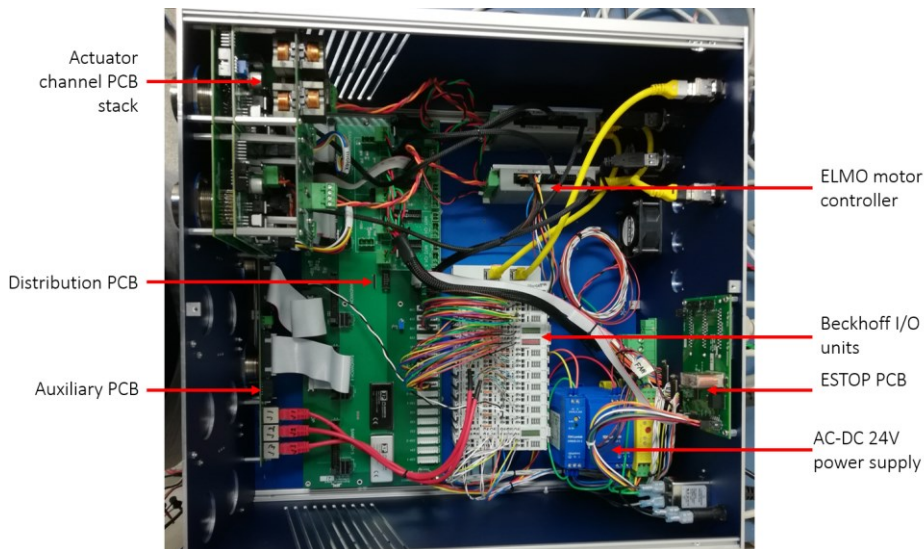
Figure 5-5 Main components of Blue Box EGSE. Yellow cable, EtherCAT. Red Cables, RJ45 with strain gauge signals.

Blue Box employed a combination of COTS and custom elements to interface with the actuators and sensors present on the test articles. An external power supply, Keysight N5746A, provided the power for motors, heaters and brakes. An internal 24V power supply powered the Beckhoff stack, logic power for the motor controllers, and the DC/DC converters on the Blue Box PCBs, see Figure 5-2 & 5-5. The majority of the circuitry was protected by means of electronic fuses (eFuse). A summary on the design for each driven element follows:

Motor controller: An ELMO GOLD DC WHISTLE was used to interface to the 3-phase brushless motors. Motor currents ranged from 1 to 20A. For each actuator channel, an ELMO with suitable

current rating was chosen. The motor controller output had to be compensated to account for harness-added resistance. The power fed to the motor controller was protected by an eFuse.

Heater-Resistive heaters with up to 4A of current were driven by a high-side FET based switch. Heater current telemetry was produced by a low-side shunt resistor followed by an AD8429 instrumentation amplifier which was then read by an EL3608 Beckhoff module. The heaters were operated in a bang-bang mode only, high frequency PWM was not employed. The power fed to the heater circuitry was protected by an eFuse. The heater circuitry was housed on the Motor PCB.

Brake driver: The brake engaged the motor shaft, not allowing rotation, when there was no current flowing. When the brake coil was energized it allowed the motor shaft to spin freely. To ensure proper release of the brake, and to reduce the chance of overheating, a two-step-like current waveform was required. Nominally, the brake was operated by flowing a "peak current" of 1.75A for 200 milliseconds followed by a continuous 0.75A "hold current" which persisted as long as the brake was commanded to open. The "peak current" ensured the brake mechanism released the shaft. Once the shaft was released a lower current is needed to maintain the brake open, "hold current".

The current waveform required by the brake necessitated a current controller, implemented on an ATMEGA328P. A simple PID-like controller ran in the microcontroller to ensure the proper current setpoint. Brake current was monitored by a high-side shunt resistor followed by an INA169 current monitor. This allowed the measurement of the current inside the coil-and-kickback-diode loop. Low side FETs driven by a PWM signal allowed for current control. The microcontroller was triggered to energize a brake by a TTL-level brake signal coming from the ELMO motor controller. The microcontroller then produced the desired current waveform as dictated by hardcoded parameters in the firmware. The power fed to the brake circuitry was protected by an eFuse. The brake circuitry was housed on the Motor PCB.

Dual resolver: Resolvers in M2020-SCS had the peculiarity of having a single excitation coil and two feedback coils. This allowed for a 0-360° absolute readout and a 16x, 0-22.5°, incremental-like signal with higher resolution. The Blue Box employed an AD2S99 programmable oscillator followed by a TCA0372 dual power amplifier to generate the excitation coil sine waveform. Two, AD2S90 Resolver-to-digital (RD) converters, interfaced with the feedback coils via a 2nd order active filter to produce the angular telemetry. A single ATMEGA328P microcontroller, housed in the distribution PCB, interfaced with the up to 12x AD2S90's (2 for each of the 5 motor channels and 2 for the single auxiliary channel). The microcontroller continuously polled all RD converters and sent the telemetry upstream to the higher-level software via RS232 onto an EL6001 Bekchoff module. The resolver circuitry was housed in the Adapter PCB minimizing trace lengths on these sensitive signals.
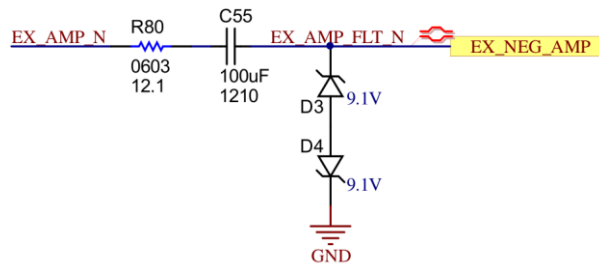
Figure 5-6 Dual resolver protection.

In case of a failure on the excitation coil circuitry, the resolver excitation coil signals were protected by an inline capacitor, and back to back Zener diodes. The capacitor blocked DC current and the Zener's limited the amplitude on the AC sine signal.

PRTThe PRTs were read by a set of EL3208's Beckhoff modules. In case of an anomaly on the EL3208, an inline resistor and Zener diode were employed to shunt any overvoltage events that could cause large

current on the flight article PRTs. The EL3208 accounted fort his added resistance via a software parameter.
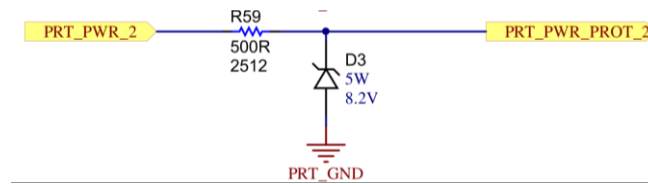
Figure 5-7 PRT protection.

Halls: The Hall sensors, used to commutate the motor, were read and processed by the ELMO motor controller. An ADUM1400 digital isolator was used to ensure failure in the ELMO Hall input circuitry did not propagate onto the flight article. The 5V rail powering the hall sensors was protected by an eFuse.

Strain gauges: The strain gauges signals were read by a set of EL3602 Beckhoff modules. The 24-bit resolution and high precision on the EL3602's allowed to read the strain gauges directly, without amplification. The tunable input range on the EL3602 was set via higher level software to match the expected range of each strain gauge. The 10V excitation signal, common to all strain gauges, was produced by a low noise LDO, TPS7A4700, and protected by an eFuse. The 10V excitation was also read by a EL3602 to account for any offset on this signal.

Switches: The switch signals were read by an EL1008 digital input Beckhoff module. The switch "excitation" was protected by a 1kΩ inline resistor in case the excitation voltage rail suffered an anomaly or there was a short circuit to ground downstream.

5.3.4.   Configuration management

Due to the large number of EGSE systems deployed, and significant customization for each delivery, a robust configuration management scheme was envisioned. The customization included different protection parameters for current or voltage, resolver impedances, harness-compensating inductors and firmware parameters. Each PCB had a revision-controlled drawing that called for particular passive components to not be installed by the manufacturer. At the box level, a top assembly drawing was then generated for each delivery that included a specific value for the non-installed passives on all the PCBs, the number of actuator channels present and firmware parameters. This scheme effectively stored all the configurations on individual top assembly drawings rather than at the PCB or mechanical chassis level.

5.3.5.   Harness design and grounding

The long span of the harness connecting the Blue Box EGSE to the article under test, two segments 25-feet each, facilitated physical placement of the Blue Box on the test venue, and allowed seamless connections through any chamber bulkheads. The length of the cable introduced electrical parasitic in the form of resistance, inductance and capacitance that caused several anomalies.

The overall harness employed multiple, shielded, twisted pairs carrying a main signal and its corresponding return. The bundles carrying motor phases were composed of twisted triplets. Low voltage signals employed 22 AWG while high power signals employed several sets of 20 AWG wire shared across multiple pins on the circular connectors. The harness did not directly propagate the shield connection onto the connector backshell, but instead terminated the shield with an eyelet that could be connected or disconnected to the circular connector body at will. This provided useful flexibility on choosing the shielding strategy, i.e. shield connected at both ends or just one end. This proved useful

while troubleshooting EMI/EMC anomalies. The shield was also spliced onto a pin of the connector to allow interfacing it to the inside of the Blue Box.

During the design phase, the team only considered the added resistance of the harnessing and compensated several driving circuitries including the ones interfacing to the motor phases, the resolver excitation coil and PRTs. Compensating the effects of the added resistance by the long harness on the motor phases proved to be a non-trivial task.
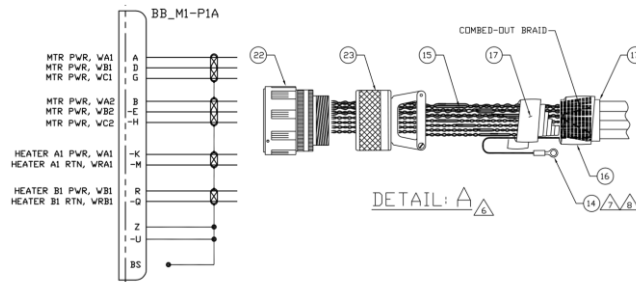
Figure 5-8 Blue Box EGSE harness drawing. "Note 14" points to the eyelet carrying the shield signal. Pins Z and -U also carry the shield signal. Note how the backshell "BS" is not connected to the shield signal.
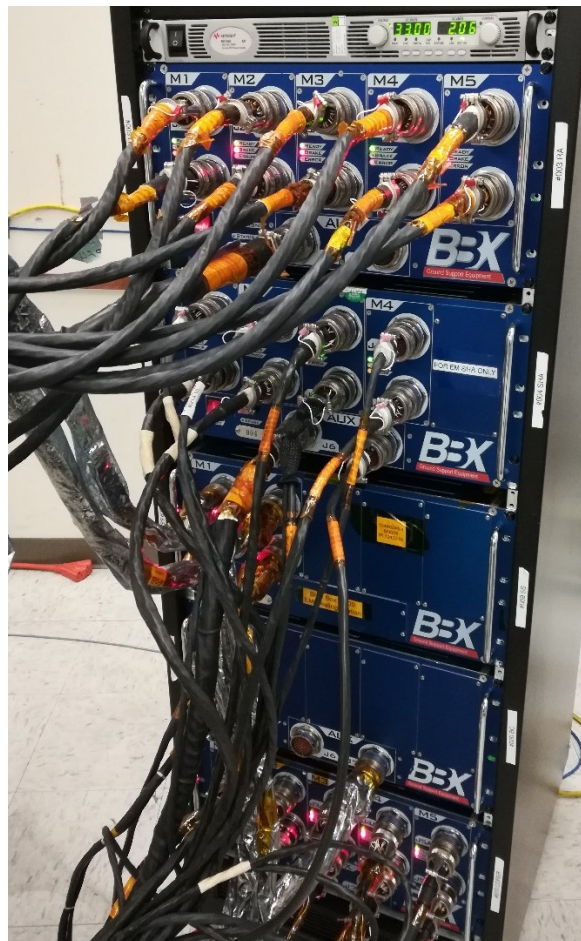
Figure 5-9 Five daisy chained Blue Boxes and their respective harnessing.

5.3.6. Inductor compensation

The long harnesses connecting the EGSE to the test article added up to 0.25Ω of one-way resistance per motor phase for low current motors, less than 2.5A, and about 0.04Ω for motors consuming up to 15A. The flight flex-cabling added additional resistance up to 1.5Ω roundtrip. To compensate for the added resistance, and due to the minimum terminal inductance required for COTS motor controller, the Blue Box architecture employed motor-phase, series inductors to reduce current ripple and tune the electrical time constant of the system (harness + motor phases). These inductors are commonly referred as motor chokes.
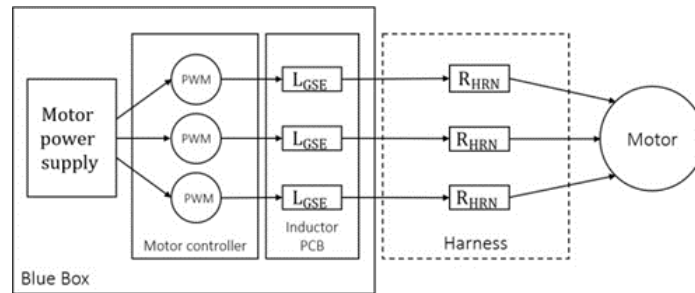
Figure 5-10 Series inductors for motor phases

The inductance of such inductors is of prime importance as it affects the motor's maximum torque at high speed in an inversely proportional fashion. It is therefore necessary to optimize the added inductance to a particular range of values. The following analysis applies to block commutation, which is the commutation used by the SCS flight motor controllers which this EGSE emulates.

Variable	Description	Units
I_M	Motor current	A
V	Motor controller voltage	V
L_M	Motor inductance phase-to-phase	H
R_M	Motor resistance phase-to-phase	Ω
L_{GSE}	Added inductance	H
R_{HRN}	Cable resistance	Ω
ω_M	Motor speed	RPM
K_v	Motor velocity constant	RPM/V
K_t	Motor torque constant	Nm/A
C_S	Number of commutation steps	-
M_P	Motor number of poles	-
T_{PWM}	Motor controller PWM period (0.00005s for ELMO)	s
T_{Comm}	Electrical revolution period dived by the number of poles and commutation cycles	-
τ_{total}	Total electrical time constant	-

Table 5-3 Variables for added inductance calculations

By using an LR circuit model to add the time constants of the motor and the harness, the total time constant of the system is calculated as:

$$\tau_{total} = \frac{L_M + 2L_{GSE}}{R_M + 2R_{HRN}} \qquad (1)$$

The following equations were then used to optimize the added inductance:

$$\frac{\tau_{total}}{T_{PWM}} = \frac{(L_M + 2L_{GSE})}{(R_M + 2R_{HRN})\,T_{PWM}} \qquad (2)$$

$$\frac{T_{Comm}}{\tau_{total}} = \frac{(R_M + 2R_{HRN})\,60}{(L_M + 2L_{GSE}) \times \omega_M\, M_P\, C_S} \qquad (3)$$

The optimization goal was to ensure that the added inductance complied with:

$$T_{PWM} \times 10 < \tau_{total} < T_{Comm} \times 10 \qquad (4)$$

The lower bound in (4) ensures ample stability margin in the motor controller's current control loop. The upper range in (4) attempts to ensure the motor can operate at the desired maximum speed. However, this condition does not guarantee that the motor will be able to sink the necessary current at a certain speed to achieve a certain torque. The maximum theoretical motor current, achieved when the PWM duty cycle is 100%, can be calculated as a function of the bus voltage and motor speed:

$$I_M(t) = \left(\frac{V - \frac{\omega_M}{K_v}}{R_M + 2R_{HRN}} \right) \left(1 - e^{-\left(\frac{t}{\tau_{total}}\right)} \right) \qquad (5)$$

Knowing the motor torque constant, K_t, one can then calculate the torque at a specific speed and ensure the added inductance allows the system to reach the torque/speed combination, at a given voltage. For the Blue Box EGSE, added motor-phase series inductance ranged from 0 to 1360 µH (MURATA 6000A).

This analysis proved useful when troubleshooting a deployed Blue Box that changed configuration from a short harness to a long harness. For the short harness, no motor chokes were used and dynamometer tests showed nominal results. When the long harness was introduced, series inductors were utilized which showed a limitation on motor torque. Raising the bus voltage, from 28C to 32V, allowed the motor to reach nominal torque.

5.3.7. Safety and protections

The "do no harm" requirement on the EGSE forced additions to the Blue Box circuitry to ensure that any failures on the EGSE did not cause damage to the test article. Previous implementations of flight EGSE at JPL employed traditional fuses along with discrete clamping circuits (OVP-XXG) to protect for overvoltage and overcurrent events. It was known that the traditional fuses employed to protect against such events blew on a regular basis and caused the continuous increase of the fuse rating to enable operations. This behavior was not desirable. Furthermore, these devices were hard to characterize and tune.

The Blue Box EGSE employed eFuses based on the LTC4368 IC to protect against over voltage and over current events. The IC provided several features not available on traditional OVP modules, such as undervoltage lockout, digital enable/disable/reset, and a fault monitoring signal. A low pass filter could also be employed to tune the response characteristics of the eFuse, similar to a "slow-blow" fuse. Furthermore, eFuses could be tested and reset prior to delivery, ensuring the nominal operation of a safety-critical element on the Blue Box. eFuse's protected the following elements on the Blue Box:
- Motor controller power input
- Hall sensor 5V rail

- Heaters
- Brakes
- Strain gauge excitation

For a fully populated Blue Box, up to 26 eFuse's actively protected the elements mentioned previously.
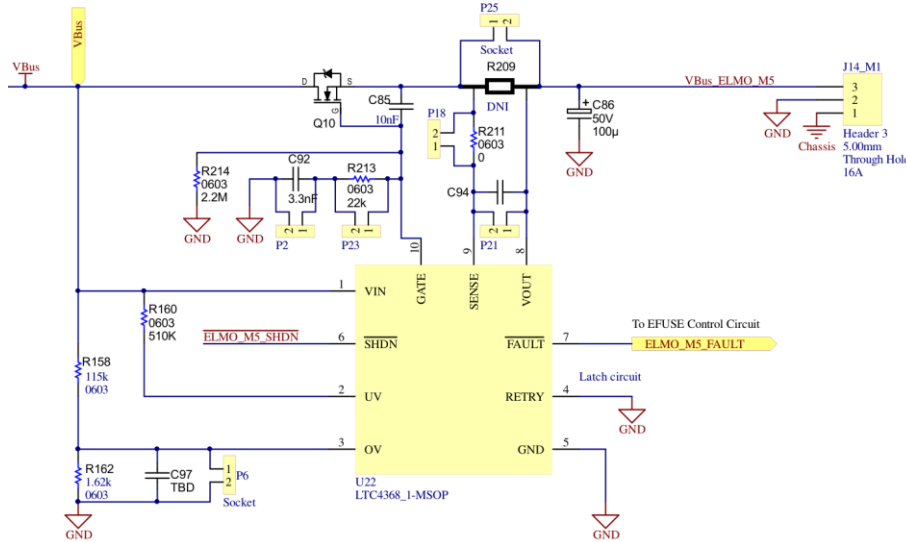
Figure 5-11 eFuse schematic excerpt. Unprotected power, VBus, on the left, protected output on the right. Notice passive low pass filter between R209 and the SENSE pin of the IC.

5.3.8.   Safety microcontroller

The safety microcontroller, ATMEGA328P, handled all fault responses, ensured nominal higher-level communication and all other sequencing aspects on the EGSE. A watchdog timer ensured firmware crashes rebooted this microcontroller. EEPROM registers were used to save the state of the EGSE ensuring a faulted state persisted between reboot cycles. Several interfaces to this microcontroller where required to ensure a reliable and safe system:

- The eFuse's control and monitoring signals were interfaced via MCP23S117T port expanders. The microcontroller had access to the fault signal of each eFuse but only had a global enable/disable/reset control signal.
- Control on the external power supply state (enabled/disabled) via an external safety relay (Phoenix contact 2981813). The relay was triggered by a digital output of the microcontroller.
- An analogue to digital converter channel on the microcontroller was used to measure the external power supply voltage via a resistive voltage divider in the distribution PCB.
- The microcontroller continuously communicated its state with the higher-level software via an RS-232 Beckhoff terminal, EL6001.
- The state of a switch in the front panel of the Blue Box. The switch was used to clear faults and bypass certain safety features when troubleshooting.
- Heartbeat signals in the form of 500Hz TTL-level square wave generated by each motor controller.
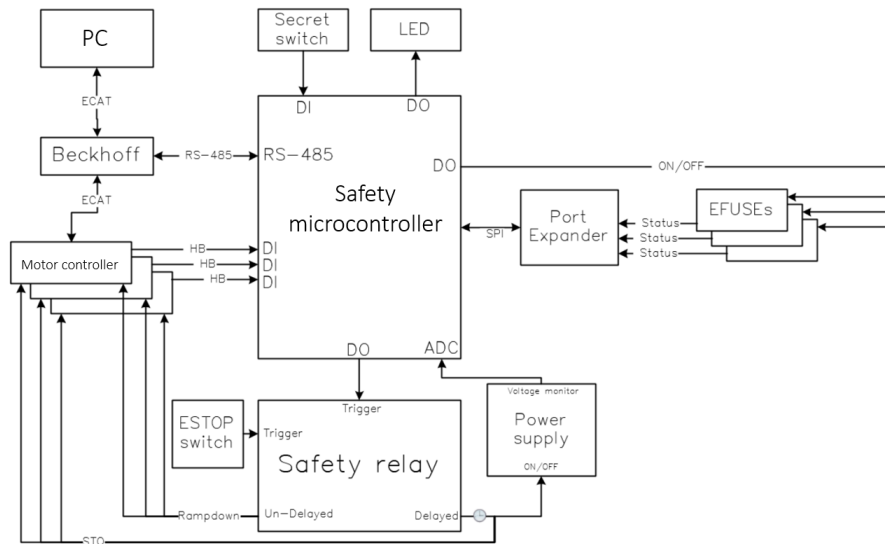
Figure 5-12 Safety microcontroller block diagram

Emergency stop event – The sequence of events after an operator pressed the emergency stop button was handled by the safety microcontroller and proved to be non-trivial. The subset of SCS actuators which were equipped with a brake, were able survive a reduced number of sudden, brake engagements when the motor shaft was spinning. This abrupt stop of the actuator was to be avoided. Since the brakes stopped the motor shaft when power was removed, abruptly removing power to the motor and brake system would cause the undesirable, hard, brake engagement. For this reason, a power sequencing strategy was developed for quickly stopping the system in case of emergency while still ensuring no fault cases could cause further motion.

An ESTOP event could be triggered, either by the external physical ESTOP button, by higher level software of by the safety microcontroller itself. Once triggered, the safety microcontroller performed the following sequence of events:
1. Toggle the safety relay input.
   a. The safety relay un-delayed output then toggled a digital input on the motor controller, the ramp down signal. This was registered by higher level software which then commanded a controlled ramp down in speed to any spinning motor. The controlled ramp down attempted to reduce the speed of the motor as much as possible prior to the brake engaging the motor shaft.
2. After the safety relay tunable delay, 0.25-1 seconds, expired, the delayed output of the relay toggled the safe-to-operate pins on the motor controllers and disabled the external power supply.
   a. Toggling the safe-to-operate pin effectively disables the output stage of the motor controller. The motor is then effectively in free-spin.
   b. By disabling the power supply, power was cut to both the motor controller and the brake driving circuitry. The brakes then engage and stop the motor shaft.

Step 2 in the sequence ensured that no fault scenario could result in continued motion. Although unlikely, this secondary step protected against motor controller firmware crashes, or electrical faults on its output stage.

The ESTOP event could be cleared, by releasing the ESTOP button, or higher-level software. Once cleared, the safety microcontroller toggled the safety relay which then enabled the external power supply and toggled the safe-to-operate and ramp down signals of the motor controllers.

Heartbeat protection: Due to a particular anomaly suffered with the specific model of motor controller used, in which a motor phase was continuously and uncontrollably energized, a protection against motor controller firmware crashes was added to the system. This protection consisted on continuously ensuring the presence of a heartbeat signal generated by the motor controller via high level software.

When operating, higher level software continuously commanded toggling the state of a digital output on each motor controller. This effectively created a software-driven ~500Hz square waveform, the heartbeat signal. The presence of the heartbeat ensured higher level software and the motor controller firmware were operating nominally. A loss of communication in the EtherCAT bus, which communicates motor controllers to higher level software, would trigger an absence of the heartbeat signal. The heartbeat signal of each motor controller was read by a digital input of the safety microcontroller and its abrupt absence would trigger an ESTOP event. This ensured that if the motor controller firmware, higher-level software, or the communication bus crashed, an ESTOP event was automatically triggered.

5.3.9. Assembly and test

To efficiently assemble the 30+ EGSE systems, an assembly line approach was utilized. The process started with configuring the different PCBs with a reduced set of passives to ensure compatibility with each specific actuator. This step set eFuse current levels, resolver excitation parameters and motor series inductors. PCBs were tested to ensure each function and protection behaved nominally. A testbed mimicking the actuators driven by the EGSE was utilized for this purpose. The PCBs were then installed onto the Blue Box chassis. Once the internal wiring of the box was completed, a box-level checkout procedure was performed. The same actuator-mimicking testbed was utilized to ensure a fully assembled system performed nominally. The box-level checkout aimed to detect any deficiencies in the workmanship of the box such as mis-wired connectors or contacts. Higher level software was also involved in this checkout to ensure software safety parameters and the protection circuitry in the box interacted nominally.
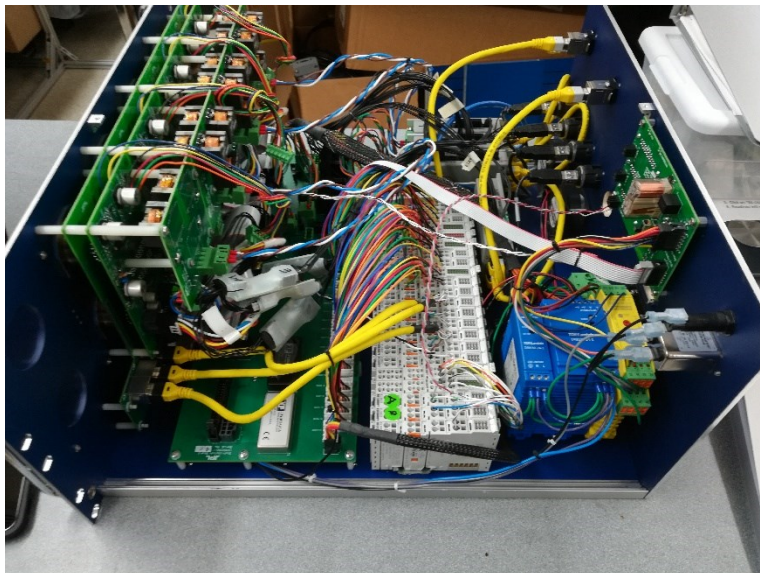
Figure 5-13 4-actuator channel Blue Box with complete internal harnessing.

5.3.10. Deployment and venues

Members of the JPL Quality Assurance team supervised the box assembly and ensured adherence to procedures and proper workmanship. Once an EGSE system was fully checked out, it was deployed to the appropriate venues, see Figure 5-14. Test venues that this EGSE supported included:

- Lab benches to do unsophisticated low-level actuator tests.
- Dynamometer facilities which characterized in detail the performance of the SCS motors. Dynamometer tests included swings in temperature to verify performance at hot and cold.
- Ultra-clean cleanrooms for operation of clean actuators. The stringent planetary protection requirements of the SCS required the use of ultra-clean cleanrooms. To comply with the cleanliness requirements, the external surfaces of the EGSE were thoroughly cleaned with isopropyl alcohol. Surfaces with paint or other outgassing prone coatings, were sealed with Kapton tape and anti-static metallized foil. The harnesses connecting the EGSE to the test article were also surrounded by Kapton and metalized foil to reduce outgassing concerns. The EGSE was then energized while inside the cleanroom passthrough for 48 hours. This ensured the fans in the EGSE and auxiliary devices evacuated all the "dirty" air from inside the enclosures.
- Thermal vacuum chambers that ensured the SCS system operated nominally under a relevant environment. During these tests, the Blue Box system was operated continuously for over 3 weeks.
- ATLO high bays at JPL and KSC as part of the rover assembly process. The robotic arm and the Sampling Handling arm of the SCS had to be moved to specific poses during assembly. The Blue Box EGSE was used for this purpose.
- External venues at Lockheed Martin and Maxar's MDA to support testing while SCS subsystems were assembled.
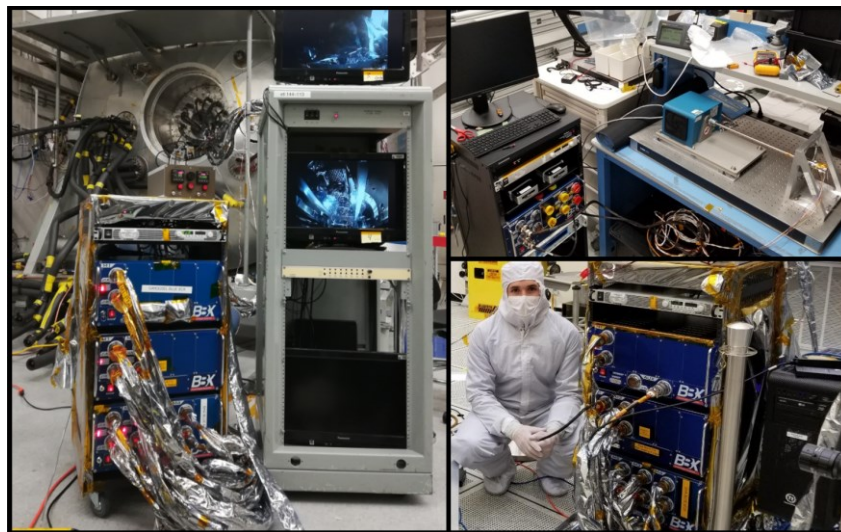
Figure 5-14 Subset of Venues where Blue Box was deployed. Left: Thermal Vacuum testbed. Top right: Dynamometer test setup. Bottom right: Ultra-clean cleanroom

5.3.11. Anomalies

During the 3-year span of time when the Blue Box was active and deployed, ~30 formal anomalies were encountered, documented and resolved. The root cause of the anomalies ranged from design errors, harnessing workmanship issues, EMI/EMC, software and firmware bugs, motor controller deficiencies and impedance mismatches. A representative subset of these anomalies is described.

Mounting screw electrical leak: For a particular deployed system controlling the main robotic arm, at some point in time, the brake current telemetry signal sporadically started showing anomalous noise

which then triggered its corresponding eFuse. At first, it was believed EMI/EMC was causing the brake current noise. The long EGSE harness, the usual suspect for EMI/EMC issues, were inspected and connection broken at different points to help troubleshooting. The root cause of this anomaly was determined to be an electrical leak, kΩ, between the chassis or shield signal in the Blue Box and motor phases caused by the metallic PCB mounting screws piercing through he PCB solder mask due to insufficient clearance. The mechanical nature of the root cause explained the sporadic nature of the symptoms. Plastic washers around the PCB mounting holes were use to avoid piercing the solder mask as PCB redesign was not practical.

Capacitive coupling on harness: During initial stages of SCS actuator testing, the drill corer system showed detrimental noise on the hall signals when the corer spindle motor was spinning. The noise was severe enough to cause faulty commutation and motor controller faults. Troubleshooting efforts showed that the hall signal noise was present even when the motor phases of the spindle motor were not connected. This implied a voltage driven source for the noise rather than current. Due to the relatively large current consumed by the spindle motor, its harness had 12 sets of 20 AWG twisted triplets wire bundles to connect the motor phases to the EGSE. Since each twisted triplet was individually shielded, the capacitive coupling between the shields and the motor phases was significant, about 15nF. The hall sensor signals were also shielded, providing a capacitively coupled path between motor phase and hall signals. The root cause was determined to be that the PWM voltage driving the motor capacitively coupled to the halls via the extensive common shield between these signals, introducing noise. The solution proved to be grounding the shield on both sides of the 50-foot harness. The reconfigurable eyelets on the harness proved handy to perform this solution with ease.

Damaged MOSFET when checking out brake circuit: Due to the redundant nature of the dual-coil brakes on the SCS, the secondary coil was tested late in the V&V campaign. For some deployed boxes, when attempting to energize the secondary brake coil it was seen that the brake did not disengage the motor shaft. It was determined that the EGSE could not drive a brake-mimicking solenoid connected directly at the front panel of the box. This pointed that the problem was internal to the box. After further troubleshooting it was determined that the driving MOSFET for the brake suffered permanent damage. The test log and documentation for that specific EGSE system was useful to determine the root cause of the anomaly as a checkout procedure deficiency. During box level checkouts, it was found out that the test operator purposely triggered the eFuse protection circuitry of the brake by shorting the live brake output with a wire, negligible resistance. This caused a surge of current, which triggered the brake eFuse as expected, but also surpassed the current rating of the MOSFET. The protection check was performed after the brake functional test, therefore the MOSFET failure was not detected as part of the checkout procedure. The solution was to update the checkout procedure to ensure the functional test of the brake was performed after the protection circuitry checks and specifically called to use an appropriate resistor to avoid spurious current surges.

5.4. Conclusions

The Blue Box EGSE system was a vital component for the M2020 SCS V&V campaign. The flexibility and fast-pace production cycle ensured the EGSE system schedule remained compatible with the SCS V&V aggressive schedule. 32 racks were deployed to a variety of venues at JPL and externally. Six boxes were daisy chained together to drive a full system-level version of the SCS composed of 17 actuators total as part of the Qualification Model Dirty Testing (QMDT). 29 anomalies were identified and resolved during the 3-year lifespan of the system.

5.4.1. Lessons learned and *recommendations*

Several particular design choices in the Blue Box system proved to be particularly beneficial:

- The daisy-chainable EtherCAT bus allowed trivial and fast reconfiguration of several boxes. This feature was particularly useful when transitioning from single actuator tests to coordinated motion with a reduced number of actuators, and all the way to a fully assembled SCS with 17 actuators. The high bandwidth capability of this bus allowed to gather the telemetry of all these actuators at 500Hz.
- eFuse-based protections proved easy to work with and more importantly, trivial to repeatably check and ensure proper behavior. The safety microcontroller that monitored and controlled all eFuses was particularly useful to achieve the complex safety responses needed.
- Ranging from stacking Beckhoff I/O units, to the number of motor channels required, modularity proved to be a useful design feature which allowed a wide range of configuration options.

Other design choices posed significant challenges:

- Long harnesses, although necessary in particular test venues, posed problems due to the added electrical parasitics. In particular due to the large number of individual shields employed for each group of signals, which created non-negligible capacitive coupling. More shielding does not always equate to better performance.
- The complex safety response required several iterations on the safety microcontroller firmware and extensive handshaking protocols with the higher-level software. Continuous development of this firmware, while EGSE was deployed, required in-the-field firmware upgrades. The Blue Box did not expose the microcontroller programming interface, a design deficiency. This deficiency complicated firmware upgrades as the boxes had to be physically opened.

5.5. References

[1]   K. Edelberg, P. Backes, J. Biesiadecki, S. Brooks, D. Helmick, W. Kim, T. Litwin, B. Metz, J. Reid, A. Sirota, W. Ubellacker, and P. Vieira, "Software System for the Mars 2020 Mission Sampling and Caching Testbeds," IEEE Aerospace Conference, 2018

[2]   D. Levine, T. Brown, K. Edelberg, W. Ubellacker, S. Brooks, C. Assad, D. Wai, D. Loret de Mola Lemus, and J. Biesiadecki. "Ssdev-Ecat: A Configurable Motion Control Server for Mars 2020 Hardware Testbeds," IEEE Aerospace Conference, 2022

6. Paper #5. NeBula: Quest for Robotic Autonomy in Challenging Environments; An Overview of TEAM CoSTAR's Solution at Phase I and II of DARPA Subterranean Challenge

The presented paper is a reduced version of the published paper which reflects the contribution of the author. Parts in which the author was not a main contributor has been omitted.

6.1. Abstract

This paper presents and discusses algorithms, hardware, and software architecture developed by the TEAM CoSTAR (Collaborative SubTerranean Autonomous Robots), competing in the DARPA Subterranean Challenge. Specifically, it presents the techniques utilized within the Tunnel (2019) and Urban (2020) competitions, where CoSTAR achieved 2nd and 1st place, respectively. We also discuss CoSTAR's demonstrations in Martian-analog surface and subsurface (lava tubes) exploration. The paper introduces our autonomy solution, referred to as NeBula (Networked Belief-aware Perceptual Autonomy). NeBula is an uncertainty-aware framework that aims at enabling resilient and modular autonomy solutions by performing reasoning and decision making in the belief space (space of probability distributions over the robot and world states). We discuss various components of the NeBula framework, including: (i) geometric and semantic environment mapping; (ii) a multi-modal positioning system; (iii) traversability analysis and local planning; (iv) global motion planning and exploration behavior; (v) risk-aware mission planning; (vi) networking and decentralized reasoning; and (vii) learning-enabled adaptation. We discuss the performance of NeBula on several robot types (e.g. wheeled, legged, flying), in various environments. We discuss the specific results and lessons learned from fielding this solution in the challenging courses of the DARPA Subterranean Challenge competition.

6.2. Introduction
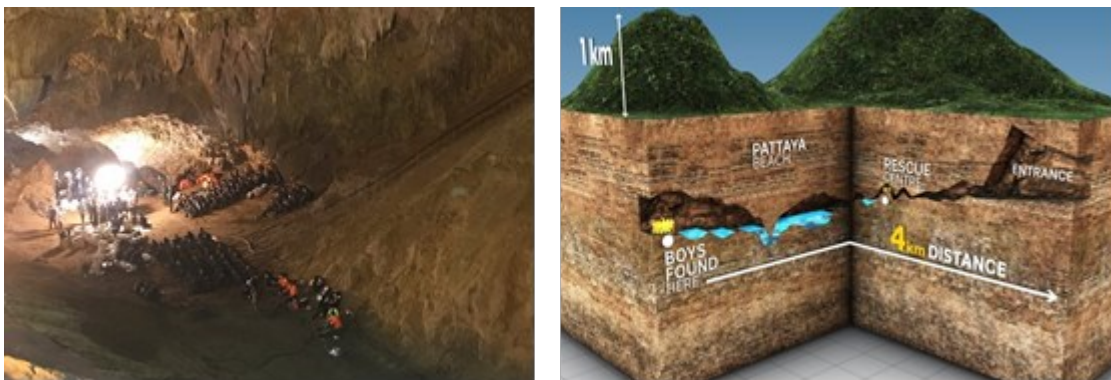
Figure 6-1: Tham Luang cave rescue mission. Figures from [9] and [10].

Robotics and Artificial Intelligence (AI) are transforming our lives, with a growing number of robotic applications ranging from self-driving cars [1], search & rescue [2], healthcare [3] and humanitarian missions [4], to robots under water [5] and robots beyond our home planet on Mars [6, 7] and the moon [8]. Autonomy and AI are empowering these robots to carry out missions autonomously, increasing

efficiency with reduced human risk, saving lives, and accomplishing tasks that are often in hazardous environments too dangerous for human.

Extreme environments: Underground environments are an important example of the type of terrain that imposes a lot of risk for humans, with a wide range of terrestrial and planetary applications. On Earth, autonomous underground exploration is a crucial capability in search and rescue missions after natural disasters, in mining, oil and gas industry, and in supporting spelunkers and cave rescue missions. One prominent example is the Tham Luang cave rescue (Figure 6-1), where the international community aimed at rescuing thirteen members of a football team from 4 km inside a partially flooded cave. Drones equipped with thermal cameras have been flown over Tham Luang to detect possible access points, and an underwater robot was deployed to send information back on the water depth and condition of the cave. However, at that time, no technology existed to autonomously reach the people, map the cave, and scan for people deep underground.

Planetary applications: Beyond our home planet, the research community has identified more than 200 lunar and 2000 Martian cave-related features [11]. Caves and subsurface voids, in general, are of utmost importance in space exploration for several reasons. First, their stable, radiation-shielding environment, and potential to act as volatile traps makes them an ideal habitat candidate for future human exploration [12, 13]. Second, planetary cave environments may harbor life due to their shielding from cosmic rays, and if there is life beyond Earth, deep planetary caves are one of the most likely places to find it. Third, exploring caves provides an unprecedented opportunity for scientists to study planetary volcanic processes and the geological history of planetary bodies. These reasons, among many others, have made subsurface exploration one of the main next frontiers for space exploration [14, 15].

While autonomy and AI technologies are growing fast, challenges still remain for operations in extreme environments. Technical challenges include: perceptual degradation (darkness, obscurants, self-similarity, limited textures) in wholly unknown and unstructured environments; extreme terrain that tests the limits of traversability; mission execution under constrained resources; and high-risk operations where robot failure or component degradation is a real possibility. Most challenging of all, however is the combination of the above features. Further work is needed to push the state-of-the-art to enable systems that can robustly and consistently address these challenges simultaneously.

Contributions: In this paper, we discuss the NeBula autonomy solution and Team CoSTAR's contributions towards addressing some of the challenges in robotic exploration of unknown extreme surface and subsurface environments. We discuss these technologies in the context of the DARPA Subterranean challenge [16], where Team CoSTAR won the Urban competition and ranked 2nd in the Tunnel competition. The videos in [17, 18, 19, 20, 21] depicts some highlights of these runs. As we will discuss in Section 2, this competition pushes the state-of-the-art boundaries in extreme environment exploration in mobility, perception, autonomy, and networking.

6.3. DARPA Subterranean Challenge

The DARPA Subterranean or "SubT" Challenge [16] is a robotic competition that seeks novel approaches to rapidly map, navigate, and search underground environments (Figure 6-2). The competition spans a period of three years. The teams participating in the systems track develop and implement physical systems for autonomous traversal, mapping, and search in various subterranean environments, including mines, industrial complexes, and natural caves.
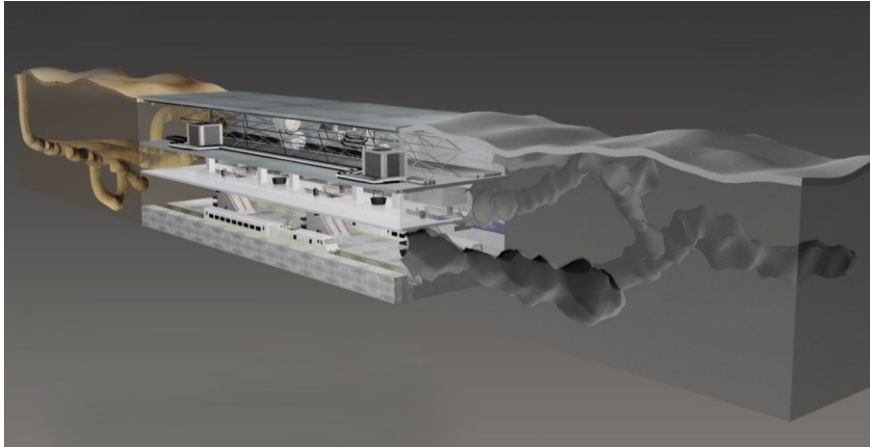
Figure 6-2: The three subdomains in the DARPA Subterranean Challenge: Tunnel systems, urban underground, and cave networks

Illustrative scenarios: The primary scenario of interest for the competition is providing autonomous and rapid situational awareness in unknown and challenging subterranean environments. The layout of the environment is unknown, could degrade or change over time (i.e., dynamic terrain), and is either impossible or too high-risk to send in personnel. Potential representative scenarios range from planetary cave exploration to rescue efforts in collapsed mines, post-earthquake search and rescue missions in urban underground settings, and cave rescue operations for injured or lost spelunkers. Additional scenarios include missions where teams of autonomous robotic systems are sent to perform rapid search and mapping in support of follow-on operations in advance of service experts, such as astronauts and search/rescue personnel. These scenarios present significant challenges and dangers that would preclude employing a human team, such as collapsed and unstable structures or debris, a presence of hazardous materials, lack of ventilation, and potential for smoke and/or fire.

6.3.1. Technical Challenge Elements

The competition is intended to push the boundaries of the state-of-the-art and state-of-the-practice across various challenge elements, including: austere navigation, degraded sensing, severe communication constraints, terrain obstacles, and endurance limits.

All-terrain Traversability: The environment includes multiple levels, loops, dead-ends, slip-inducing terrain interfaces, and a range of features and obstacles that challenge robot's mobility. Examples of terrain elements and obstacles include constrained passages, sharp turns, large drops/climbs, inclines, steps, ladders, mud, sand, and/or water. The environments may also include organic or human-made materials; structured or unstructured clutter; and intact or collapsed structures and debris.

Degraded Perception and Sensing: The environment includes elements that range from constrained passages to large openings, lighted areas to complete darkness, and wet to dusty conditions. Such environments with limited visibility, difficult and expansive terrain, and/or sparse features can lead to significant localization error and drift over the duration of an extended run. Perception and proprioceptive sensors will need to reliably operate in these low-light, obscured, and/or scattering environments while having the dynamic range to accommodate such varying conditions. Dust, fog, mist, water, and smoke are among the challenging elements.

Constrained Communication: Limited line-of-sight, radio frequency (RF) propagation challenges, and effects of varying geology in subterranean environments impose significant impediments to reliable networking and communications links. Teams in this competition consider innovative approaches to overcome these constraints, including novel combinations of hardware, software, waveforms, protocols, distributed or dispersed concepts, and/or deployment methods.

Endurance and Power Limits: To succeed in accomplishing the mission goals, teams need to be capable of a team-aggregated endurance of 60-120 minutes. This aggregate endurance requires novel deployment concepts, energy-aware planning, heterogeneous agents of varying endurance, energy

harvesting or transfer technologies, and/or a combination of various approaches to overcome the various challenge elements.

6.4. Concept of Operations

In this section, we briefly go over NeBula's ConOps (Figure 6-4) for exploring unknown extreme terrains under time constraints. In order to simultaneously address various challenges associated with exploring unknown challenging terrains (Section 2.2), we rely on a team of heterogeneous robots with complementary capabilities in mobility, sensing, and computing.

Robot Capabilities: Figure 6-5 shows the robots we have deployed. The capabilities of these robots drive the ConOps design process. Tables 1, 2, 3 summarize our heterogeneous robot capabilities from mobility, sensory, and computing perspectives. Our ConOps induces specific combinations of mobility-sensor-computer, defining the robots we deploy in the environment to satisfy the mission objectives. The payload capacity of each robot is directly correlated with the sensory capacity; larger payload capacity allows for a larger sensory suite. Also, the energy/battery capacity, and desired endurance on each robot is correlated with their processing capabilities; typically, larger robots are able to carry larger batteries and more powerful computing resources. Some of these mobility-sensor-computer combinations are discussed in Section 12.
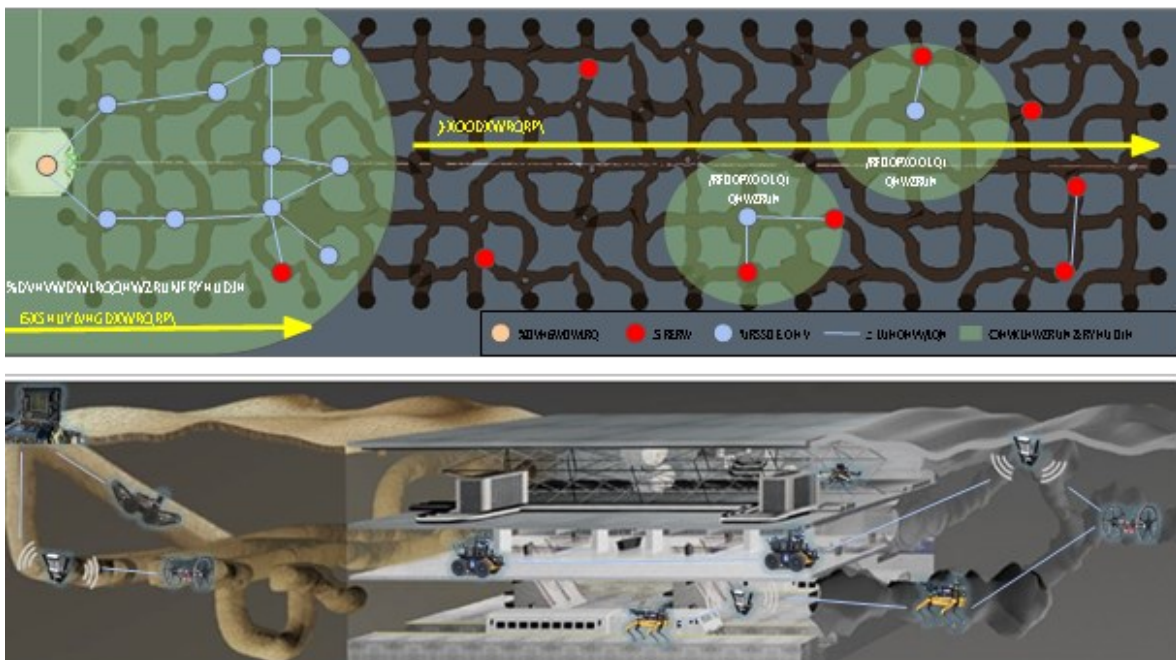
Figure 6-4: NeBula's Concept of Operation. Top: Bird's eye view of autonomy in cave. Bottom: Perspective view with our robots and different environments.

ConOps: Our Concept of Operations (ConOps) utilizes a heterogeneous set of platforms (see Table 6-1 and Figure 6-5). In the following, we describe several steps of an example illustrative mission ConOps.

5. Vanguard Operations: As the robots enter the environments, they explore the frontier with vanguard robots with highly capable sensing for mapping and artifact detection.

6. Mesh Network Expansion: As robots start the mission they aim at maintaining communication with the human supervisor by creating and extending a wireless mesh network inside the environments of networking. Ground robots do so by deploying communication pucks like breadcrumbs, and aerial scouts can self-deploy for either comms relays or added sensing. Mission autonomy will decide where and how to deploy these breadcrumbs.

7. Leaving the Mesh Network: The environment is highly communication-denied. Due to the large scale, complexity of the environment, and capacity of robots to carry communication nodes, the mesh network reach is typically limited to the parts of the environments in the vicinity of the base station (i.e., environment entrance). Hence, the robots will leave the communication network range soon and, for the most part, carry out a fully autonomous mission.

8. <u>Autonomous Mission</u>: Robots perform search, mapping, and exploration. Autonomous mission guides them to the rendezvous points to exchange information with each other, or they come back to the mesh network to exchange information with the base station.

9. Dynamic Task Allocation: Robots continue simultaneous frontier exploration. They autonomously monitor the

   (a)   state of the robot team that includes: (i) health, battery, and functionality level of the assets, (ii) robot locations, (iii) the information value (e.g., the numbers of detected artifacts) on each robot.

   (b)   state of the world that includes what robots learn about the environment, e.g., geometric and semantic maps,

Figure 6-5: Team CoSTAR's NeBula-powered robots

   (c)   state of the mission that includes: (*i*) the remaining mission time, and (*ii*) margin to the desired mission output, (*iii*) acceptable risk thresholds.

   (d)   state of communication: (*i*) network connectivity, throughput, etc., (*ii*) how long each robot is out of the comm range, (*iii*) location of comm nodes

Given these states, the mission planner will decide to deploy new robots, re-task or re-position active robots in the environment.

10. <u>Team Behaviors</u>: Vehicles and team formation are configured during the mission. Examples include:

   (a)   Return to Base, when a battery swap is needed, optimal, and possible at base,
   (b)   Return to Mesh Network, to ensure the data are communicated, then continue,
   (c)   Explore Frontier, continue as is, aggressively prioritizing coverage,

(d)   Act as a Data Mule: to retrieve data from a vehicle who cannot come back to the mesh network (due to limited battery, health, speed, etc), faster and healthier vehicles can act as data mules to carry the information between others agents and the mesh network.

11. Heterogeneous Coverage: These behaviors continue until the entire course is explored. Due to the heterogeneous capabilities of the robots from mobility, sensing, and computation perspectives, the autonomy might dispatch different robots to the same parts of the course. This is to increase the confidence and coverage in mapping and artifact detection by providing multimodal information (e.g., thermal, radar, etc) about the environment elements. For example, the drone might have reached and searched parts of the course but given its limited sensing capabilities, autonomy will dispatch a ground robot to get a second vote on an artifact before submitting it to the server. All the data is submitted to the server prior to the end of mission time.

6.5. NeBula Autonomy Architecture

Resiliency is a key requirement to enable a repeatable and consistent robotic autonomy solution in the field. *To enable a resilient autonomy solution, NeBula takes uncertainty into account* to cope with unmodeled and unknown elements during the mission.

Table 1: Heterogeneous NeBula-powered Mobility Modes

Robot Type	Deployed In	Energy capacity	Payload capacity	Comm	Speed	Mobility	Endurance
Legged robots	Urban	Mid	Mid	Mid	Mid	Mid	Mid
Hybrid (ground/aerial)	STIX	Low	Low	Low	High	Mid-High	Low-Mid
Wheeled	STIX, Mine, Urban	High	High	High	Low	Low	High
Drones	STIX, Mine	Low	Low	Low	High	High	Low
Tracked	STIX	High	Mid	Mid	Low	Low-Mid	Mid-High
Fast small rovers	Mine	Mid	Mid	Low	High	Low	Mid
Aggregated robot team	All events	Shared/Synergistic	Shared/Synergistic	Shared/Synergistic	Aggregated	Aggregated	Aggregated

Table 2: Heterogeneous NeBula Sensing Modalities (the values are based on our specific ConOps)

Sensors	Exteroceptive									Proprioceptive		
	Lidar	Vision	Radar	Thermal	Sonar	IR Depth	CO2/Gas	Wi-Fi	Sound	Contact/Force	Encoder	IMU
Accuracy	High	Mid	Low	Low	Low	High	Low	Low	Low	Low	Mid	High
Power efficiency	Low	High	High	Mid	Mid	High	High	High	High	High	High	High
Size/weight efficiency	Low	High	High	Low	Mid	High	High	High	Mid	Mid	Mid	High
Range and FOV	Mid	High	Low	High	Low	Low	Low	High	Mid	-	-	-
Dark/fog/smoke/dust	Mid	Low	High	High	Mid	Mid	-	-	-	-	-	-

Table 3: NeBula Processors

Processors	Micro-controllers	Snapdragon	Intel NUC	Nvidia Xavier	AMD
Compute	Low	Low	Mid	High	High
Power consumption	Low	Low	Mid	High	High
Size efficiency	High	High	Mid	Low	Low

Motivation/Insight: An important (if not the most important) cause of the brittleness of today's autonomy solutions is the disjoint design of various subsystems. Traditionally, when designing or advancing the performance of a certain module, the typical assumption is that the rest of the system functions properly and nominally. When it comes to real-world deployment, these assumptions typically break due to the discrepancy between the computational models and real-world models. This introduces uncertainty in the perception, inferences, decision-making, and execution, potentially leading to suboptimal behaviors.

Key principle for resilient autonomy architectures: Focused on fielding autonomy in challenging environments, NeBula is built on a fundamental principle that: "To achieve resilient autonomy, the decisionmaking, inference, and perception modules must be reciprocal and tightly co-designed." This implies reasoning over joint probability distributions across various component-level states as opposed to marginal distributions over a set of disjoint system states. Contrary to the typical sense → infer →

plan → act sequence in autonomy solutions, NeBula architecture is built on a plan-to-(sense → infer → act) loop, where the planner dynamically *plans for* the acquisition of sufficient sensory information and *plans for the quality of representation* required to enable resilient and uninterrupted missions within the prescribed mission risk thresholds. NeBula's joint perception-planning is formulated as an uncertainty-aware belief space planning problem. Belief captures the probability distribution over system's states including the robot pose, environment state, measurements, team coordination state, health state, communication state, etc. Planning over joint beliefs and taking cross-component uncertainty into account (which describes the interaction of connected modules), NeBula allows for each module to not only be robust to uncertainties within its own subsystem but also resilient to uncertainties in the integration process, resulted from imperfections and off-nominal performance of connected modules.

Illustrative example (Perception-aware planning under uncertainty): Simultaneous localization and mapping (SLAM) is a fundamental problem in robotics that aims at simultaneously solving the localization problem ("where is the robot?") and the mapping problem ("what does the environment look like?"). This is a very well studied problem and it is well-known that solving SLAM (i.e., incorporating joint probability distributions between localization states and environment states) typically leads to optimal and resilient inference, whereas solving localization and mapping separately and putting their solutions together is suboptimal and can lead to a brittle inference system. Analogous to SLAM philosophy, NeBula extends this concept from pure inference to "joint inference and decision-making" (Fig. 6). For example, NeBula develops solutions where mapping and planning are solved simultaneously using SMAP (simultaneous mapping and planning) to achieve resilient traversability and risk-awareness. Similarly NeBula develops SLAP (simultaneous localization and planning) solutions where localization uncertainty is taken into account in the planning phase using belief space planners. Solving these joint problems typically leads to behaviors where the autonomous system is intelligently planning proactive actions to improve the "inference quality" (e.g., world model or robot model) and reduce uncertainty to the levels necessary to achieve mission goals within the prescribed risk thresholds. This is in contrast to typical solutions where the relationship is one-way and the inference module serves the decision-making modules, and decision-making components react to inference output.

Figure 6-6: Illustrative example of joint inference and decision-making in NeBula's low-level navigation system. Denoting the state domain of the localization by pose x, mapping by map state m, and planing by policy parameters u, SLAM, SLAP, and SMAP aim at solving for (i.e., estimating or predicting) the joint distributions $p(x,m)$, $p(x,u)$, and $p(m,u)$. The full joint problem, SPLAM (simultaneous planning, localization, and mapping) solves for the probability distribution $p(x,m,u)$.
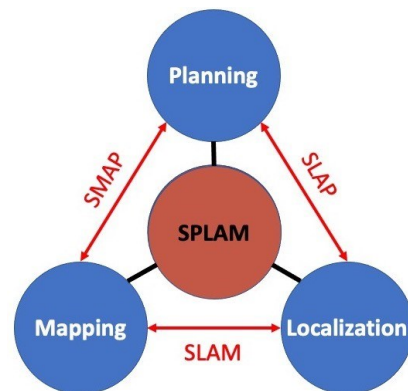
Modularity and scalability: In addition to resiliency, NeBula focuses on a modular and scalable framework. This requirement is driven by missions carried out by a team of networked heterogeneous robots. Each robot has different mobility (e.g., wheeled, legged, aerial, hybrid), sensing, and computational capabilities (e.g., Section 12). NeBula provides appropriate abstraction to allow for re-usability and agnosticism to the specific robot and hardware. Any low-level hardware-specific modules should be properly isolated to increase the re-usability of software. Further, NeBula supports networked systems where agents are intermittently losing and re-establishing communications, and sharing knowledge with each other and with the base station, enabling large-scale environment exploration with a limited number of robots. Each robot has a level of local autonomy to act individually when it is disconnected from the rest of the team.

System architecture: Figure 6-7 illustrates the NeBula's high-level functional block diagram, and will serve as a visual outline of the sections of this paper. The system is composed of multiple assets: mobile robots, stationary comm nodes, and a base station, each of which owns different computational and sensing capabilities. The base station acts as the central component to collect data from multiple robots and distribute tasks, if and when a communication link to the base station is established. In the absence of the communication links the multi-asset system performs fully autonomously. The fundamental blocks are:

- *Perception* (Section 5, 6, 7): Perception modules are responsible to process the sensory data and create a world model belief. The local perception modules (Section 5) provide the odometry and state estimation information needed for local navigation, such as state (pose, velocity) and traversability maps. The global SLAM (simultaneous localization and mapping) module, in Section 6, tracks the robot's position within a globally consistent frame while building a 3D map of the environment. The semantic understanding and artifact detection module (Section 7) adds semantic information to the map and finds objects of interest from the environment, and in conjunction with the global localization module reports their location.

- *Planning* (Section 8, 9, 11): Planning modules will make onboard decisions based on the current world belief. The planning modules are composed of multiple layers. The highest layer is the mission planning module (Section 11) which runs a mission according to its specifications, generates global goals for each robot, and allocates tasks to different robots. The second layer is the global motion planning layer (Section 9), responsible for exploration, search, and coverage behaviors in global scale and large environments. It makes plans to safely move the robot to a goal assigned by the mission planner. It also enables autonomous exploration of the environment in order to increase the knowledge and confidence about the world-belief. The third layer is the traversability and local navigation component (Section 8), responsible for analyzing how and with what velocities different terrain elements can be traversed. It quantifies the motion risk, and optimizes/replans local trajectories with high frequency to enable aggressive traversability in obstacle-laden and challenging environments, while ensuring the risk levels stay within the prescribed mission specifications. NeBula abstracts motion models, enabling the planning stack to be robot-agnostic and to support heterogeneous mobility platforms.

- *World Belief*: This block includes a probabilistic model of the world. It is jointly constructed by perception and planning modules, and enables a tight-integration between these modules leading to perception-aware behaviors. World belief extends the traditional state database concept to a belief database, where we maintain probability distributions over various state domains as well as joint probability distributions across multiple domains. It includes belief over robot pose, environment map, mission state, system health, information roadmap, among other state domains. There are multiple variations of the world belief: (i) local to each robot, (ii) shared belief across robots, and (iii) predicted belief to assess future risk and performance to enable making perception-aware and uncertainty-aware decisions. During exploration tasks, robots develop their own local world models based on what they perceived with their limited sensor input. They generate the world model as an abstract representation of spatial and temporal information of their surrounding environment (e.g., maps, hazards) and internal state (e.g., pose, health). This world belief is internally predicted to enable uncertainty-aware decisions and actions based on this predicted model. The shared world model is synchronized among the robots and the base station using asynchronous bidirectional messaging with the publish/subscribe paradigm. The discussion of world belief is distributed across all sections of the paper.

- *Communications* (Section 10): When possible, communication modules synchronize the shared world models across the robots and the base station. To cope with the dynamic and unstable nature of the underlying mesh network, the communication manager is responsible to provide reliable message transfer with buffering, compression, and re-transmission. The modules also

provide capabilities to maintain a mobile ad-hoc network using radio devices. Static communication nodes can be dropped from particular robots to help forming a network.

- *Operations* (Section 11): Operation modules aid the human supervisor to effectively monitor the system performance and interact with it if and when communication links are established. One of the main roles is the visualization of complex world belief in a human-recognizable form. In the nominal operation scenarios, the human operator only interacts with the system by updating the world belief, when needed and when possible.

Over time, each layer adapts to the collected data as well as to improvements of models in other layers. **Current Implementation Status**: NeBula is a growing and evolving framework. Its current version (in 2020) has been deployed in several large projects for terrestrial and planetary applications. It has enabled autonomous operations on various vehicle types including 1) wheeled rovers, 2) legged robots, 3) flying multicopters, 4) hybrid aerial/ground vehicles, 5) 1/5th scale race cars 6) tracked vehicles, and 7) fullsize passenger vehicles. We refer to Section 12 for a detailed description of our implementation on these platforms.

6.6. Large-Scale Positioning and 3D Mapping

NeBula's Simultaneous Localization and Mapping (SLAM) solution, called LAMP (Large-scale Autonomous Mapping and Positioning) achieves low drift, multi-robot, multi-sensor SLAM over large scales in perceptually degraded conditions. LAMP produces a consistent global representation of an unknown environment, along with the associated covariances to enable uncertainty-aware solutions across the NeBula system (Figure 6-7). In the context of the DARPA Subterranean Challenge, LAMP achieves the requirement for artifact localization error of less than 5 m over multiple kilometers of traverse. In this section, we will outline the architecture of LAMP, and then describe our approach to multi-sensor SLAM. Finally, we present results from representative field tests.

6.6.1. Subsystem Overview

As outlined in Figure 6-13, LAMP is a factor-graph based SLAM solution, with the following key components: a) an adaptable odometry input that can process individual or fused odometry sources, such as HeRO (Section 5), b) a multi-modal loop closure module, based on LiDAR, visual or semantic features, c) an outlier-resilient optimization of the factor graph, including multi-sensor inputs.

The flow of data starts with the odometry and sensor inputs, which add factors to the graph on the robot. Parallel processes then run loop closure searches and factor-graph optimization. Next, the graph is sent to the base station. The base station merges graphs from each robot into a common multi-robot graph that is further optimized with the addition of inter-robot loop closures. The main output products of LAMP are a set of poses describing the robot trajectory and the location of artifacts, as well as a point-cloud map.
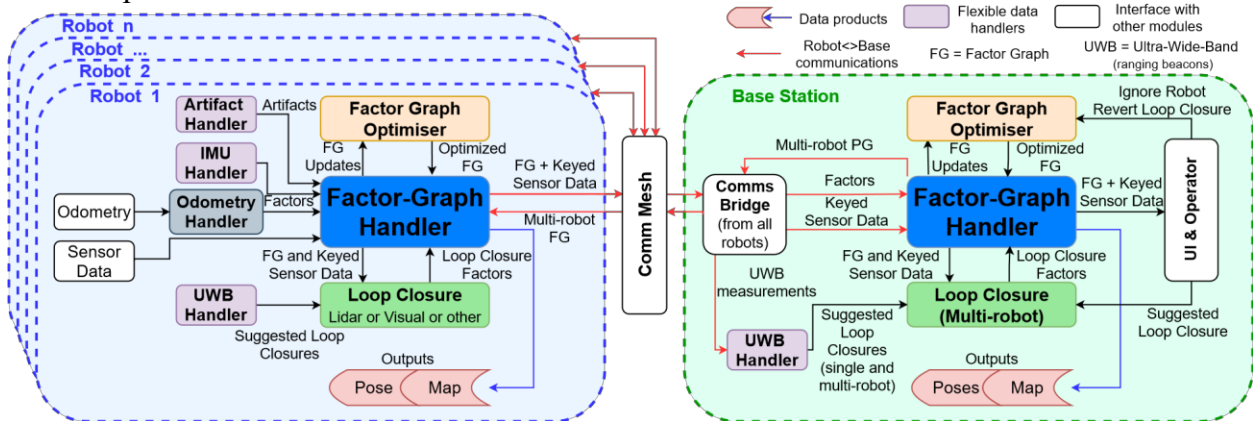
Figure 6-13: LAMP Architecture. Each robot maintains their own factor graph (FG), which can then be fused with a multi-robot team on the base station, using a centralized architecture. The LiDAR and camera data that is used for loop closures and map building (white "Sensor Data" box) is labelled Keyed Sensor Data, being linked with a specific pose-node. Handlers of artifact observations, IMU measurements, and UltraWide-Band (UWB) signals all process data to add constraints to the factor graph. Our robust optimization approach runs in parallel to optimize both the robot and multi-robot factor graphs.

Pose Nodes and Adaptable Odometry Input: To make the factor-graph optimization computationally tractable over large-scale, long-term multi-robot exploration, LAMP utilizes a sparse graph of pose-nodes and edges (Figure 6-14). The edges are obtained from an accumulation of odometry measurements between two consecutive nodes (odometry edges) or from translation and rotation estimates between non-consecutive nodes (loop closures edges, described below). A new pose-node and linking odometry edge is created after travelling more than a threshold translation or rotation. To address the challenge of perceptual degradation for these odometry edges, we use HeRO (Section 5) as the input odometry source.
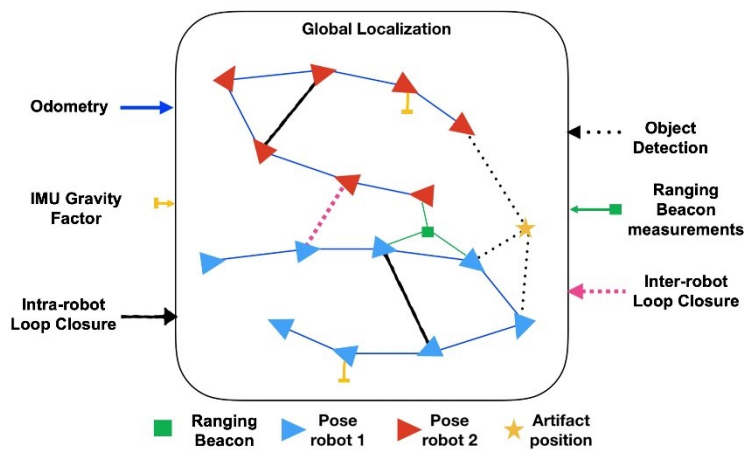
Figure 6-14: Graphical representation of the LAMP multi-robot pose-graph, including odometry factors, interand intrarobot loop closures, gravity factors, ranging beacon measurements and shared observations of landmarks(e.g. artifacts).

Multi-Modal Loop Closures: A crucial capability to reduce the accumulated error in the robot trajectory is loop closure detection: the ability to correctly assert when a robot revisits a previously visited location or known landmark. Loop detection enables the computation of rigid body 3D transformations between non-consecutive pose-nodes that can be added as loop closure edges in the factor graph (Figure 6-14). The multi-modal architecture of LAMP's loop closure module (Figure 6-13) enables a robust and reliable system through the use of different sensing modalities. These loop closure sensing modalities include using lidar data [50], visual data [51] and semantic data [52].

Multi-robot Fusion: NeBula addresses the problem of multi-robot exploration of unknown environments by relying on LAMP's multi-robot architecture. This architecture is centralized, to leverage agents with greater computational resources (such as a base station), however for decentralized applications of NeBula we utilize the techniques described in [53]. In the centralized architecture the agent with the greatest computational capability serves as the central agent to fuse factor graphs constructed by individual robots into a consistent multi-robot graph, along with the associated sensor data (Figure 6-13). The factor graphs are fused using the same multi-modal loop closure modules as on the single robot, but instead of searching for intra-robot loop closures, these modules search for inter-robot loop closures. To further improve localization accuracy, we leverage the computational power of the central agent to perform batch loop closure analysis across the entire graph. This analysis identifies

and computes additional interand intra-robot loop closures to add to the multi-robot graph. The updated multi-robot global graph is then optimized, and periodically sent back to the robots, for each agent to have a consistent global representation of the environment for global planning (Section 9).

Factor-Graph Optimization: Our factor-graph optimization (Kimera-RPGO [51]) uses a robust outlier rejection approach to reject the erroneous loop closures that can occur when operating in perceptually degraded conditions, such as with obscurants and self-similar environments. Kimera-RPGO rejects erroneous loop closures by finding the largest consistent set of loop closures for each set of single robot and inter-robot loop closures, using a consistency graph and max clique search (an adaptation of [54]). The loop closures that are not in the consistent set are discarded prior to optimization (see [50] and [55] for details). The updated factor graph is then optimized with a Levenberg–Marquardt solver that is implemented in GTSAM (Georgia Tech Smoothing and Mapping [46]).

6.6.2. Additional Factors and Multi-Sensor Fusion

LAMP fuses multiple sensing inputs into the factor graph (Figure 6-14) to improve the robustness and accuracy of the SLAM solution. We present four examples here:

1. IMU Gravity Factors: When the robot is stationary, the accelerometers on the IMU can be usedto obtain a robust estimate of the local gravity vector, which is added to the factor graph as a constraint on roll and pitch (yellow factors in Figure 6-14).

2. Landmark Factors: Measurements of distinct landmarks can either be used to detect loop closures or to directly provide constraints to the factor graph. These landmarks fall into two categories.

    (a) Deployed Landmark Factors: These landmarks include visual beacons, ranging beacons or retro reflecting beacons and are deployed from a robot while exploring an unknown environment. For example, we have implemented deployable Ultra-Wide-Band (UWB) ranging beacons in our system (see Section 12.2 for hardware details, and [56] for algorithmic details). The signals from the beacons robustly and efficiently identify loop closures, to seed LiDARor vision-based alignment computations for singleand multi-robot teams (green node and factors in Figure 6-14).
    (b) Environmental Landmark Factors: Existing features in the environment such as signs, salient objects and the shape of junctions (e.g. [52]) can be used as landmarks. For example, we use observations of specific objects, such as backpacks and fire extinguishers (called artifacts in SubT), with sets of range-bearing observations (dashed black lines in Figure 6-14) from the artifact relative-localization module (Section 7). By fusing the object observations into the factor graph we also ensure the most up-to-date global location of those objects for situational awareness (and scoring in SubT).

3. Calibration Factors: At the start of a mission, each robot is aligned with a global reference frame from a combination of LiDAR, IMU and survey station measurements of the robot and a calibration gate (e.g. Figure 6-15). These initial calibration measurements, as well as any additional measurements generated during the mission, are added as constraints to the factor graph.

6.6.3. Metric and Semantic Map Generation

LAMP builds both a geometric and semantic global map from sensor measurements attached to the nodes in the factor graph. Both maps are built by projecting sensor measurements into the global reference frame by using the latest, optimized state of the associated pose-nodes in the factor graph. For the geometric map, these sensor measurements (Keyed Sensor Data in Figure 6-13) are either point clouds (from LiDAR, depth cameras or visual feature tracking) or local occupancy grids. In particular, structures like confidencerich occupancy grids [57], allows for encoding the environmental uncertainty,

which then can be used for perception-aware coverage planning and enabling SMAP-like behaviors [58]. For the semantic map, the sensor measurements are descriptive observations, such as detections of distinct objects (e.g. backpacks, survivors), semantic classifications of 3D spaces (e.g. doorways, stairs) or ambient measurements (e.g. temperature, pressure, gas concentration). The resulting 3D semantic map provides rich situational awareness to the operator of the robotic team, and can be the critical output data product of the overall system. The semantic map is especially important in the context of SubT, where the semantic map primarily consists of the globally localized artifact observations (both objects and ambient measurements), which is exactly the information needed for scoring (Section 7).

6.6.4. LAMP Performance

The performance of LAMP on a single robot dataset from a husky robot equipped with 3 LiDARs is demonstrated in Figure 6-16. LAMP achieves error at less than 0.2% of the distance travelled, with the IMU gravity factors assisting in reducing the z error in the latter portion of the trajectory (Figure 6-16.c). Further single robot tests are summarized in Table 6-5, from the five benchmark datasets shown in Figure 6-17. These benchmarks show LAMP achieving the accuracy better than 5m on all other than the tunnel and cave datasets, which have motion distorted LiDAR measurements. Multi-robot LAMP performance is demonstrated in Figure 6-18 with two huskies deployed in an urban environment. The results demonstrate the benefit of using UWB beacons (Figure 6-18.c) compared to using pure LiDAR-based loop closures. Further results are presented in Section 13. Please refer to [50] for detailed results in tunnel environments, including the impact of
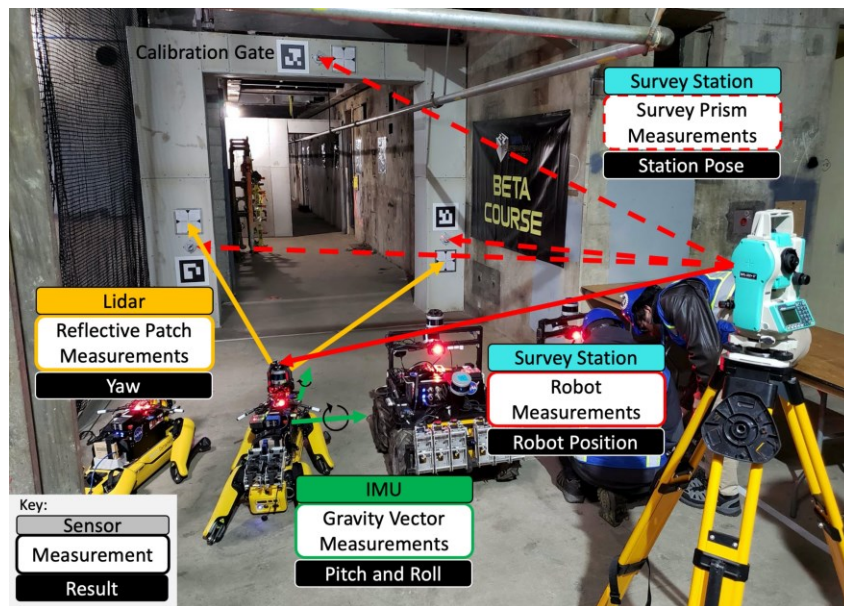
Figure 6-15: Example calibration to global frame from the DARPA Subterranean Challenge Urban Circuit. The coordinates of the survey prisms and reflective patches on the gate are provided and define the reference frame. A survey station measures the prisms to determine its pose in the global frame, after which it can measure the position of robots. LiDAR measurements of the reflective patches provide a yaw estimate and an IMU computes roll and pitch assuming gravity alignment of the reference frame.

loop closures, [56] for results using UWB beacons for a single robot and [59] for single robot cave exploration results.
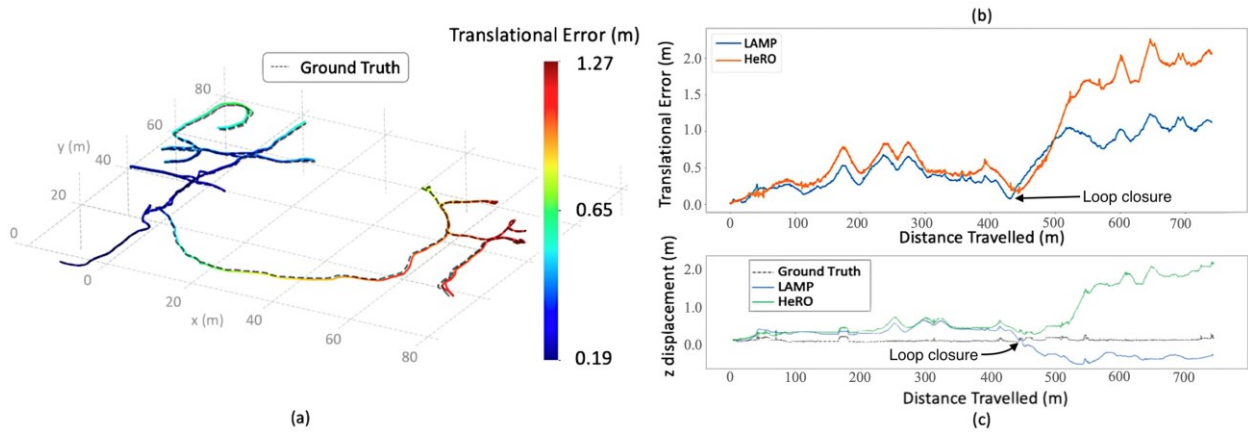
Figure 6-16: Single-robot LAMP performance with loop closures and IMU factors in the Urban Circuit of the DARPA Subterranean Challenge: (a) LAMP localization accuracy compared to DARPA-provided ground truth. (b) Translational error against distance travelled for LAMP, and the HeRO odometry input to LAMP. (c) z trajectory against distance travelled for LAMP, HeRO and the ground truth. IMU factors included in LAMP help to constrain attitude drift and achieved improved performance in z, and overall, compared to the input odometry.

6.7. Semantic Understanding and Artifact Detection

Semantic understanding of the environment and detecting objects of interest and artifacts are important capabilities to enable higher levels of robotic autonomy in unknown environments. Semantic mapping and artifact detection are among the main components of the NeBula autonomy framework. This section discusses NeBula's solution for detecting, localizing, and visualizing objects of interest on heterogeneous robots with different sensor configurations. Here, we focus on both (*i*) static objects, with clear visual, thermal, or depth signature, and (*ii*) spatially-diffused phenomena such as gas propagation and WiFi signal. The pipeline is explained in detail in [60], with a summary and recent extensions detailed here.
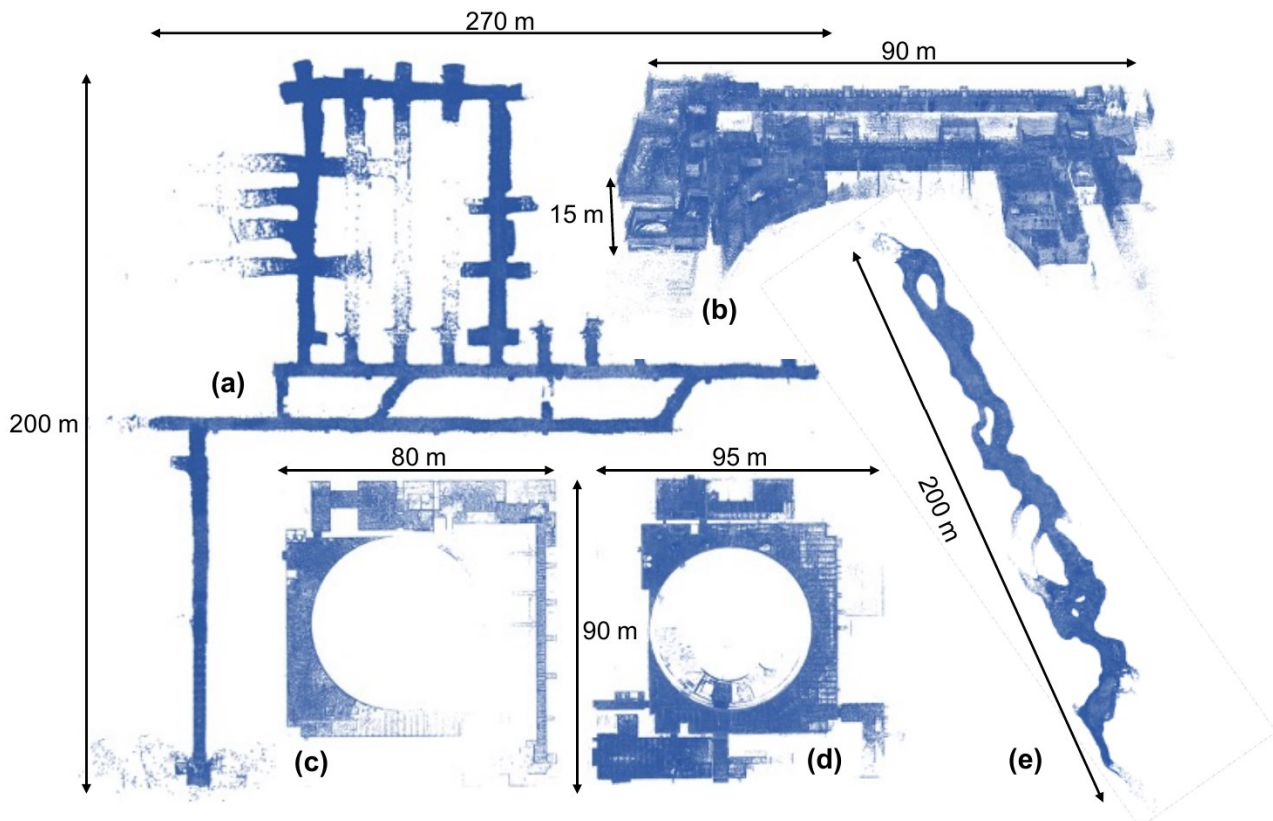
Figure 6-17: Maps from the five LAMP single-robot benchmark datasets. (a) Tunnel dataset from Bruceton mine on a Husky. (b) Multi-level urban dataset from Satsop Power Plant on a Spot robot. (c) and (d) Urban dataset from Satsop Power Plant on a Husky robot platform. (e) Cave dataset from Valentine Cave on a Spot robot. The ground truth is provided by DARPA for (a)-(d) and by survey scans for (e).

Requirements: The object detection system needs to (*i*) make detections in real-time across multiple sensor modalities; (*ii*) permit high-accuracy localization; (*iii*) adjust the sensor configuration based on the detection and localization confidence; and (*iv*) apply filtering to present the most likely detection candidates to the mission supervisor (when a communication link is established). While the method presented in this section is general, in the context of the DARPA Subterranean challenge, we focus on a set of predefined object types including gas sources (e.g., CO_2 source) and man-made objects such as fire extinguisher, drill, rope, helmet, survivor manikin, backpack, vent, and cell phone [61, 62]. Object signatures exist in one or more modalities: visual, thermal, depth, WiFi, audio, and chemical.

Architecture: Figure 6-19 shows the proposed object detection, localization, and visualization pipeline. We break down the underlying object detection problem into two stages: (1) an image-based object detection

Dataset	Robot	Environment	Dist. (km)	Max (m)	Mean (%)	Max (deg)	Mean (deg/m)
		Dataset Characteristics		Absolute Transl. Error		Absolute Rot. Error	
(a)	Husky	Tunnel	1.65	9.7	0.93%	5.3	0.006
(b)	Spot	Urban	0.65	2.2	0.46%	5.0	0.019
(c)	Husky	Urban	0.62	3.5	0.42%	3.9	0.011
(d)	Husky	Urban	0.75	0.9	0.19%	1.8	0.006
(e)	Spot	Cave	0.6	10.6	1.68%	6.0	0.020

Table 6-5: Performance statistics for LAMP operating on single-robot benchmark datasets from different robots and in different environments (Figure 6-17)
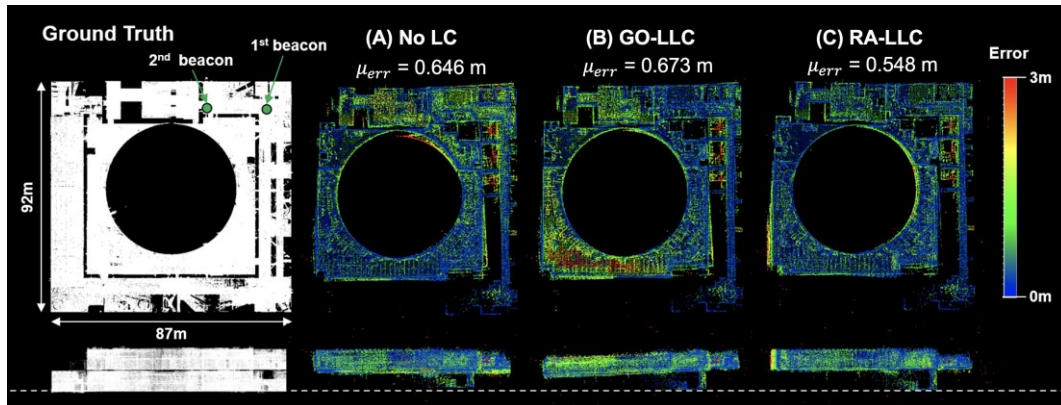
Figure 6-18: Multi-robot map accuracy results: (A) no loop closure (No LC); (B) geometric-only lidar loop closure (GO-LLC); and (C) range-aided lidar loop closure (RA-LLC). In this test, data from two robots in the Urban Circuit of the DARPA Subterranean Challenge are used, with two deployed UWB beacons (as shown on the left overlaid on the DARPA provided ground-truth map). μ_{error} indicates the mean map error to the ground truth map.

pipeline to first find the object; and (2) a relative localization filter applying projective geometry to the detection to estimate its position explicitly. By splitting the detection and localization tasks, we can utilize high quality and fast detection from existing algorithms and apply them to generic camera types in our relative localization approach. For temporally-static objects, NeBula relies on multi-modal detection and, when available on robots, leverages visual cameras, depth measurements, and thermal cameras.

Spatially Diffuse Phenomena: For temporally-dynamic and spatially-diffused phenomena, we rely on source seeking methods based on gas sensors and WiFi sensing. The detection confidence provides the uncertainty assessment to the perception-aware planner. The planner motivates the sensor to adjust the configuration to make new measurements with higher fidelity, leading to more accurate detections. We discuss the three stages of detection, localization, and base station processing in the rest of this section.

Detection: For visually-observable objects, detections are made in both the color and thermal spectra using state-of-the-art convolutional neural networks (CNNs). CNN produces a bounding box on the image to pass to the relative localization module. NeBula relies on different CNN implementations to adapt to various processing capabilities. On ground robots, a YOLO Tiny [63, 64] variant is used, leveraging GPU hardware (e.g., Nvidia Jetson Xavier) to run in real-time on multiple cameras (see Section 12). On drones, a MobileDet variant [65] is used, modified to run on a Google EdgeTPU. To achieve sufficient detection performance for our specific application, we fine-tuned the detection networks with the appropriate domainspecific dataset. In the context of SubT, we have produced more than 40,000 annotations of the following objects: fire extinguisher (12.26 %), drill (9.98%), rope (17.90%), helmet (19.29%), survivor (19.84%), and backpack (20.72%). Our training is focused on maximizing recall that increases true positives. This is followed by an outlier rejection method using range, color, and size filters, reducing the false positives. For more details on training methods on this data, see [60].

Localization: The detection networks produce 2D bounding boxes (within image) that are combined with depth measurements, used to compute the position of the artifact relative to the robot. The depth measurements can be obtained from multiple sources: depth cameras (such as from an RGB-D camera), LiDAR scans mapped into the camera frame, or a size-based projection, where the depth is computed such that the bounding box, when projected to 3D at that depth, matches the expected size of the object. These methods are detailed in [60]. For robustness to sensor failure, each method is run in parallel, with the highest priority method (LiDAR, then depth, then size projection) used if the corresponding sensor is available. All methods jointly filter multiple detections to produce a combined relative location reported to the LAMP module (Section 6) to compute the global location before sending the report to the base station. The relative location
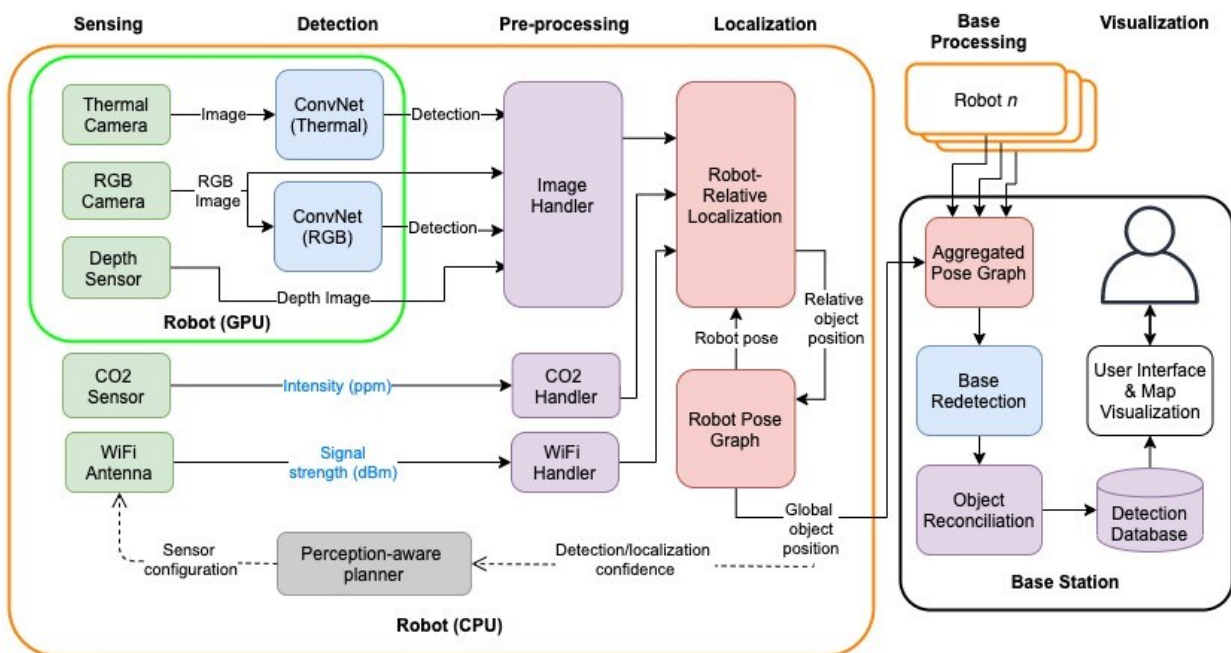

Figure 19: Multi-robot, multimodal object detection, localization and visualization pipeline.

can also be computed without depth measurements, as an additional back-up, and on systems without depth cameras or LiDAR (such as drones). In this case, we use a monocular based tracking approach over an image sequence (detailed in [66]).

Multi-modal multi-robot artifact reconciliation: The artifact reports from each of the robots are further processed on robots with more powerful computational resources (or on base station). These reports include:(*i*) detection class; (*ii*) detection confidence; (*iii*) reference RGB/thermal image; (*iv*) bounding box; and (*v*) location estimate. The base station processes the reports, rejecting outliers and matching observations of the same artifact instances from other agents or previous visits. To reduce the number of false positive reports, a larger and more performant detection network (YOLOv4 [64]) is used to update the detection confidence of each report. Then, the report is compared to previous reports of the same class to identify repeat observations and observations of the same artifact instance reported by other agents. This comparison uses both location proximity and a comparison of NetVLAD visual image descriptors [67]. The highest confidence report of each object is then saved to a database and visualized for review by the human supervisor using the mission executive interface (see Figure 6-20 - Visualization block). When needed, to increase the confidence on the detected semantics, the perception-aware motion planner seeks new measurements, e.g., from a closer or better angle to the target, or by sending a different robot with complementary sensors to get multiple readings from the target.

6.7.1.   Spatially Diffuse Localization

To detect and locate spatially diffuse phenomena, such as gas leaks and WiFi sources, the robotic team is leveraged as a mobile sensor network, with distributed and moving ambient sensor measurements. Signal strength (e.g. CO_2 concentration or WiFi RSSI) is recorded at every robot position and is (*i*) used to augment the global 3D semantic map (Figure 6-20-Detection block); and (*ii*) processed to produce an initial location estimate at the area of peak signal strength. The combination of the spatially informative semantic map with an initial location estimate seeds a local search for source locations, based on the 3D geometry. Automation of this local search is ongoing work. In tests presented here, information is sent to the base station for displaying to the operator, who performs the local search on inspection of the metric-semantic map.
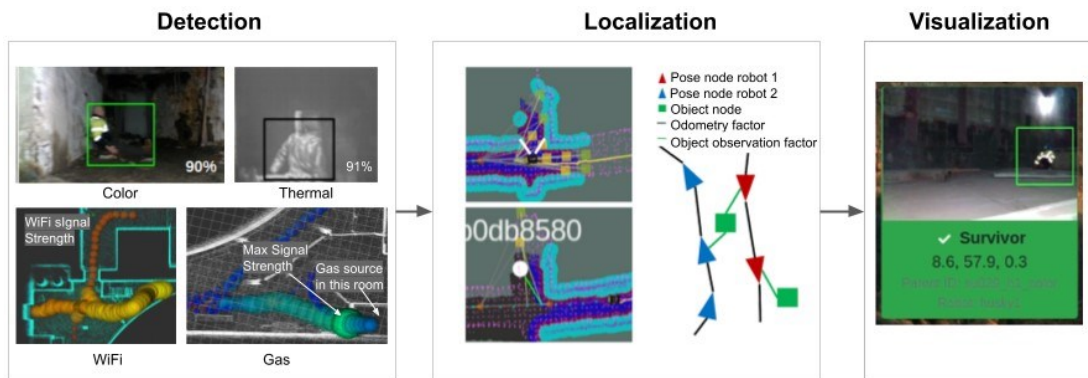
Figure 6-20: Visualization of representative parts of the object detection pipeline. In the left pane, a sample of detections for each of the four modalities (color, thermal, WiFi, and gas) is presented. In the middle pane, the addition of a natural landmark observation into the pose graph is depicted. The right pane shows the final operator view.

Detection performance: Figure 6-21 shows examples of a true and false positive detection for each visual artifact type. We observed that spray paint markings and existing equipment in the environments, which share the same gross features as the target objects, are incorrectly picked up. For spatially-diffuse detection (gas and WiFi), we extrapolate the source location by measuring the signal strength gradient and move the robot in directions that increase the detection confidence (see Figure 6-20-Detection block).

6.7.2. Experimental Evaluation

In order to evaluate our proposed framework, we perform high-fidelity simulation studies with a four-wheeled vehicle (Husky robot) and real-world experiments with a quadruped (Boston Dynamics Spot robot). Both robots are equipped with custom sensing and computing systems, enabling high levels of autonomy and communication capabilities [89]. The entire autonomy stack runs in real-time on an Intel Core i7 processor with 32 GB of RAM. The stack relies on a multi-sensor fusion framework. The core of this framework is 3D point cloud data provided by LiDAR range sensors mounted on the robots [50]. We refer to our autonomy stack-integrated Spot as Au-Spot [78].

Baseline Algorithms: We compare our PLGRIM framework against a local coverage planner baseline (next-best-view method) and a global coverage planner baseline (frontier-based method).

1. Next-Best-View (NBV): NBV is a widely-adopted local coverage planner that returns a path to the best next view point to move to. It uses an information gain-based reward function as ours but limits the policy search space to a set of shortest paths to sampled view points around the robot. While NBV is able to leverage local high-fidelity information, it suffers from spatially limited world belief and sparse policy space.

2. **Hierarchical Frontier-based Exploration (HFE)**: Frontier-based exploration is a prevalent global coverage planning approach that interleaves moving to a frontier node and creating new frontiers until there are no more frontiers left (e.g., [90]). While it optimizes for the global completeness of environment exploration but often suffers from the local suboptimality due to its large scale of the policy space and myopic one-step look-ahead decision making. The performance of frontier-based methods can be enhanced by modulating the spatial scope of frontier selection, but it still suffers from downsampling artifacts and a sparse policy space composed of large action steps.

6.7.2.1. Simulation Evaluation

We demonstrate PLGRIM's performance, as well as that of the baseline algorithms, in a simulated subway, maze, and cave environment. Figure 6-32 visualizes these environments. In our comparisons, in order to achieve reasonable performance with the baseline methods in complex simulated environments, we allow baseline methods to leverage our Local and Global IRM structures as the underlying search space.
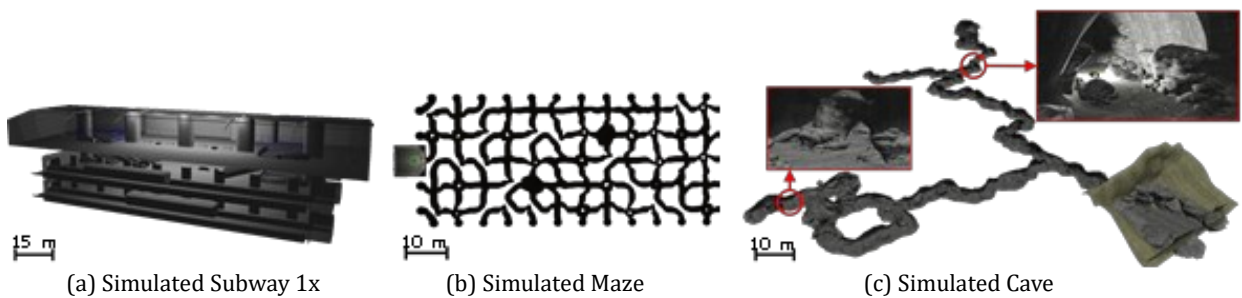

(a) Simulated Subway 1x   (b) Simulated Maze   (c) Simulated Cave

Figure 6-32: Simulated environments for performance validation: (a) subway station, (b) maze (top-down view), and (c) cave.
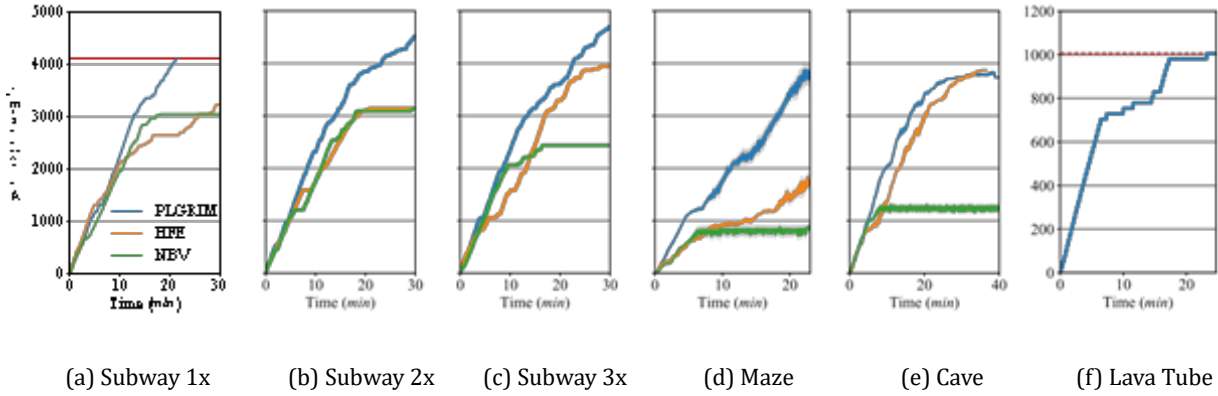
Figure 6-33: Exploration by PLGRIM and baseline methods in simulated subways of increasing size (a)-(c), simulated maze and cave (d)-(e), and real-world lava tube (f). For (d) and (e), the covered area is the average of two runs. Red dashed lines indicate 100% coverage of the environments, wherever applicable.

Simulated Subway Station: The subway station consists of large interconnected, polygonal rooms with smooth floors, devoid of obstacles. There are three varying sized subway environments, whose scales are denoted by 1x, 2x, and 3x. Figure 6-33(a)-(c) shows the scalable performance of PLGRIM against the baselines. In a relatively small environment without complex features (Subway 1x), NBV performance is competitive as it evaluates high-resolution paths based on information gain. However, as the environment scale grows, its myopic planning easily gets *stuck* and the robot's coverage rate drops significantly. HFE shows inconsistent performance in the subway environments. The accumulation of locally suboptimal decisions, due to its sparse environment representation, leads to the construction of a globally inefficient IRM structure. As a result, the robot must perform time-consuming detours in order to *pick up* leftover frontiers.

Simulated Maze and Cave: The maze and cave are both unstructured environments with complex terrain (rocks, steep slopes, etc.) and topology (narrow passages, sharp bends, dead-ends, open-spaces, etc.). The coverage rates for each algorithm are displayed in Figure 6-33(d)-(e). PLGRIM outperforms the baseline methods in these environments. By constructing long-horizon coverage paths over a high-resolution world belief representation, PLGRIM enables the robot to safely explore through hazardous terrain. Simultaneously, it maintains an understanding of the global world, which is leveraged when deciding where to explore next after exhausting all local information. In the cave, NBV's reliance on a deterministic path, without consideration of probabilistic risk, causes the robot to drive into a pile of rocks and become inoperable. NBV exhibits similarly poor performance in the maze. However, in this case, NBV's myopic planning is particularly ineffectual when faced with navigating a topologically-complex space, and the robot ultimately gets *stuck*. As was the case in the subway, HFE suffers in the topologically-complex maze due to the accumulation of suboptimal local decisions. In particular, frontiers are sometimes not detected in the sharp bends of the maze, leaving the robot with an empty local policy space. As a result, the robot cannot progress and spends considerable
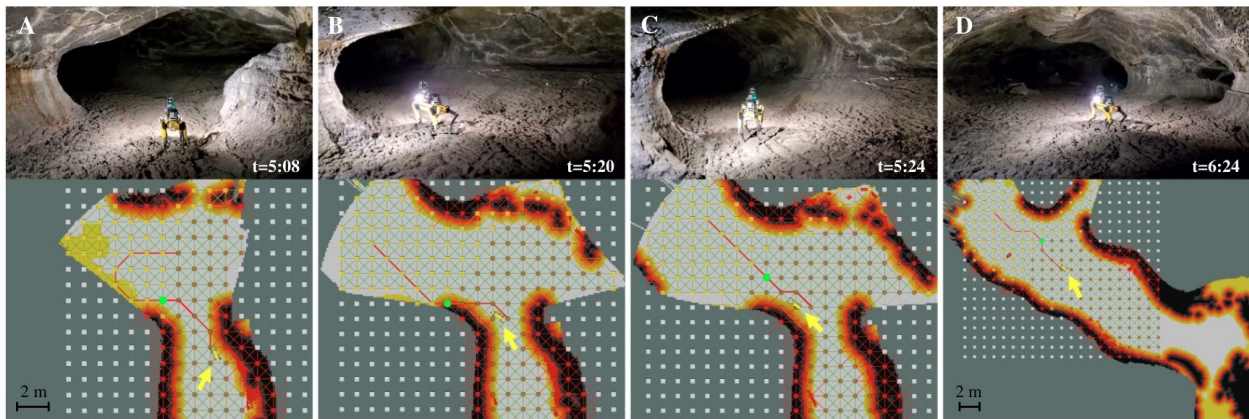
Figure 6-34: The Local IRM (yellow, brown, and white nodes represent uncovered, covered and unknown areas, respectively) is shown overlaid on the Riskmap. A yellow arrow indicates the robot's location. LCP plans a path (red) that fully covers the local area (snapshot A). When $p(\overset{.}{W})$ updates, the path is adjusted to extend towards the large uncovered swath while maintaining smoothness with the previous path. Another $p(\overset{.}{W})$ update reveals that the path has entered a hazardous area—wall of lava tube (snapshot B). As a demonstration of LCP's resiliency, the path shifts away from the hazardous area, and the robot is redirected towards the center of the tube (snapshot C). One minute later, the robot encounters a fork in the cave. The LCP path curves slightly toward fork apex (for maximal information gain) before entering the wider, less-risky channel (snapshot D).
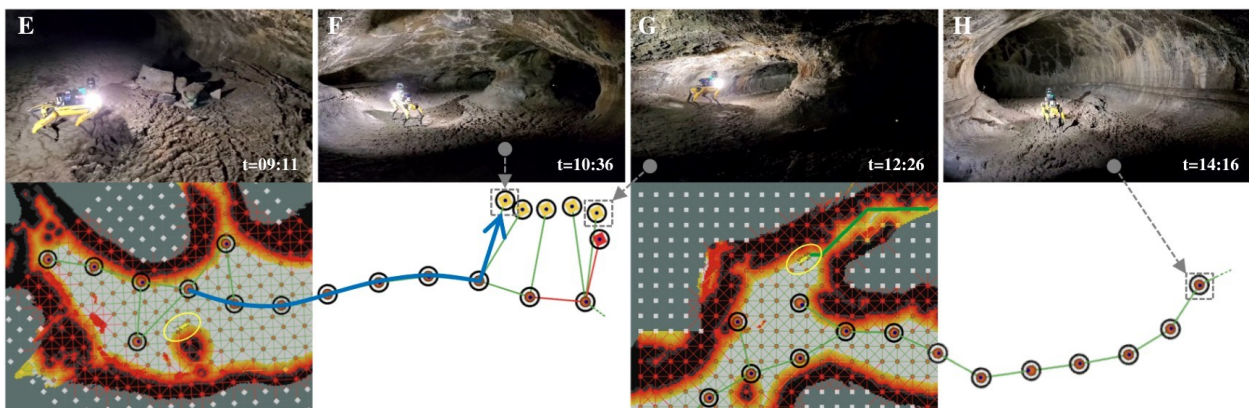
Figure 6-35: Portions of the Global IRM constructed in the lava tube are visualized–yellow nodes represent frontiers, brown nodes represent breadcrumbs. Gray arrows associate a frontier with a snapshot of the robot exploring that frontier. GCP plans a path (blue) along the Global IRM to a target frontier after the local area is fully covered (snapshot E). The robot explores the area around the frontier (snapshot F), and then explores a neighboring frontier at the opening of a narrow channel to its right. LCP plans a path (green) into the channel (snapshot G). Later, after all local areas have been explored, the robot is guided back towards the mouth of cave along the breadcrumb nodes (snapshot H). time backtracking along the IRM to distant frontiers.

6.7.2.2. Real-World Evaluation

We extensively validated PLGRIM on physical robots in real-world environments. In particular, PLGRIM was run on a quadruped robot Valentine lava tube, located in Lava Beds National Monument, Tulelake, CA. The cave consists of a main tube, which branches into smaller, auxiliary tubes. The floor is characterized by ropy masses of cooled lava. Large boulders, from ceiling breakdown, are scattered throughout the tube. Fig. 34 and 35 discuss how PLGRIM is able to overcome the challenges posed by large-scale environments with complex terrain and efficiently guide the robot's exploration. Fig. 33(f) shows the area covered over time.
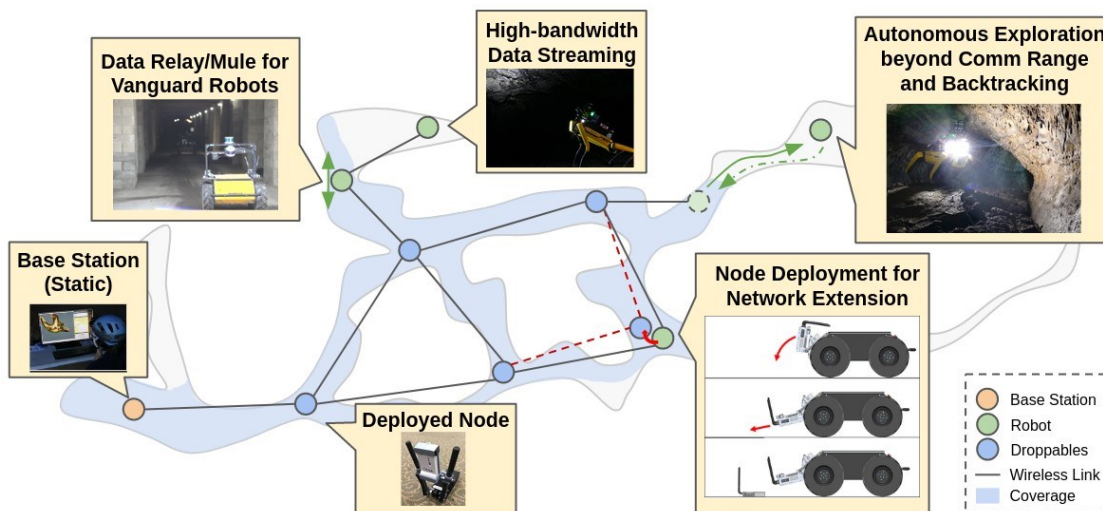
Figure 36: This figure shows how the mesh network is extended into the subterranean environment by deployed communication nodes which form a backbone network. Robots inside the coverage area of the backbone network can extend the network to robots in their communication range. Robots without a route through the network to the base station must be fully autonomous and return to an area with communication coverage to return data. Alternatively, (not pictured) multiple robots without a wireless route to the base station may share data and have one act as a data-mule to carry the data back to communication range.

6.8. Multi-Robot Networking

Multi-robot systems offer advanced capabilities to enable complex and time-constrained missions in largescale complex environments. Resilient wireless mesh networking solutions are a prerequisite for reliable and efficient multi-robot missions. NeBula is inherently a "networked" solution (Figure 6-7). While it can be implemented on a single autonomous robot, it also allows for faster and more efficient missions with multiple potentially heterogeneous robots (see Figure 6-5). NeBula's goal in the SubT challenge is to map an unknown subterranean environment, locate artifacts, and communicate that information to the base station via a wireless mesh network for submission to the DARPA Command Post. Inter-robot wireless communication in subterranean environments is particularly challenging and uncertain in the reliability, capacity, and availability of communication links because of: i) limited line-of-sight opportunities, ii) the complicated nature of the interaction of radio signals with the environment (e.g. reflecting, scattering, multipath), and iii) the unknown nature of the environment. In this section, we will go over NeBula's CHORD (Collaborative High-bandwidth Operations with Radio Droppables) communication system for comm-degraded subterranean environments. The objective of CHORD is to maintain high-bandwidth links to multiple robots for efficient commanding, autonomous operation, and data gathering in complex unknown environments. For more details on the development of NeBula's networking solutions, see [89, 91].

6.8.1. CHORD System Design

Architecture and ConOps: NeBula's operations in the SubT Challenge consists of three general types of agents: 1) static agents (e.g. base station), 2) mobile agents (e.g. robots), and 3) deployable static agents (e.g. communication relay nodes). Each agent communicates by means of a wireless mesh network using commercial off-the-shelf radios. We use a hybrid of ROS 1 and ROS 2 for the communication middleware [91, 92]. We use ROS 1 for intra-robot communications, and ROS 2 for inter-robot communications. The mesh network can be extended, as shown in Figure 6-36, into the subterranean environment by deploying communication nodes (Section 12.2) from robots to build a backbone wireless mesh network. The decision of where to drop communication nodes is based on the 3D map, data route, signal to noise ratio, and the estimated available bandwidth between each radio

[93]. The exact coverage area of each node is dependent on many factors including surface materials, roughness, and environment shape. Dropping communication nodes in range of another node with a route to the base station reduces the uncertainty of getting data back from robots near that node. Robots may also be used to extend the mesh network when they are in communication range of another asset (robot or communication node) with a route to the base station. When a robot needs to send data to the base station, but has no communication route to the base station, it can either return to the communication range of an asset that does have a route to the base station (usually be backtracking to a node on the backbone network) or communicate that data to another robot (referred to as a data mule) which is returning.

Intra-robot Communication: Each robot consists of a combination of computers and sensors (see Section 12) connected by Gigabit Ethernet. Where possible (current generation Husky hardware) this network is separate from the radio network and connects only through a single computer which is connected to a radio. That computer runs the ROS 1 core, the ROS 1-2 bridge, and is responsible for handling inter-agent communication. This further isolates intra-robot communication from inter-agent communication and prevents inadvertent radio traffic. Intra-robot communications are monitored using ROS 1 topic statistics.

Inter-agent Communication: Even with relatively high power/bandwidth radios, bandwidth is still a shared, limited, and temporary resource. Efforts must be taken to manage bandwidth usage and be robust to communication loss when robots operate outside the range of the radios. CHORD uses ROS 2 over the wireless mesh network for inter-agent communication. The advanced Quality of Service (QoS) features of ROS 2 are used to guarantee delivery of important priority data while maintaining network stability over low-bandwidth links. This configuration enables traffic prioritization and resource control. We configured two categories of QoS for inter-robot topics with different mission requirements. Topics that require full message history transfer for post-processing or that deliver mission-critical information have higher priority and are configured so that the messages are reliably delivered even though the network may be down for periods of time. Estimated link capacities, data routes, and data traffic are also monitored to ensure stability.

6.8.2. Evolution of CHORD

Tunnel Circuit: During the Tunnel competition we used ROS 1 in combination with a custom cross-master messaging mechanism (multimaster-JPL) in combination with radios from Silvus Technologies and Persistent Systems [89]. While our communication system and radios supported our six robot operation well during the tunnel competition, we observed some communication issues. We found that careful attention was needed to avoid ROS 1 attempting to share global topics (like TFs and diagnostics) across all robots. In addition, without better quality of service (QoS) controls, robots outside of the communication range of the backbone network would buffer all data and flood the network on their return. Some of our data products were also larger than expected. See [89] for more details.

Urban Circuit: Before the Urban competition we switched to using ROS 2 for inter-agent communication in combination with radios from Silvus Technologies. We observed better performance than our previous ROS 1-only data sharing system. First, by using a different protocol for inter-robot communication, we isolated the ROS 1 networks completely and avoided unintended data flows between agents. The network isolation also helped to diagnose network issues easily as every inter-robot ROS topic passes through the bridge node. Second, we were able to keep network traffic inside our bandwidth budget, which contributed to the stability of the dynamic network. For more details on the results, see [91].

6.9. Mobility Systems and Hardware Integration

As described in Section 3, to simultaneously address various challenges associated with exploring unknown challenging terrains, we rely on a team of heterogeneous robots with complementary capabilities in mobility, sensing, computing, and endurance. These assets are deployed in the mission as the robots learn about the terrain specifications. Figure 6-40 shows four classes of our robots: (i) Wheeled rovers: to cover general and relatively smooth surfaces and mild obstacles. (ii) Legged robots: to cover more challenging and uneven terrains where surmounting obstacles or staircases are required [78, 18, 98, 99]. (iii) Tracked robots: To complement legged platforms in handling different surface material, and (iv) Aerial and Hybrid locomotion: to enable traversing vertical shafts, and areas that are not accessible by ground robots.

6.9.1. Ground robots

Our ground robots are able to carry heavy payloads. Hence they are equipped with high levels of sensory and processing capabilities enabling complex autonomous behaviors and artifact detection. Their battery capacity allows them to have longer operational time than flying vehicles. Below, we discuss the NeBula Autonomy Payload on these ground robots.

Architecture: The NeBula payload (Figure 6-41) consists of the NeBula Sensor Package (NSP), NeBula Power and Computing Core (NPCC), NeBula Diagnostics Board (NDB), and NeBula Communications Deployment System (NCDS). Its electronics and software architecture is modular, to facilitate adaptation to varying mechanical and power constraints of each platform in our heterogeneous robotic fleet.

Design Principles: The key design principles are:

- Durability: Shock proofing of the system increases longevity and self-recovery chances when exploring challenging terrains.
- Lightweight materials: Payload reduction maximizes robot agility and battery life.

Topology	Wheeled Vehicles Husky	Legged Platform Spot	Hybrid Vehicles Rollercopter, Drivocopter
High-level Computers	**SLAM:** Multiple, High-power CPU **Object Recognition:** NVIDIA GPU	**SLAM:** Mid-power CPU **Object Recognition:** NVIDIA GPU	**SLAM:** Lightweight SB-CPU's **Object Recognition:** NVIDIA GPU
Low Level Microcontrollers	**Safety features:** Atmel MCU **Comm Dropper:** STM MCU	**Safety features:** Atmel MCU **Comm Dropper:** STM MCU	**Safety features:** Atmel MCU
Sensors	LiDAR, depth and thermal cameras, gas and signal sensors, external IMU.	LiDAR, depth and thermal cameras, gas and signal sensors, external IMU.	LiDAR, depth and color cameras, IMU.
Comm Dropper	Yes	Yes	No
Mass	50kg	40kg	1-5kg
Battery	Lead acid	Lithium ion	Lithium polymer
Operational time	3 hours	1.5 hours	<60 minutes
Topology	High-speed Data Mules Balto	Tracked Vehicles Telemax	Aerial Vehicles Quadrotor, Coax-octocopter
High-level Computers	**SLAM:** Single mid-power CPU **Object Recognition:** NVIDIA GPU	**SLAM:** Single high-power CPU **Object Recognition:** NVIDIA GPU	**SLAM and object detection:** Lightweight low-power CPU
Low Level Microcontrollers	**Safety features:** Atmel MCU	**Safety features:** Atmel MCU **Comm Dropper:** STM MCU	**Safety features:** Atmel MCU
Sensors	LiDAR, depth and thermal cameras, gas and signal sensors, external IMU.	LiDAR, depth and thermal cameras, gas and signal sensors, external IMU.	Depth and color cameras, IMU, 2D lidars
Comm Dropper	No	Yes	No
Mass	10kg	75kg	0.5-3kg
Battery	Lithium Polymer	Lead acid	Lithium Polymer
Operational time	2 hours	3 hours	<20 minutes

Figure 6-40: Hardware specifications for some of CoSTAR robots
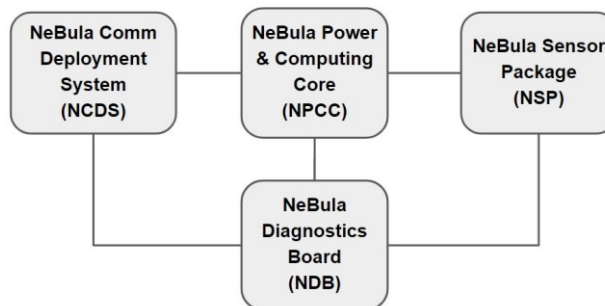
Figure 6-41: High-level overview of the 'NeBula Autonomy Payload' architecture

- Modularity: A critical feature when developing a heterogeneous fleet of robots with various capabilities. For example, processors and sensors are adaptable across different mobility systems with differing mass/size constraints.
- Portability: Ease of transportation, minimize damage to valuable hardware.

- HW-autonomy co-design: Adaptable design process to enable reconfiguring sensors to adapt to autonomy evolution.

NeBula Sensor Package (NSP): The NSP empowers the NeBula autonomy solution on the robots by gathering sensory information in real-time from the environment. NSP is heterogeneous: on each robot NSP consists of a subset of the following sensors: LiDARs, monocular, stereo, and thermal cameras, external IMU's, encoders, contact sensors, ultra high lumen LEDs, radars, gas sensors, UWB and wireless signal detectors. NSP is protected by custom superstructures with impact protection. A combination of hard resin urethane, semi rigid carbon-infused nylon, and aluminum were used. The NSP interfaces with the NPCC via high-bandwidth USB and Ethernet for data and custom serial messages and push-pull connectors for high-amp power. One version is depicted in Figure 6-42, which shows NSP payloads utilizing an array of Velodyne Puck VLP-16, Intel Realsense d435i, and FLIR Boson 640, among several others; the sensors are interchangeable and reconfigurable to accommodate different sensor arrangements, manufacturers and sensing modalities.

Figure 6-42: NSP equipped on Husky (left) and Spot (right).

NeBula Power and Computing Core (NPCC): The NPCC is an auxiliary payload which provides power to all NeBula sensors and computers used for autonomy. Aluminum enclosures provide protection to the internal electronics in the event of atypical loads and impacts such as falls and collisions. It is designed with considerations for thermal cooling and haptics due to extensive cycling of the connector interface panel. The modular, auxiliary-mount design was tweaked to accommodate for the reduced flight-weight of the drones. NPCC is powered from an external lithium high capacity battery to provide isolation and extended battery life for the internal battery across the heterogeneous fleet. The payload uses two high-power computers for sensing, autonomy, and semantic scene understanding and also hosts the low-level microprocessor. On some robots, NPCC is equipped with a GPU-based system-on-module with a custom interface to the power modules, cameras and sensors to accommodate machine learning and semantic understanding functionalities. The various configurations of the NPCC can be seen in Figure 6-43.

NeBula Diagnostics Board (NDB): The NDB implements the system diagnostics, which monitors the vital power elements of the robot such as battery voltage, input current and individual regulator voltages. When the robot boots initially, all voltage regulators are powered up in a staggered sequence to limit the inrush loads to the NDB. After each voltage regulator is enabled, the processor checks that the voltage is within the expected range and reports errors if any are found. In addition, the current monitoring checks for high current draw when each of the regulators are enabled to detect possible short circuits in the various robot sensors and mechanisms. The power module has an input protection circuit to protect against voltage
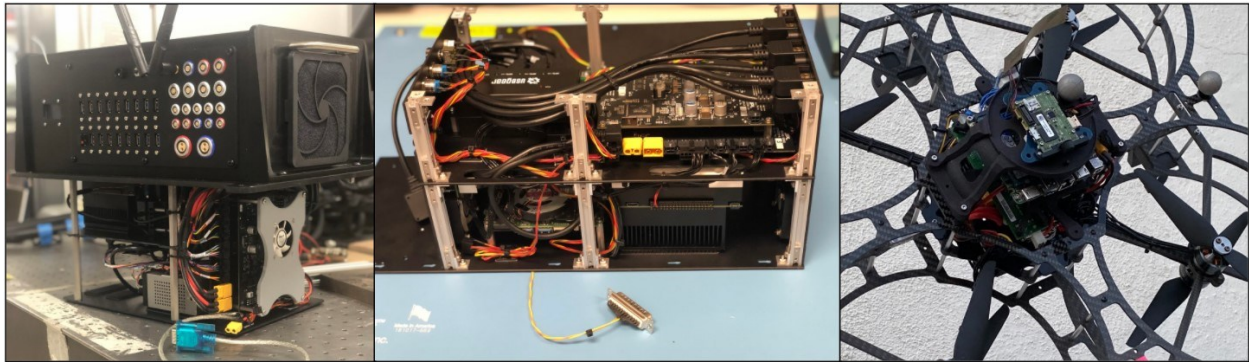
Figure 6-43: NeBula Power and Computing Core. Wheeled/tracked vehicles (left), Legged (middle), Aerial (right).

transients, reverse polarity and under voltage. A custom ROS message combines all these measurements and is constantly publishing the hardware power status to a specific robot diagnostic topic using the rosserial interface.

Figure 6-44: NCDS equipped on Husky (left) and Spot (right).

NeBula Comm Deployment System (NCDS): As discussed in our ConOps in Section 3, we construct and expand a wireless mesh network near the environment entrance, to extend the reach of the base station. In order to do so, ground robots are equipped with a Comm Deployment System (NCDS), which allow them to carry and deploy communication radios (comm nodes) and static assets during the mission. The radios are autonomously deployed using the NCDS which mounts at the rear of the robots seen in Figure 6-44. The comm nodes are encased in aluminum until release, and the NCDS electronics are mounted locally on the mechanism and sealed for ingress protection. The core protection and brake-lock/release mechanism was modularized across the fleet though the deployment capacity was reduced for the legged and tracked vehicles due to available mounting points, payload constraints and sensor occlusion. It is driven by a geared brushless motor and activated via a custom embedded system communicating over rosserial. A ROS message provides the status of each radio (loaded, dropped). The NCDS circuit board interfaces with the NPCC via serial communication. It monitors the hard stop switches used for calibration and the switches responsible for detecting if radios are loaded/released. A high level representation is depicted in Figure 6-45.

The NCDS software architecture relies on a finite state machine (FSM), with the following representative activities:

- Start up: Checks for battery power. Enables motor power and establishes links with motors.
- Calibration: Servos is actuated until limit switches are contacted. Encoder positional values are then stored in local memory.

  _____

- Load/Unload: Manual switches allows the user to load and swap radios.
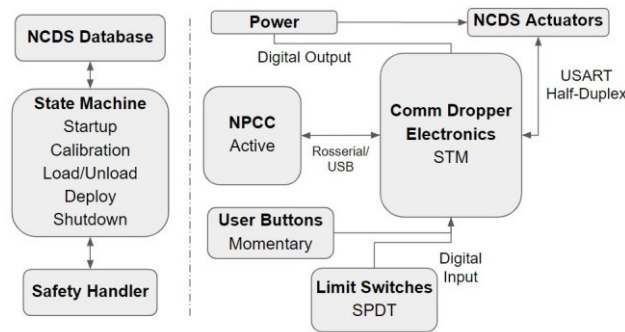
Figure 6-45: NCDS Software Architecture (left) and NCDS Hardware Architecture (right)

- Deploy Radio: Perform radio deployment. Use sensors to detect if deployment was successful.
- Shutdown: Disables motor power.

6.9.2. Static assets

Static assets refer to hardware solutions which are not capable of changing their position after deployment. Our static assets are composed of: comm nodes and UWB modules as pictured in Figure 6-46. The comm nodes construct NeBula's mesh network to enable more efficient inter-robot information exchange, while the UWB provide auxiliary landmarks and provides ranging measurement to assist the SLAM and global localization modules, as explained in Section 6. Static nodes can be powered prior to the start of a mission or prior deployment. They are carried by mobile robots and deployed by the NeBula Comm Deployment System (NCDS).

Figure 6-46: Static asset (comm node and UWB)

6.9.3. Flying vehicles

NeBula has been implemented on several flying robots of varying sizes. Flying robots are responsible for exploring vertical shafts, areas not accessible with ground robots, or relaying data from the ground robots to the base station by quickly flying to regions with strong communication connectivity, e.g., for data muling (see Section 10). Their processors and sensing capability is much more constrained than our ground robots. The concept behind the drone development is to keep a balance between the payload, the size of the drone, and the endurance. Thus, an iterative design has been performed in order to conclude in an optimal hardware configuration [100]. Figure 6-47 shows several NeBula-powered aerial vehicles:

A specific example is shown in Figure 6-48, a custom drone extensively utilized in this project that carefully
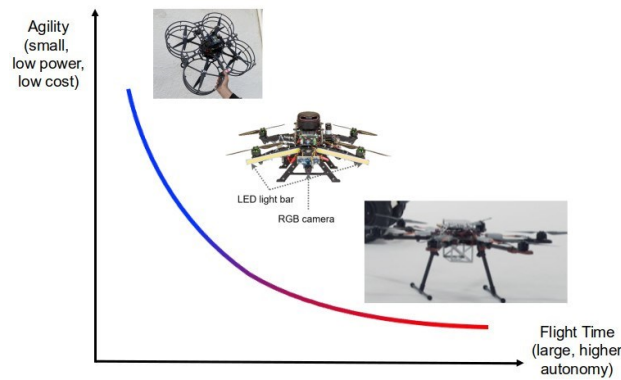
Figure 6-47: Flight time of similarly-sized vehicles with different autonomy capabilities. The general trend for aerial robots is long flight times are possible at the expense of large vehicles with less access and agility.

balances speed, weight, autonomy capability, and flight time. The vehicle's weight is 1.5 kg and provides 12 minutes of flight time. A 2D rotating RPLiDAR A2 is mounted on top of the vehicle, providing range measurements at 10 Hz and a monocular visual sensor at 30 FPS. The velocity estimation is based on the PX4Flow optical flow sensor at 20 Hz, while the height measurements are provided by the single beam LiDAR-lite v3 at 100 Hz, both installed on the bottom of the vehicle pointing down as indicated in Figure 6-48. Furthermore, the aerial platform is equipped with two 10 W LED light bars in both front arms for providing additional illumination for the forward looking camera and four low-power LEDs pointing down for providing additional illumination for the optical flow sensor.
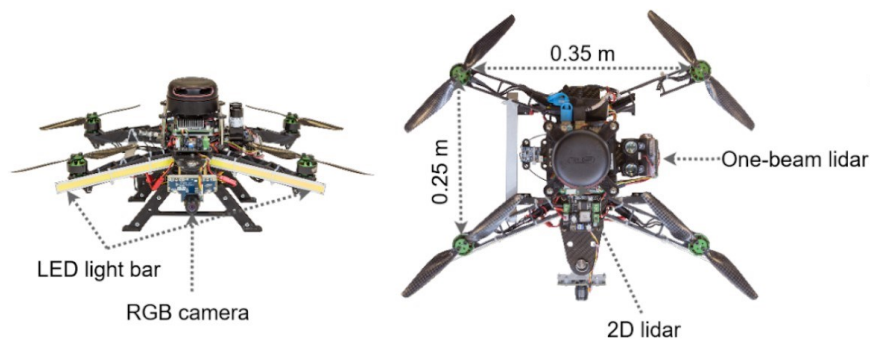
Figure 6-48: Drone equipped with a forward looking camera, a LED light bars, optical flow, 2D LiDAR and single beam LiDAR looking upward and downward.

6.9.4. Hybrid

To extend the range of the flying drones, our team has been investigating and designing new hybrid ground/aerial vehicles, referred to as "rollocopters". Rollocopters are designed to mainly roll on the ground; and when rolling is not possible, they can fly, negotiate a non-rollable terrain element, and land on the other side, and continue rolling. The combined rolling/flying behavior can extend the operational lifetime by several folds. Furthermore, the structure used for rolling the robot is designed to provide impact resilience while flying which provides further robustness. Our hybrid platforms consist of an adapted version of the above-mentioned NeBula payload along with the pixhawk firmware [101]. [102] describes the details of integration of the NeBula autonomy stack on the rollocopter platform.

Design Evolution: Figure 6-50 shows different variations of the rollocopter platform. The Hytaq version [103] consists of a rotating cage, which encloses the drone to enable rolling. Figure 6-49 shows a time-lapse for early hybrid mobility tests on reinforced versions of this platform at JPL's Mars Yard [104]. Its modular, multi-agent version, called Shapeshifter [105, 106], self-assembles this shell using

permanent electromagnets. Passive-wheeled-rollocopter (PW-rollocopter) [102, 29] uses two independent passive wheels to enable large sensory FOV and autonomy. To reduce propeller-generated dust, Drivocopter [107] and BAXTER [108] implement dedicated wheeled actuators, at the expense of a slight reduction in flight time. The latest work is focused on omnidirectional spherical rollocopters that provide maximum agility and maneuverability while having the minimum friction [109, 110].

Figure 49: Hybrid platform flying over an obstacle at the JPL Mars Yard [104].

Figure 6-50: Hybrid platform hardware evolution (top row: left to right) pre-challenge Hytaq design [103], Modular hybrid vehicle [105], (bottom row: left to right) Autonomous Rollocopter [102, 29], DrivoCopter [107], BAXTER [108], Spherical Rollocopter [109, 110].

6.10. Experiments

In this section, we present Team CoSTAR's multi-year effort to validate NeBula technologies on physical and virtual systems. We first briefly discuss our simulation-based validation approach, and then discuss the performance of NeBula on heterogeneous physical robot teams in various challenging real-world environments. The videos in [17, 18, 19, 20, 21] depicts some highlights of these runs.

6.10.1. Simulation Results

Simulator Configuration: We use simulations both for component development and integration testing. NeBula relies on multiple simulator configurations at different fidelity levels to enable faster and more focused development. Examples include a high-fidelity Gazebo simulator for testing ground vehicle behaviors, flight stack software-in-the-loop simulations for analyzing flight performance, a docker-based multi-robot
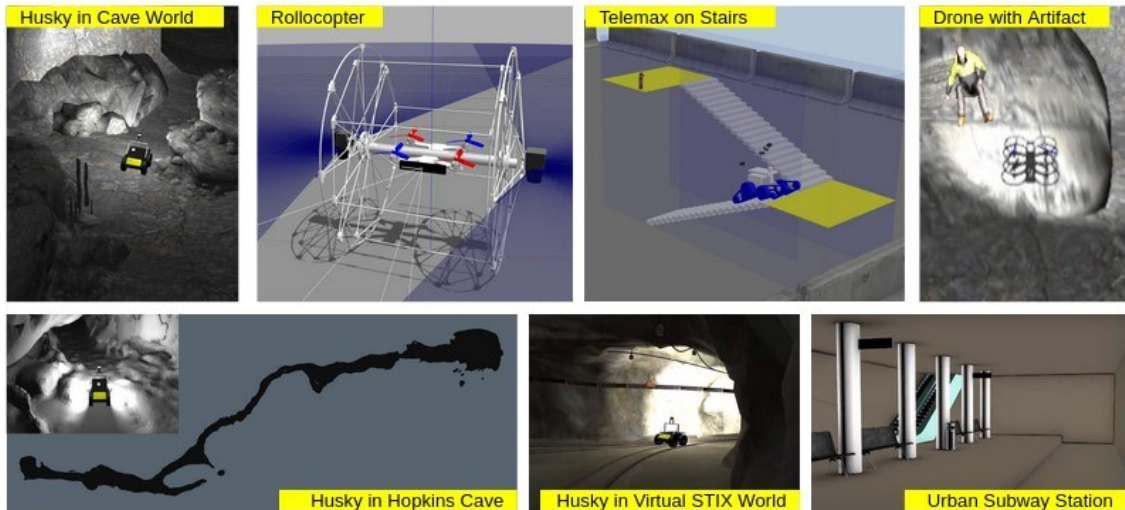
Figure 6-51: Robot and environment simulation models

networking simulator, and a low-fidelity dynamics simulator for Monte-Carlo analysis. Our simulator setup is portable, and used in local and cloud environments depending on the computational resources it requires and the number of agents that are deployed during the test.

Robot and Environment Models: Figure 6-51 shows selected examples of our simulated robot and environment models. In addition to many existing open-source models including the ones available at SubT Tech Repo [111], we build our custom robot and environment models, some of which are submitted to and available on the same repository. For example, Figure 6-52 shows a comparative study of drone navigation algorithms using the robot and environment models that are publicly available on the repository.

Self-organized Simulation Events: We regularly organize simulation-based events ("virtual" demos emulating the virtual DARPA SubT Challenge, see [112]) to track performance statistics over time. In each virtual demo, we evaluate the latest system performance based on several evaluation metrics. We developed a set of automated analysis tools to evaluate statistics on exploration, localization, mapping, artifact scoring, and human intervention. Simulation enables us to measure the statistics from large-scale tests which cannot be obtained easily with hardware experiments. Figure 6-53 shows exploration and operation statistics of a single robot simulation in the Gazebo simulator. The competition statistics (Figure 6-53-a) provide high-level evaluation with the number of sectors covered, number of artifacts scored, and robot trajectories in the course. The exploration statistics (Figure 6-53-b,c) evaluate how quickly and efficiently the autonomous exploration behavior covered the large-scale environment. The human supervisor intervention is monitored to measure the reliability of the autonomous system (Figure 6-53-b). The localization and mapping performance (Figure 6-53-b,d) is evaluated against the ground-truth dataset generated from the simulator. Finally, the artifact scoring performance is quantified with detection and localization evaluation (Figure 6-53-b).

6.10.2. Field Tests and Demonstrations

Our system has been rigorously field-tested in over 100 field tests in 17 different off-site locations, from lava tubes to mines 240m underground as well as numerous on-site locations including JPL's Mars Yard. This testing regime is a fundamental part of field-hardening our system to perform robustly in real-world challenging environments. A snapshot of some of our field test locations is shown in Figure 6-54. In this section, we discuss highlights of our system's performance at these self-organized field tests and demonstrations.

Extreme terrain in a natural lava tube

Sweden
South Korea

Eagle Rock Substation Building

240 m underground in Arch Mine, WV

Figure 6-54: Locations and snapshots from field test activities. Each blue circle is a different field-test location. DARPA Organized Events

This section outlines results from testing NeBula in the series of DARPA facilitated test events as part of the Subterranean Challenge [62]. The timeline of these events is summarized in Figure 6-60, with substantial developments over each of the 6 months intervals between tests by all teams, including (but not limited to) [114, 115, 116, 117, 118, 119, 120].

6.10.2.1. SubT Integration Exercise (STIX)

Environment and Robots: STIX was held in April 2019 at the Edgar Experimental Mine, Idaho Springs, CO. The participating teams were offered two practice sessions and one simulated scored run in an environment representative of the Tunnel Circuit. For Team CoSTAR, one of the primary objectives was to quantify the capability and limitation of various mobility systems through the evaluation in a real mine environment. To that end, we deployed four different types of mobility platforms shown in Figure 6-61, including Clearpath
Husky wheeled vehicle, Flipper tracked vehicle, Scout quadcopter, and Rollocopter aerial/ground hybrid vehicle.

Performance: Each platform demonstrated autonomous exploration capabilities in the mine. Husky autonomously traversed 200 m until it reached the first fork. During the drive, Husky detected 5 artifacts and reported back to the base station: two of which were correct in types and locations. Soon after Husky turned into a side passage, the communication to the base station was lost, which triggered the return to base behavior as designed. The robot successfully returned to the base by following the breadcrumb nodes in IRM. Rollocopter performed four 3-minute runs during the practice sessions, each of which consisted of au-
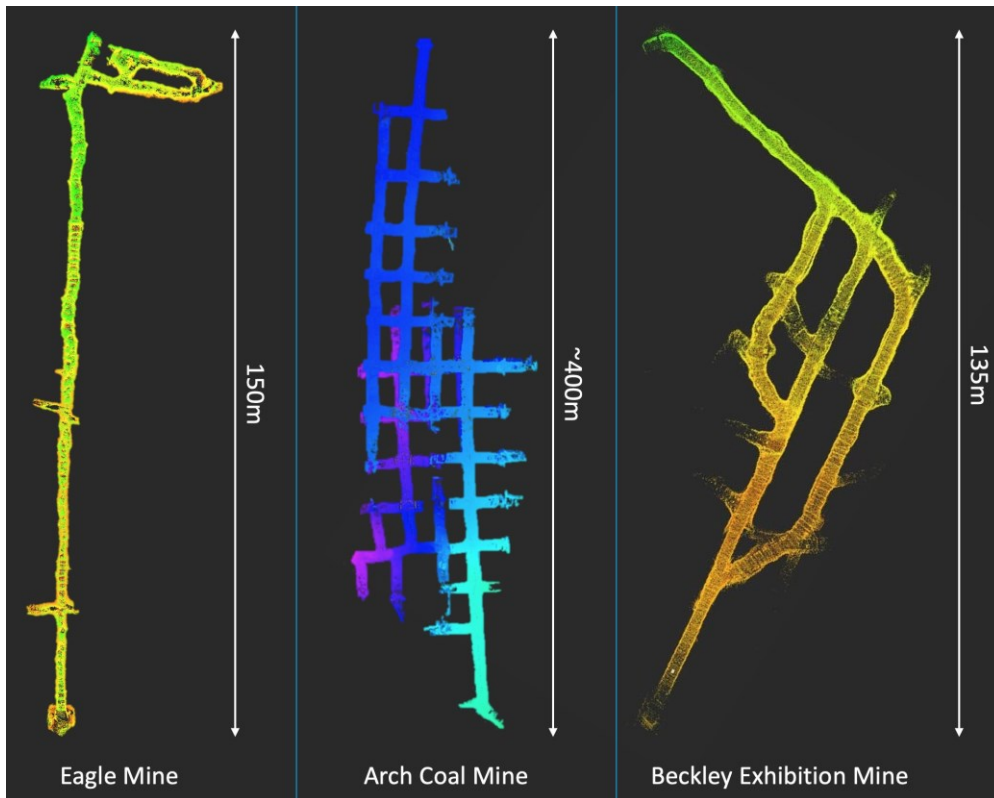
Figure 6-55: SLAM point cloud maps from field tests in different mine locations. Left: a silver mine in southern California. Center: a portion of a large coal mine in West Virginia, 800ft underground. Right: A near-surface historic coal mine in West Virginia.

Figure 6-56: Autonomous flights in Mj¨olkuddsberget Mine, Sweden (left) and Hwasoon Mine, Korea (right).

tonomous take-off, exploration, and landing operations. The robot exhibited robust navigation capabilities, traveling over 100m in cumulative distance. Dust was a major issue for drone flight in the narrow passageways, causing vision-based state estimation failures. Our approach of using heterogenous odometry sources enabled us to be resilient to these failures to a large degree [23]. Dust largely obscured all cameras after a few minutes into each run. With no measurement updates from odometry sources, we relied on IMU-only inertial odometry to safely land the vehicle. These results led to future work on improving state estimation resilience in the presence of dust and variable lighting. It also helped us to improve the camera placement design for the various scales of environments. The Flipper was able to navigate over the train tracks in the tunnel because of its tracked design but it was much slower than the Husky. This is because of greater contact area of the tracks that causes slower turning behavior compared to differential drive (wheeled) robots for the same commanded track/wheel speeds [121]. This is why we decided to incorporate a hybrid vehicle that had both wheels and tracks (Telemax) in the next circuit. We extensively tested Telemax in the Arch
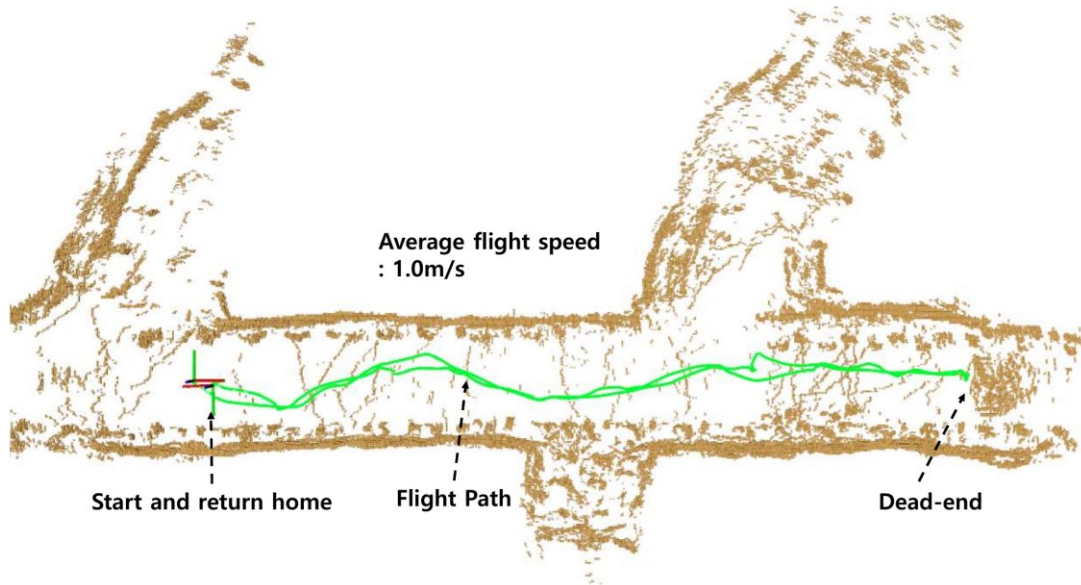
Figure 6-57: Autonomous flight test at Beckley Mine, Morgan Town, WV. In this example, the drone flies approximately 50m over 45s. While flying, the drone meets the dead-end and return to the communication range to deliver the map and artifact data before explore other branches of the mine.
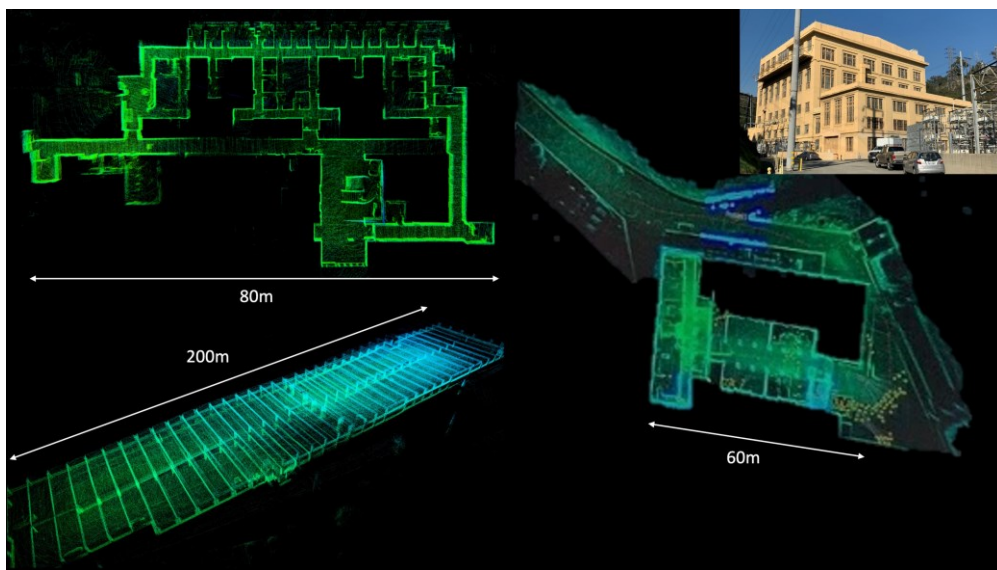
Figure 6-58: SLAM point cloud maps from field tests in different locations. Top Left: an office building at JPL. Bottom Left: A multi-level parking structure at JPL. Right: Eagle Rock substation and surrounds

(pictured at top right)

mine [68] and were able to navigate over different types of terrain (in tracked mode) while maintaining speed when the robot was on flat terrain (in wheel mode).
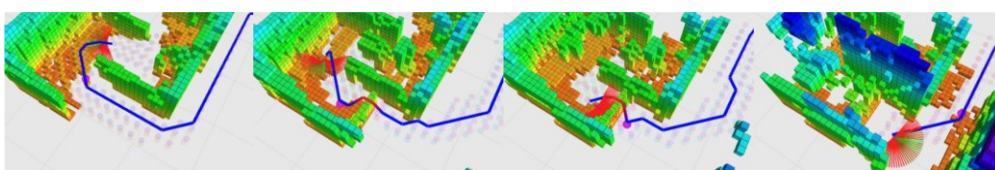
(a)   Time sequence of planned hybrid transition from rolling to flying and back to rolling. Colored blocks are occupiedvoxels colored by z height. Blue/Red path indicates hybrid

planned path where blue is rolling and red is flying. Pink sphere is goal waypoint. Motion primitives from local planner are shown. Note that as the vehicle moves forward, an obstacle is revealed and a small hop over it is planned and executed.

(b) Power-energy consumption comparison with hybrid (green), rolling-only (blue), and flying-only (red) mobilitymodes. The hybrid mode flies over three obstacles, while rolling-only mode was tested without any obstacles.
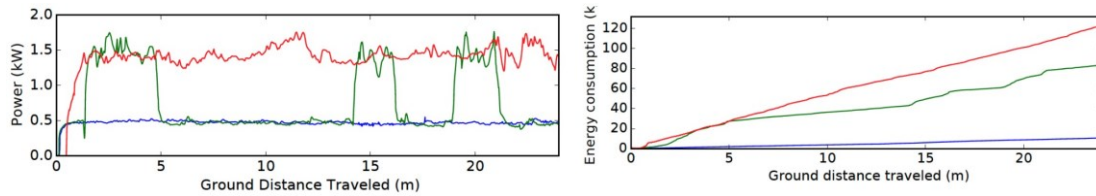
Figure 6-59: Rollocopter mobility mode comparison
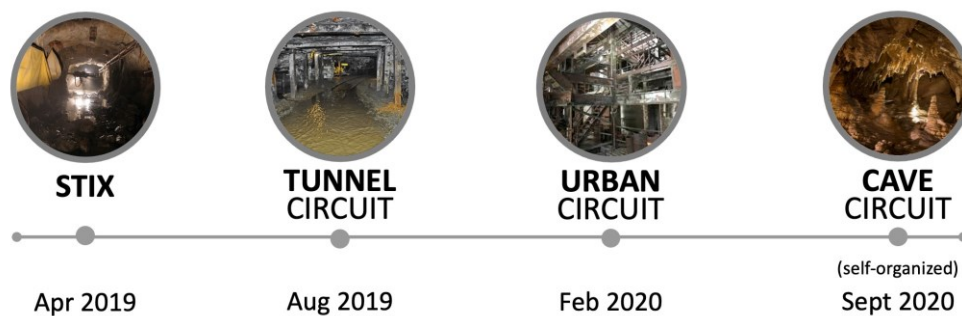
Figure 6-60: Overview of the timeline of DARPA organized test activities, with the expectation of increasing capability from one event to the next.

6.10.2.2. Tunnel Circuit

Environment: The Tunnel Circuit took place in August 2019 at the NIOSH mine complexes in Pittsburgh, PA. There were two courses, Experimental (EX) and Safety Research (SR), focusing on different aspects of the tunnel environmental challenges. The EX course is composed of long straight corridors with featureless flat walls. The SR course has a grid-like structure that provides many decision points and loop closures.

Robots: Team CoSTAR staged seven robots at the starting gate (see Figure 6-62). The robot roster includes four Clearpath Husky robots (Husky 1-4), one Telerob Telemax track/wheel hybrid robot (Telemax 1), one high-speed RC car (Xmaxx 1), and one aerial drone (Scout 1). Our strategy was to adaptively deploy the heterogeneous robot team based on the complexity and challenges of the unseen course elements. The information from vanguard robots told that the environment is benign and mostly accessible by the ground vehicles, leading the decision to rely more on wheeled platforms that show higher endurance.

Performance: In each run, we sent 3 to 4 robots to the course and achieved more than 2 km combined traversal (Figure 6-63). The video in [17] depicts some highlights of these runs. The longest single-robot drive was 1.26 km by Husky 4 at the SR mine on Day 3, including long periods of no-communication autonomous exploration and successful returning to the communication range at the end of the mission. Figure 6-64 shows the map created by Husky 4 in this run, with an error under 1% of the distance travelled. Four
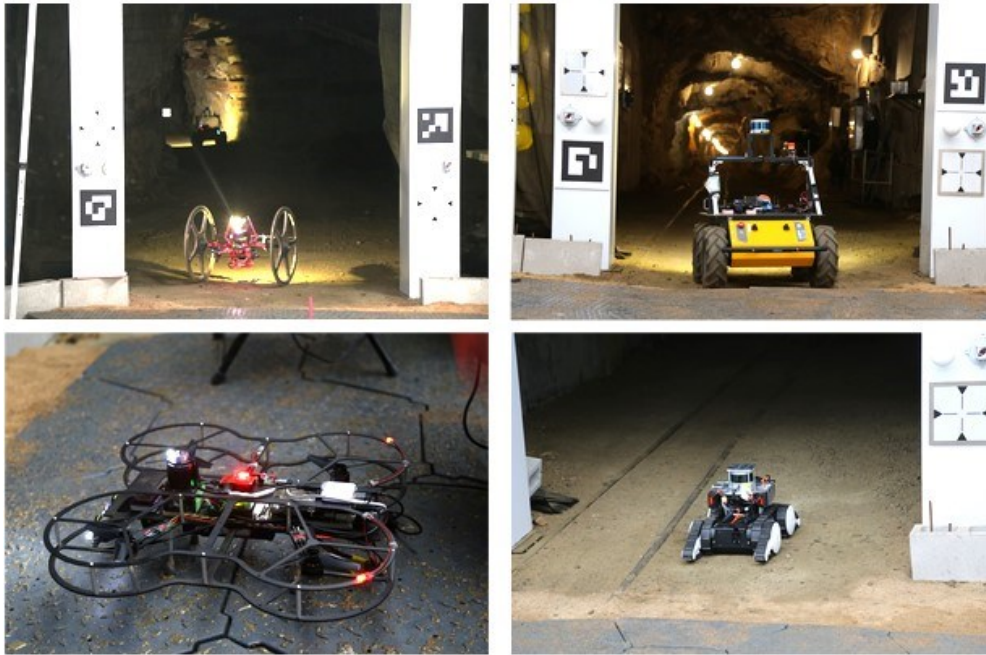
Figure 6-61: Four heterogeneous mobility platforms deployed at the STIX event. Clockwise from top left:: Rollocoper (with Husky in the course), Husky, Flipper and Scout.
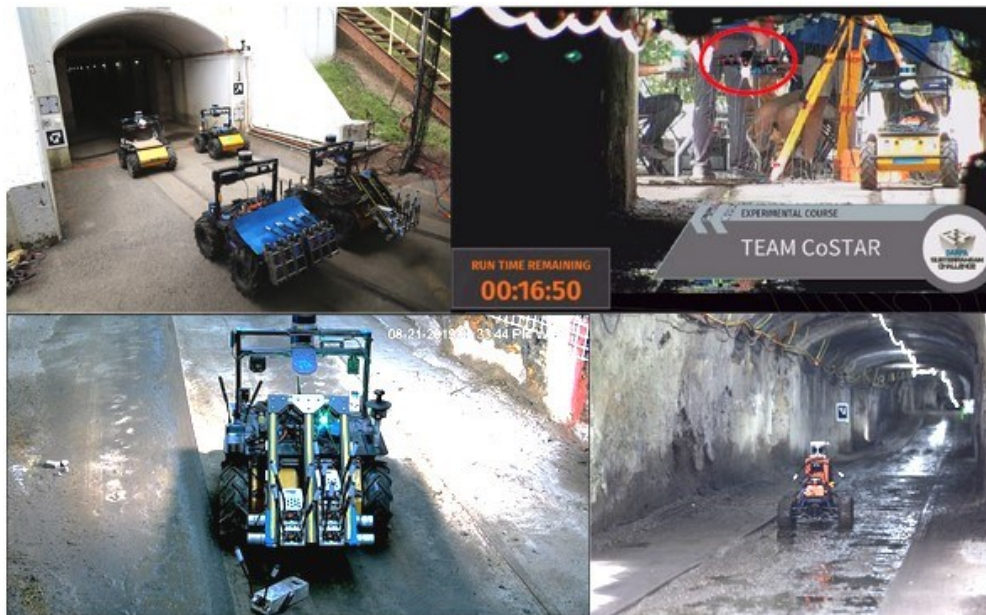
Figure 6-62: Robot team deployed at the Tunnel Circuit event. Top Left: Four Huskies at the Staging Area, Top Right: Drone deployed at the Experimental Mine, Bottom Left: Husky deploying a communication node, Bottom Right: RC car deployed at the Experimental Mine.

communication nodes are deployed from the robots to build a backbone network, covering the areas near the mine entrance and extend the reach of base station for faster data retrieval. We detected 16 artifacts during our four runs of the Tunnel Circuit, leading to a circuit score of 11 and the second-place finish among 11 teams (Table 6-7).
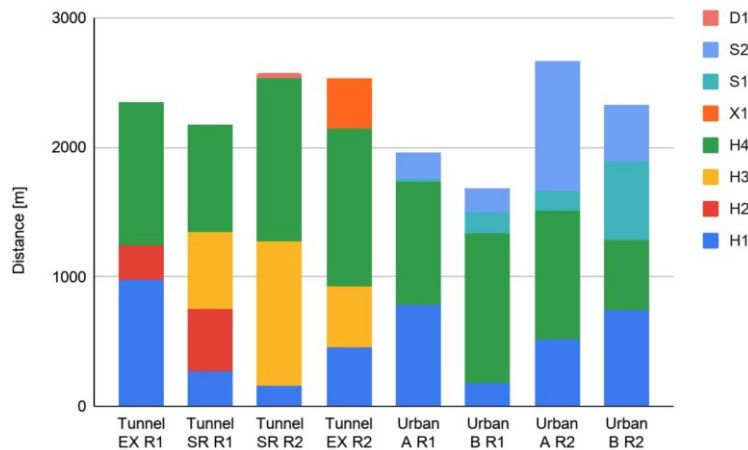
Figure 6-63: Driving distance statistics during the Tunnel and Urban Circuits. Prefixes refer to different robot types: D Drone, H Husky (wheeled robot), S Spot (legged robot), X XMax (1/5 scale RC car).

Table 6-7: Number of scored points for each competition run.

Circuit	Tunnel				Urban			
Run	SR R1	SR R2	EX R1	EX R2	A R1	A R2	B R1	B R2
Run scores	4	7	2	4	5	7	4	9
Course scores	7		4		7		9	
Circuit scores	11				16			
Circuit rank	2nd				1st			
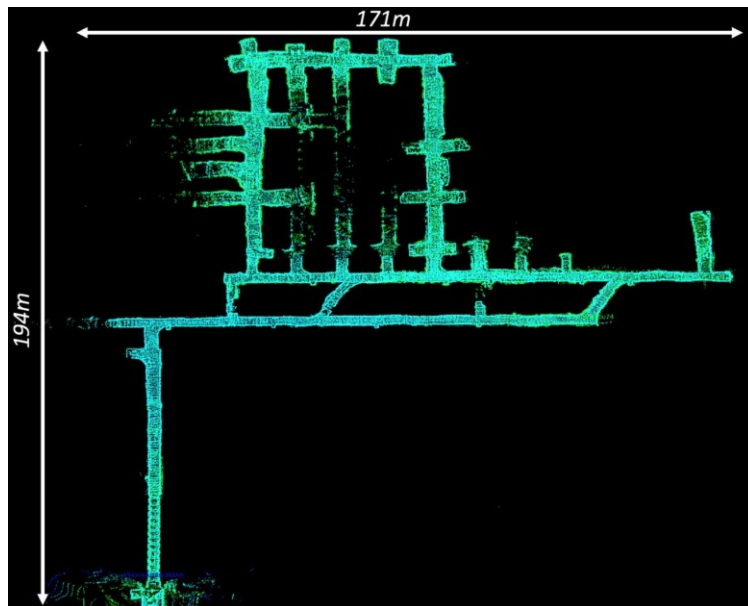
Figure 6-64: SLAM point cloud map from a single Husky robot run in the Safety Research run of the Tunnel Circuit. The robot starts from the bottom left, and completes the top loop in a clockwise direction.

Challenges: During the Tunnel Circuit event, we faced many real-world challenges which contributed to improve our system toward the next Circuit events. The flat featureless walls of the EX course affected our localization performance which was purely LiDAR-based as of the Tunnel Circuit. This motivated the development of multi-modal method (Section 5 and Section 6). Multi-robot operations in a commdegraded environment also posed challenges to our networking system. Based on the analysis of the Tunnel experience, we carefully redesigned the inter-robot networking protocol and deployed it in the Urban Circuit (Section 10). The drone traveled 35 m in 43 seconds before it experienced critical

state estimation error due to poor lighting. To eliminate this single-point failure in the future flights, we put more efforts on multi-modal sensing and parallel estimation (Section 5).

6.10.2.3. Urban Circuit

Environment: The Urban Circuit took place in February 2020 at the Satsop Business Park in Elma, WA. The unfinished power plant in the park was chosen for the place of the second circuit event where the robots were exposed to challenges from urban structures. The two courses, Alpha and Beta, covers two floors of the power plant with size around $90 \times 90 \times 15$ m^3. There are many small rooms and narrow corridors divided by thick walls that prevent direct wireless communications.

Robots: Team CoSTAR staged seven robots and deployed four of them during this event (Figure 6-65), including the newly introduced Boston Dynamics Spot quadruped robots (Spot 1 and 2). The other two robots are Clearpath Husky (Husky 1 and 4) with major upgrades in onboard electronics and sensor stack. All robots are deployed in each run, acting in the vanguard and supporting roles based on the assignment, their location, and time of the mission. One Spot was dedicated to climbing stairs to explore the floor at a different level.
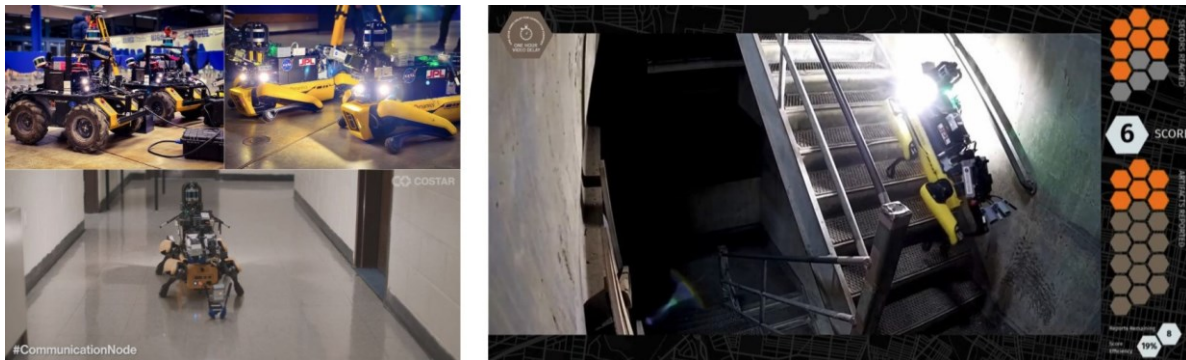
Figure 6-65: Robot team deployed at the Urban Circuit event. Left: Robot fleet and communication node deployment, Right: A snapshot of Spot stair climbing (DARPA TV).

**Performance**: We detected 25 artifacts during our four runs of the Urban Circuit, leading to a circuit score of 16 and the first-place finish among 10 teams (Table 6-7). Figure 6-66 shows a multi-robot map generated at the Beta course, including details on scored artifacts at multiple levels and at the furthest extent of exploration. The four-robot team traversed a combined total of 2.3 km (Figure 6-63), including a large closed loop by the two husky robots around the central round structure. The video in [18] depicts Spot robots exploring the multi-level courses autonomously.

Figure 6-67 shows the breakdown of scoring in the two highest scoring runs of the Urban competition, summarizing the reasons for not scoring the remaining artifacts. In addition to the artifacts missed due to the robot not reaching the artifact locations (Figure 6-66), we missed artifacts due to the limited field of view of the sensory suite on the robots (Figure 6-66) and other challenges in the artifact detection pipeline.

Challenges: Overall, the Team CoSTAR's system showed significant improvement from the Tunnel Circuit. Nonetheless, the circuit identified numerous ongoing challenges calling for further development. These development areas include: improved depth and breadth of coverage, enhanced sensor field-of-views for artifact detection, aerial robot developments, autonomous fault recovery, and careful attention to comm node placement/configuration to maximize wireless link quality for fast data retrieval.
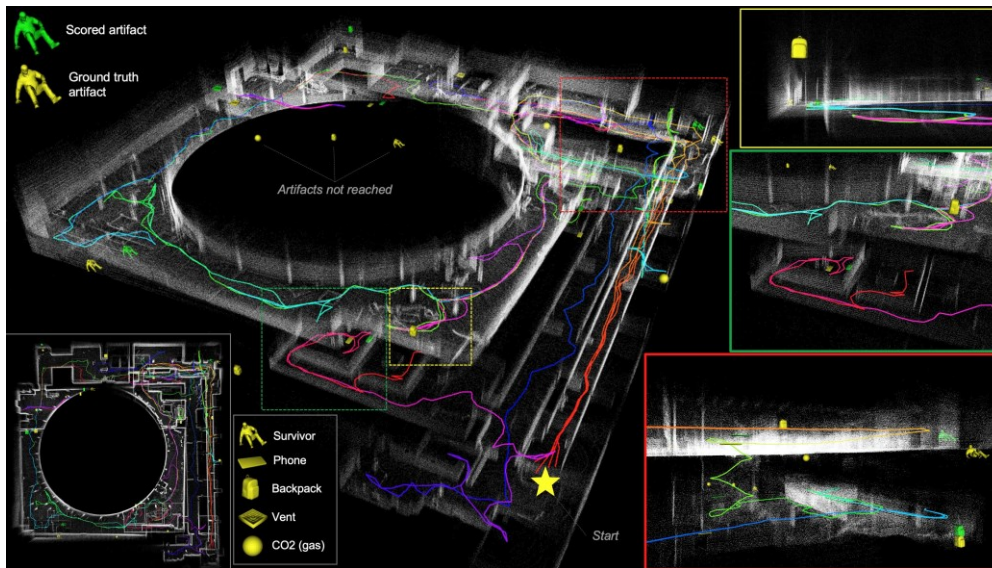
Figure 6-66: Multi-robot map, trajectories, scored artifacts and ground truth artifacts. All robots start from the star on the bottom right with trajectory colors cycling from red through yellow to blue and back to red based on distance travelled. RED inset shows multi-level exploration and scoring (upper-level survivor and lower-level backpack) by Spot1 with a stair descent (green part of trajectory). GREEN inset shows the furthest extent of lower-level exploration where a cell phone was scored by Spot1. YELLOW inset shows an instance of an unscored artifact, where it is placed out of view of ground robots, requiring flight. Other unscored artifacts are seen in the center of the map where no robot arrived near to them.
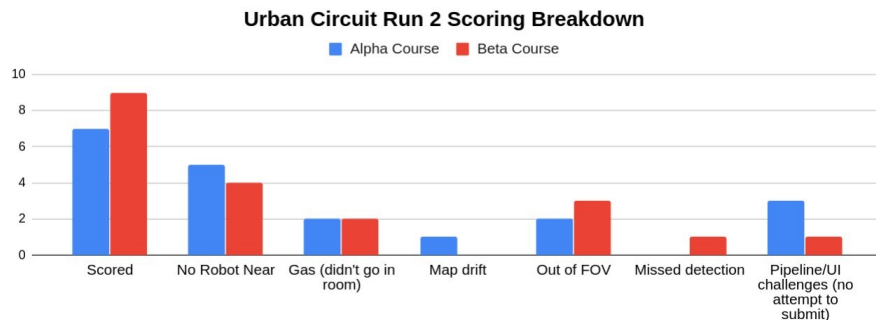
Figure 6-67: Scoring breakdown for the two highest-scoring Urban Circuit runs.

6.10.3. Self-Organized Cave Circuit

Environment overview: We self-organized a Cave Circuit event at the Valentine Cave of the Lava Beds National Monument, Tulelake, CA. The cave, a class of lava tubes, was formed from volcanic flows, and an active research target for the future lunar/Martian cave exploration [122, 123]. The length of the cave is approximately 300 m with an elevation change of 20 m. The tortuous and steep terrain in the cave limited the range of operations of wheeled platforms, hence tests were focused on the Spot quadrupeds (drone testing was not possible due to regulatory challenges).

Circuit Event Organization: The test was run as close to the competition setup as possible. The global frame and artifact locations were determine based on a pre-existing, high precision Faro scan of the cave. A fiducial gate was surveyed into the cave frame and used to calibrate the robots. All artifact classes other than CO_2 and Vent were placed throughout the cave, with a prioritization on ropes and helmets (the cave-specific artifacts).

Results: The cave demonstration was remarkable in that entire runs were fully-autonomous with zero human intervention: the operator only started the mission. Figure 6-68 shows a map from one such run. Spot traversed 400 m on average over 4 runs. Each mission was ended not by a time limit, but by the

full accessible environment being covered, with side passages limited by traversability hazards (very low ceilings, cliffs). The videos of the cave demonstration are available at [19, 20, 21].
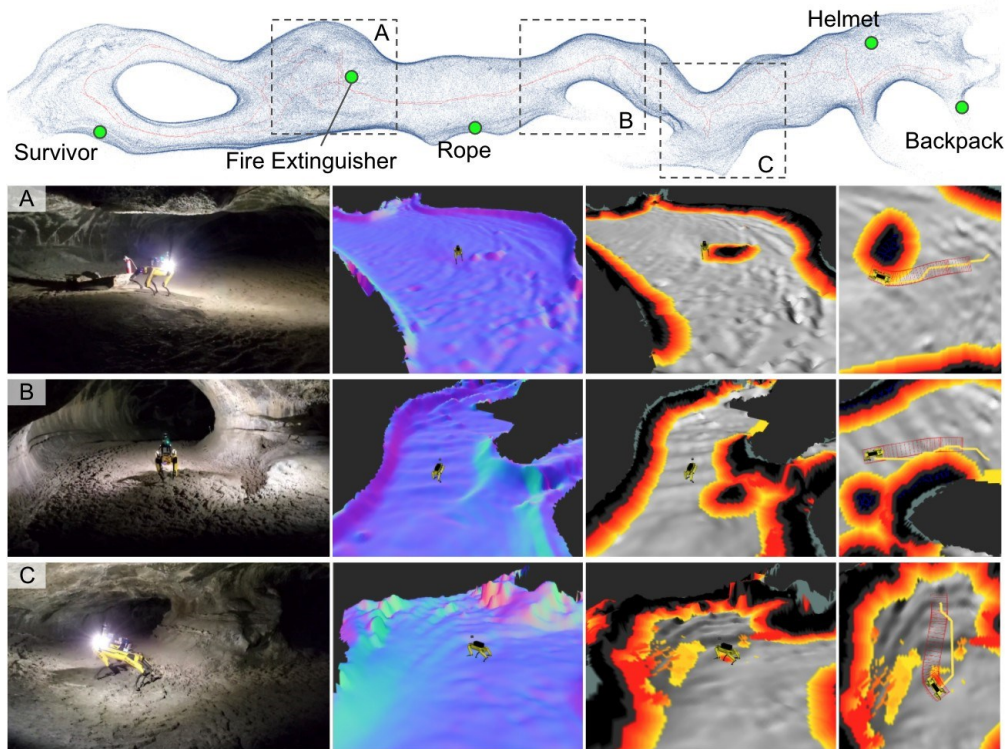
Figure 6-68: A pointcloud map from the SLAM module and traversability maps during autonomous exploration in the Valentine Cave at Lava Beds National Monument, Tulelake, CA.

6.11. Lessons Learned

At the time of submission, NeBula's uncertainty-aware and perception-aware principles are implemented in a number of modules throughout our autonomy solution. The module interactions have been tightly codesigned and joint probability distributions across some of the modules are incorporated to bolster the overall system's resiliency. This uncertainty-aware architecture is verified through intensive field testing campaigns using heterogeneous platforms with different variations of mobility, sensing, and computing capabilities. We observed that the joint perception-planning approach brought resiliency to the system behaviors in challenging real-world environments, where uncertainty is ubiquitous. This section summarizes the lessons learned from developing and fielding the NeBula autonomy solution.

6.11.1. Heterogeneous system design and integration

Designing a system with heterogeneous robots is a non-trivial task. Accomplishing the objectives of complex real-world operations (such as the one in the SubT) with constraints on time, resources/cost, robot size, weight, power, etc., can be too difficult or impossible for a single robot. This calls for multi-robot solutions. An important lesson learned and a major future direction is: "It is critical to have principled tools that can translate the design choices to overall mission metrics". These design choices range from the selection of type and number of robots to the selection of sensors, instruments, and algorithms, to the type of wires and connectors, and batteries. As some concrete examples that our team has encountered: "A slight change in the weight (and hence operation time) of one single robot" or "selection of a specific wire that can slightly affect the data traffic", can have a significant effect on the overall aggregated performance of the robot team and mission metrics. There are 100s if not thousands of such design parameters and choices (both in HW and SW), which calls for systematic tools to quickly abstract them and translate them to high-level mission metrics.

An important observation is that for the fast-paced development of a very large autonomy architecture for a multi-robot system, the architecture should be highly modular and adaptive. Since the architecture must incorporate robots' heterogeneous capabilities (mobility, sensing, and compute), appropriate abstractions need to be implemented to operate robots in a unified framework. We have performed many iterations of the architecture redesign as our entire system capabilities grow. A key lesson learned is that integration testing at a regular interval is essential to maintain the stability of such a growing system. Team CoSTAR has organized monthly virtual and physical integration demonstrations with competition-like set-ups. Regular testing enforces the new module to comply with the system interaction rules, ensuring functionality despite constant augmentations by multiple subteams throughout the development. Regular performance tracking also allows us to understand the current technology state and highlights the next domain to be studied.

6.11.2. Resilient state estimation

In challenging real-world robotic operations, perceptually-degradation is common, and state estimation can suffer from deterioration of sensor measurements and estimation quality. In addition, physical systems are exposed to the risk of sensor failures that are made prevalent by frequent field testing. These failures are difficult to model in many cases, yet systems must be able to react to these uncertain events to ensure system stability is not lost. One key lesson from our experience is to let the system predict a failure and quickly adapt to it. We observed that adding redundancy (e.g., HeRO at Section 5) in a principled way shows a lot of potentials to improve the resiliency of an odometry system by incorporating multi-modal sensors and algorithms. HeRO's built-in health check mechanism allows for preliminary detection of various types of failures and adapting the system to mitigate the effect. This proactive approach has been effective in our field tests and circuit events, providing the foundation to support high-level autonomous behaviors.

Another critical observation is on "how and when to trust the sensor models". Following NeBula's philosophy of uncertainty-aware predictive planning, the planner needs to be able to predict the joint distributions over the system's future actions and estimated states. To predict the future performance, we divide unknowns into "known unknowns" and "unknown unknowns". Known unknowns refer to uncertainties that can be reasonably modeled using probability distribution functions. Unknown unknowns refer to unmodeled uncertainties resulting from unexpected events in the system operation. To be resilient and robust to these uncertainties, we have observed that a cascaded framework (like HeRO) of loosely-coupled and tightly-coupled layers is promising. The cascaded framework first copes with unknown unknowns, by relying on a loosely-coupled layer and checking the consensus across different sensory modalities to detect anomalies and reject faulty estimation channels. Once left with inliers, it handles "known unknowns" by tightly fusing the estimation channels using their predicted probabilistic models.

6.11.3. Large-scale positioning and mapping

The SLAM design and deployment efforts presented in this paper highlight the importance of using complementary sensor information for localization and mapping. In complex environments, various sensors have their own advantage and disadvantages. For example, wheel-encoder-based odometry or visual odometry provides a useful source of information in long corridors where LiDAR scan matching is subject to drift; IMU data allows for accurate short-term relative rotation estimation while history-based scan matching can resolve longer-term displacement estimation. This need to fuse heterogeneous sensors also emphasizes the importance of a flexible SLAM framework where one can easily define and fuse sensor data when available. In this sense, the use of a factor graph framework reduced the integration efforts and allowed us to design a unified SLAM back-end that can be easily reconfigured. The importance of developing a reconfigurable framework is further exacerbated by the desire of running our SLAM solution on a heterogeneous set of platforms (e.g., robots with different sensor suites and different computational capabilities), which demanded our framework to be sensor agnostic (e.g.,

adjust to different sensors with minimal parameter tuning) and reconfigurable (e.g., enable and disable sensors to fuse via configuration files).

While having a reliable odometry solution is critical in large-scale mapping, even the most accurate odometry systems accumulate error over long distances across extreme terrains. This remarks the importance of loop closures to keep the localization errors bounded. However, when it comes to complex, large-scale environments, with perceptually-degraded conditions, a key lesson learned is that loop closure needs to be incorporated in a resilient manner into the overall framework. Computational constraints will limit the ability to search the map history and find correct loop closures in a reasonable time. Even after loop closures are found, it is crucial to maintain multiple hypotheses or at least remove incorrect loop closures resulting from perceptual aliasing. In this paper, we observed that *graph-based outlier rejection* (e.g., a variation of [54]) is helpful in filtering some of the incorrect hypotheses. This family of methods rely on approximate max clique solvers for consistency maximization, which becomes computationally expensive due to the size and density of the SLAM graphs in competition settings. Unfortunately, they often fail to select inlier loop closures, inducing "jumps" in the robot trajectory when the solver is stuck in suboptimal maximal cliques. Future work includes improving loop closure detection (e.g., prioritizing the most informative loop closures, using different sensors for place recognition) and adopting more recent methods for outlier rejection based on graduated non-convexity.

Computational aspects can be also improved by sharing the workload across robots. Centralized multi-robot SLAM methods require increasing computational resources for larger teams of robots. Adopting a distributed SLAM system can improve scalability and reduce communication bandwidth. In general, distributing the overall computation across various robots (based on their capabilities) can better scale to large teams of robots.

An important lesson learned is: Augmenting geometric information with semantics can increase the resiliency of the SLAM system. For instance, incorporating semantic information such as intersections, stairs, manmade objects in the graph can increase the robustness of the loop closures. Further, identifying a set of stairs in the environment provides a readily usable prior on the geometry of the stairs; similarly, identifying doors provides actionable information for navigation. Metric-semantic mapping is an active research area and a tight integration of geometric, semantic (and physical) reasoning has the potential to improve the robustness and accuracy of the map built by the robots.

Finally, while this section is concerned with localizing the robots and building a map, the quality of the map reconstruction is highly affected by the trajectories covered by the robots. Following NeBula's uncertaintyaware planning perspective, performing active loop closures to reduce the uncertainty in the robot location has a major impact on the SLAM accuracy. Active loop closures can be enabled by guiding robots to rendezvous points to create inter-robot measurements or by visiting parts of the environment that have unambiguous detection signatures. Towards this goal, quantifying and actively reducing uncertainty is crucial and is a fundamental trait of the NeBula framework. Active localization and mapping go beyond loop closures, and tightly couples perception, action, and communication.

Uncertainty-aware traversability analysis: Navigating over perceptually-degraded challenging terrains requires a radical departure from systems designed to operate in known environments with clear landmarks and easily distinguishable obstacles. Designed to detect complex geometric hazards at various scales, traversability analysis highly depends on the quality of local mapping and state estimation. As such, an important lesson has been that accounting for the "perception uncertainty" in planning is a key to building a reliable traversability system operating on challenging terrains and perceptual conditions. We learned that multi-fidelity mapping approaches (similar to the one presented in Section 8) improve the balance between computational constraints and accuracy in the presence of degraded state estimation and sensor measurement uncertainty. Uncertainty-aware estimation trusts and accumulates measurements in the world belief based on measurements' accuracy and quality. Using this world belief, the traversability layer precisely quantifies the perception-aware traversability risks and costs when negotiating challenging terrains. Finally, a critical lesson in traversability algorithm

design and development is constant field testing: The presented uncertainty-aware approach has been field-hardened in over 100 field test sites with diverse traversabilitystressing elements.

6.11.4. Scalable belief-space global planning

Global planning for area coverage and exploration behaviors is one of the modules where the awareness of uncertainty plays a critical role in achieving high performance in the real world. We remark several key dilemmas encountered while developing and testing the global planner, related to uncertainty representation and uncertainty-aware decision making: i) scalability vs. information fidelity in world belief representation, ii) planning horizon vs. planning time for each receding-horizon planning episode, and iii) the consistency of plans for smooth motions vs. resiliency to sudden changes in world belief over time. We learned that hierarchical approaches (similar to the ones described in Section 9) have the potential to address the above challenges. Our method, PLGRIM, leverages i) hierarchical IRMs, ii) longer-horizon, higher resolution POMDP solvers with manageable computation load, and iii) receding horizon planning with resiliency logic. However, those are still open problems. An important future direction is "quick online adaptation" of parameters that balance the environment scales and complexity with the computing system and sensor limitations. Another important open problem is related to encoding and capturing a more accurate and reliable representation of the high-dimensional world belief.

6.11.5. Semantic understanding and artifact detection

Detecting objects and understanding the semantics of the environment in perceptually-degraded subterranean settings is a challenging task. In the DARPA subterranean challenge, artifacts have multiple signatures, ranging from visual, thermal, auditory to gas-based, and radio-based artifacts. These various signatures and payload constraints (size, weight, power, etc.) on different heterogeneous platforms call for a method that assesses the value of adding various sensors and sensing modalities to each vehicle. Further, the choice and configuration of each sensor on each robot have a significant impact on the scoring performance (see Section 7). For example, for artifacts that can be detected visually, the salient camera parameters include field of view, reliability, image quality, resolution, and frame rate. Hence an important lesson has been that the artifact collection system needs a tight co-design of software and hardware. This includes the whole pipeline from the sensors, cables, to the processors and algorithms. For example, a change in a USB hub or cable can significantly impact the choices of other hardware and algorithms by removing certain data chocking elements in the pipeline. A related unexpected failure mode (which was occurred in one of our competitions) at the system level was sensor data transfer and communication, caused by both USB driver and networking bandwidth limitations. Correcting this problem required a thorough analysis of the hardware configuration, including the development and testing of custom driver software by our team.

The second major lesson was related to data. While the existing standard object detection datasets are quite large and diverse, learning to detect objects in the perceptually-degraded environments (e.g., variable lighting and with obscurants), such as the ones in the DARPA subterranean challenge-like environments, are still out-of-distribution in relation to mainstream datasets.

Finally after these trade-offs, there are still many limitations in the perception side of the artifact detection architecture. So the third, and the most important, lesson learned is that the planning and perception for artifact detection need to be tightly co-designed. In other words, active perception is required where the planner needs to take actions that compensate for perception shortcomings. Examples of such actions are: (i) executing local search maneuvers where the robot sweeps the larger parts of the scene with it sensors to compensate for its limited field of view, (ii) actively getting closer to certain targets or making measurements from various angles to increase the detection confidence. This mode might also include deciding which robot and which sensor should gather more information to increase the confidence. It also includes (iii) changing perception pipeline parameters such as the camera resolution, input rate, etc. to handle computational constraints by focusing and limiting the attention of the system on the important parts of the input channel.

Active perception for semantic understanding is highly open area, with a lot of future work in these domains.

6.11.6. Bandwidth-aware communication system design

Communications between computational units (e.g. ROS nodes) should ideally take into account the predicted available bandwidth in the link whether that link is on the same computer, via a high-speed Ethernet, a larger wired network, or radio/wireless. We took a number of successful steps in this direction: i) separating inter-agent (ROS 2) and intra-agent (ROS 1) communications, ii) using different QoS settings for different classes of topics, iii) monitoring inter-robot communications and estimated bandwidth, and iv) monitoring intra-robot communications. As future multiagent projects move away from ROS 1 and towards ROS 2 (or another middleware/communication solution) the same principles apply. We see that there is a need for continued improvements and autonomy in routing and QoS systems to optimally use communication resources in these future systems.

Another important lesson learned is that due to the communication-degraded nature of the subterranean environments, the planner needs to support and improve the communication and multi-robot networking performance by dropping communication nodes at the optimal locations and by actively carrying (mulling) data using mobile robots between the various nodes. Hence, aligned with NeBula's philosophy, (1) taking networking uncertainties into account, (2) evaluating and predicting the potential value of the communicated information, and (3) co-designing the planning system and networking system are that critical observations to increase the robustness and performance of the overall multi-robot robot networking system in communication-degraded environments.

6.11.7. Supervised autonomy to full autonomy

Achieving mission success depends heavily on the mission-level autonomy from both single and multi-robot perspectives. This is especially the case in contexts such as the SubT Challenge where large robot teams must intelligently coordinate themselves under strict communication, time, and resource constraints to explore and map km-scale environments and find objects of interest.

Closer to the course entrance a communication link with the human supervisor can be established. Thus the system must be capable of autonomously balancing between deeper exploration, operational risk, the value of the collected onboard information, and the cost of bringing the systems closer to the surface for the data retrieval. A key lesson learned is that even when robots are close to the course entrance and a communication link with the human supervisor is established, with a large heterogeneous multi-robot team, a single human supervisor becomes a bottleneck in the control loop due to excessive cognitive workloads of the supervisor. Hence, for successful operations, NeBula's mission executive and Copilot assistant are designed to support such tasks by adjusting the system autonomy levels, gradually delegating human tasks where the human is viewed as a resource, and providing suitable instructions and feedback to reduce the cognitive load of the single supervisor. Integral to the effort is maintaining a world belief that can be easily interpreted by the system or supervisor, and trigger behaviors or sequences of actions that bring the system closer towards achieving mission completion.

However, there is a lot of future research in this area. Our ongoing efforts have been focusing on some of these areas, including efficient ways of specifying more complex tasks and missions, balancing human-machine task distribution, planning using semantic information, and scheduling under uncertainty in task execution and future event occurrence.

6.11.8. Simulator-based development

The development of our system was greatly accelerated by the use of different computer simulation environments, discussed herein. The challenges inherent to real-world robotics in uncertain and fully autonomous settings pose tremendous risks to naive robots and algorithms in the early stages of development. Taking development into a simulation and out of hardware has afforded us numerous opportunities to pursue and achieve high-risk-high-gain algorithmic strategies. Many safety-critical features are difficult to test with physical hardware. By carefully modeling different fleet and hardware

configurations, we were able to develop, test, and eventually deploy our heterogeneous multi-robot team in the real world, with optimal networking, hardware, and software payloads. Although simulators offer an enormous benefit to robotic systems development, there are significant differences between simulations and real-world system which must be accounted for. It is important to understand simulator limitations and always perform proper validation and testing on physical hardware platforms.

6.12. Conclusion

Team CoSTAR's approach to the DARPA Subterranean Challenge lies in our autonomy solution, NeBula (Networked Belief-aware Perceptual Autonomy), which emphasizes resilience and intelligent decision making through uncertainty-awareness. NeBula has led to 2nd and 1st place in DARPA Subterranean Challenge's Tunnel (in 2019) and Urban (in 2020) competitions, respectively. When dealing with exploration and operation in unknown environments, uncertainty is inherent to all decisions. As the main principle, NeBula focuses on quantifying and taking advantage of uncertainty at multiple levels of our autonomy stack, including state estimation, mapping, traversability, planning, communications, and other state domains. We combine these technologies in a synergistic way, which examines the interaction between interrelated modules.

During this competition we have and hope to continue to demonstrate autonomous exploration in extreme environments on multiple platforms (including wheeled, legged, and aerial). Solving this problem remains of paramount interest in a wide range of applications, especially when it comes to missions to explore unknown planetary bodies beyond our home planet. We believe the uncertainty-aware and platform-agnostic nature of most NeBula components is a step towards resilient and safe robotic autonomy solutions in unknown and extreme environments with both single and multi-robot systems.

6.13. Glossary: Acronyms

APE Absolute Position Error
AUV Autonomous Underwater Vehicle
BPMN Business Modelling Process Notation
BRM belief roadmap
CHORD Collaborative High-bandwidth Operations with Radio Droppables
CIO Contact-Inertial Odometry
Comm Communication
ConOps Concept of Operations
CoSTAR Collaborative SubTerranean Autonomous Robots
CNN Convolutional Neural Network
CVaR Conditional Value-at-Risk
DARPA Defense Advanced Research Projects Agency
DLT Direct Linear Transform
EdgeTPU Edge Tensor Processing Unit
FGA Flat Ground Assumption
FIRM Feedback-based Information Roadmap
FOV Field of View
FPS Frames Per Second
GCP Global Coverage Planning
GESTALT Grid-based Estimation of Surface Traversability Applied to Local Terrain
GICP Generalized Iterative Closest Point
GO-LLC Geometric-Only LiDAR Loop Closures
GNSS Global Navigation Satellite System
GPS Global Positioning System

GPU Graphical Processing Unit

GTSAM Georgia Tech Smoothing and Mapping

HeRO Heterogeneous and Resilient Odometry Estimator

HFE Hierarchical Frontier-based Exploration **IMU** Inertial Measurement Unit **iSAM2** incremental Smoothing and Mapping

IRM Information RoadMap(p30,31 dups)

JPL Jet Propulsion Laboratory

LAMP Large-scale Autonomous Mapping and Positioning

LCP Local Coverage Planner

LIO LiDAR-Inertial Odometry

LION LiDAR-Inertial Observability-aware Navigation for vision-denied environments

LO Lidar Odometry

LOCUS Lidar Odometry for Consistent operations in Uncertain Settings

MAV Micro Aerial Vehicle

MDC Motion Distortion Correction

MER Mars Exploration Rover

MIKE Multi-robot Interaction assistant for unKnown cave Environments (aka 'Copilot', 'Copilot MIKE')

MPC Model Predictive Control

MSL Mars Science Laboratory

MSR Mars Sample Return

NBV Next-Best-View

NeBula Networked Belief-aware Perceptual Autonomy

NCDS NeBula Communications Deployment System

NDB NeBula Diagnostics Board

NPCC NeBula Power and Computing Core

NSP NeBula Sensor Package

PLGRIM Probabilistic Local and Global Reasoning on Information roadMaps

POMCP Partially Observable Monte Carlo Planning

POMDP Partially Observable Markov Decision Process

QoS Quality of Service

RA-LLC Range-Aided LiDAR Loop Closures

RC Remote Control

RF Radio Frequency

RHC Receding Horizon Control

RIO RaDAR-Inertial Odometry

RRT Rapidly-exploring Random Trees

QP Quadratic Programming

ROAMS Rover Analysis Modeling and Simulation

ROS Robot Operating System

RSSI Received signal strength indication

SLAM Simultaneous Localization and Mapping

SLAP Simultaneous Localization and Planning

SMAP Simultaneous Mapping and Planning

SOG Sum of Gaussians

STEP Stochastic Traversability Evaluation and Planning

STIX SubT Integration Exercise

TIO Thermal-Inertial Odometry

TRACE Traceable Robotic Activity Composer and Executive

UAV Unmanned Aerial Vehicle

UWB Ultra Wide-Band

VIO Visual-Inertial Odometry
VO Visual Odometry
WIO Wheel-Inert

6.14. References

[1]   E. Yurtsever, J. Lambert, A. Carballo, and K. Takeda, "A survey of autonomous driving: Common practices and emerging technologies," IEEE Access, vol. 8, pp. 58443–58469, 2020.

[2]   H. Balta, J. Bedkowski, S. Govindaraj, K. Majek, P. Musialik, D. Serrano, K. Alexis, R. Siegwart, and G. De Cubber, "Integrated data management for science & a fleet of search-and-rescue robots," *Journal of Field Robotics*, vol. 34, no. 3, pp. 539–582, 2017.

[3]   Y. Qin, S. A. Pedram, S. Feyzabadi, M. Allan, A. J. McLeod, J. W. Burdick, and M. Azizian, "Temporal segmentation of surgical sub-tasks through deep learning with multiple data sources," in *2020 IEEE International Conference on Robotics and Automation (ICRA)*, 2020, pp. 371–377.

[4]   P. F. Santana, J. Barata, and L. Correia, "Sustainable robots for humanitarian demining," *International Journal of Advanced Robotic Systems*, vol. 4, no. 2, p. 23, 2007.

[5]   J. C. Kinsey, R. M. Eustice, and L. L. Whitcomb, "A survey of underwater vehicle navigation: Recent advances and new challenges," in *IFAC Conference of Manoeuvering and Control of Marine Craft*, vol. 88. Lisbon, 2006, pp. 1–12.

[6]   T. Sasaki, K. Otsu, R. Thakker, S. Haesaert, and A. Agha-mohammadi, "Where to map? iterative rover-copter path planning for mars exploration," *IEEE Robotics and Automation Letters*, vol. 5, no. 2, pp. 2123–2130, 2020.

[7]   M. Bajracharya, M. W. Maimone, and D. Helmick, "Autonomy for mars rovers: Past, present, and future," *Computer*, vol. 41, no. 12, pp. 44–50, 2008.

[8]   J. Ford, H. Jones, K. Sharif, and R. Whittaker, "Technologies enabling the exploration of lunar pits," *International Symposium on Artificial Intelligence, Robotics and Automation in Space (i-SAIRAS)*, 2020.

[9]   T. Fedschun, "Thailand cave rescue clears hurdle, divers reach passageway that may lead to youth soccer team," https://www.nytimes.com/2018/07/12/world/asia/thailand-cave-rescue-seals.html, 2018.

[10]   T. Vejpongsa, "Flooding complicates cave search for thai soccer team," https://apnews.com/article/be65215e881540fc9e63d2edfe98efa1, 2018.

[11]   G. Cushing, "Candidate cave entrances on mars," *Journal of Cave and Karst Studies, Vol. 74, p. 33-47*, vol. 74, pp. 33–47, 04 2012.

[12]   S. B. Kesner, J.-S. Plante, P. J. Boston, T. Fabian, and S. Dubowsky, "Mobility and power feasibility of a microbot team system for extraterrestrial cave exploration," in *Proceedings 2007 IEEE International Conference on Robotics and Automation*, 2007, pp. 4893–4898.

[13]   T. Titus, J. Wynne, P. Boston, P. De Le´on, C. Demirel-Floyd, H. Jones, F. Sauro, K. Uckert, A. AghaMohammadi, E. Alexander Jr, J. Ashley, A. Azua, L. Chiao, G. Cushing, J. Dedecker, A. Fair´en, A. Frumkin, J. De Waele, G. Harris, and R. Romo, "Science and technology requirements to explore caves in our solar system," *White Paper*, 07 2020.

[14]   V. Stamenkovi´c, L. Beegle, K. Zacny, D. Arumugam, P. Baglioni, N. Barba, J. Baross, M. Bell, R. Bhartia, J. Blank, *et al.*, "The next frontier for planetary and human exploration," *Nature Astronomy*, vol. 3, no. 2, pp. 116–120, 2019.

[15]   T. Touma, J. G. Blank, M. F. Ginting, C. Patterson, and A. Agha, "Mars Dogs: Biomimetic Robots for the Exploration of Mars, from its Rugged Surface to its Hidden Caves," in *AGU Fall Meeting*, 2020. [16] DARPA, "DARPA Subterranean Challenge," https://www.subtchallenge.com, 2018.

[16]   CoSTAR Team, "NeBula Autonomy Highlights in Team CoSTAR's Multi-robot Operations in the DARPA Subterranean Challenge Tunnel and Urban Circuit," https://youtu.be/O4SZxZmQh-Q, NASA-JPL, 2020.

[17] ——, "Autonomous Spot Demonstration in Urban Environment," https://youtu.be/VitjPLRdY8g, NASA-JPL, 2020.

[18] ——, "Robotic Exploration over Extreme Terrain in Martian-Analog Lava Tubes," https://youtu.be/ ApyPiZK d0, NASA-JPL, 2020.

[19] ——, "Search for Life: NASA JPL Explores Martian-Like Caves," https://youtu.be/qTW-dbZr4U8, NASA-JPL, 2021.

[20] ——, "Mars Dogs: AI Powered Autonomous Robot Concept for Mars," https://youtu.be/ A8YR2J6KTxU, NASA-JPL, 2020.

[21] DARPA, "DARPA Subterranean Challenge: Scoring Metrics," https://www.subtchallenge.com/ resources/SubT Challenge Finals Rules.pdf, 2021.

[22] A. Santamaria-Navarro, R. Thakker, D. D. Fan, B. Morrell, and A. Agha-mohammadi, "Towards resilient autonomous navigation of drones," *Proceedings of the International Symposium on Robotics Research*, 2019.

[23] M. Palieri, B. Morrell, A. Thakur, K. Ebadi, J. Nash, A. Chatterjee, C. Kanellakis, L. Carlone, C. Guaragnella, and A. Agha-mohammadi, "LOCUS A Multi-Sensor Lidar-Centric Solution for HighPrecision Odometry and 3D Mapping in Real-Time," *IEEE Robotics and Automation Letters*, vol. 6, no. 2, pp. 421–428, 2020.

[24] A. Kramer, C. Stahoviak, A. Santamaria-Navarro, A. Agha-mohammadi, and C. Heckman, "Radarinertial ego-velocity estimation for visually degraded environments," in *IEEE International Conference on Robotics and Automation (ICRA)*, 2020, pp. 5739–5746.

[25] S. Fakoorian, M. Palieri, A. Santamaria-Navarro, C. Guaragnella, D. Simon, and A. Agha-mohammadi, "Maximum correntropy Kalman filter for orientation estimation with application to lidar inertial odometry," in *ASME 2020 Dynamic Systems and Control Conference*, 2020. To appear.

[26] S. Fakoorian, A. Santamaria-Navarro, B. T. Lopez, D. Simon, and A. Agha-mohammadi, "Towards Robust State Estimation by Boosting the Maximum Correntropy Criterion Kalman Filter with Adaptive Behaviors," 2021. To appear.

[27] A. Tagliabue, J. Tordesillas, X. Cai, A. Santamaria-Navarro, J. How, L. Carlone, and A. Aghamohammadi, "LION: Lidar-Inertial Observability-aware Navigator for vision-denied environments," in *17th International Symposium on Experimental Robotics*, 2021, p. To appear.

[28] T. Lew, T. Emmei, D. D. Fan, T. Bartlett, A. Santamaria-Navarro, R. Thakker, and A.-a. Aghamohammadi, "Contact inertial odometry: Collisions are your friends," *Proceedings of the International Symposium on Robotics Research*, 2019.

[29] P. Furgale, J. Rehder, and R. Siegwart, "Unified temporal and spatial calibration for multi-sensor systems," in *IEEE/RSJ Int. Conf. on Intelligent Robots & Systems*, 2013.

[30] J. Rehder, J. Nikolic, T. Schneider, T. Hinzmann, and R. Siegwart, "Extending kalibr: Calibrating the extrinsics of multiple IMUs and of individual axes," in *Proc. IEEE Conf. on Robotics and Automation*, 2016.

[31] A. Millane and Z. Taylor, "evo: Python package for the evaluation of odometry and slam." https://github.com/ethz-asl/lidar align, 2019.

[32] P. Autopilot, "PX4FLOW Smart Camera," https://docs.px4.io/master/en/sensor/px4flow.html, 2021.

[33] R. Mur-Artal and J. D. Tard´os, "ORB-SLAM2: an open-source SLAM system for monocular, stereo and RGB-D cameras," *IEEE Transactions on Robotics*, vol. 33, no. 5, pp. 1255–1262, 2017.

[34] Qualcomm Technologies, Inc., "Machine Vision SDK," https://developer.qualcomm.com/software/machinevision-sdk.

[35] A. Rosinol, M. Abate, Y. Chang, and L. Carlone, "Kimera: an open-source library for real-time metricsemantic localization and mapping," in *IEEE International Conference on Robotics and Automation (ICRA)*, 2020.

[36]   S. Khattak, F. Mascarich, T. Dang, C. Papachristos, and K. Alexis, "Robust thermal-inertial localization for aerial robots: A case for direct methods," in *2019 International Conference on Unmanned Aircraft Systems (ICUAS)*, 2019, pp. 1061–1068.

[37]   T. Shan, B. Englot, D. Meyers, W. Wang, C. Ratti, and D. Rus, "Lio-sam: Tightly-coupled lidar inertial odometry via smoothing and mapping," in *IEEE/RSJ IROS*, 2020.

[38]   H. Ye, Y. Chen, and M. Liu, "Tightly coupled 3d lidar inertial odometry and mapping," in *2019 International Conference on Robotics and Automation (ICRA)*, 2019, pp. 3144–3150.

[39]   W. Hess, D. Kohler, H. Rapp, and D. Andor, "Real-time loop closure in 2d lidar slam," in *2016 IEEE International Conference on Robotics and Automation (ICRA)*, 2016, pp. 1271–1278.

[40]   A. Segal, D. Haehnel, and S. Thrun, "Generalized-icp." in *Robotics: science and systems*, vol. 2. Seattle, WA, 2009, p. 435.

[41]   J. Zhang and S. Singh, "LOAM: Lidar odometry and mapping in real-time," in *In Robotics: Science and Systems, vol. 2*, 2014, p. 9.

[42]   E. Nelson, "Berkley localization and mapping," *https://github.com/erik-nelson/blam*, october 2016.

[43]   C. Forster, L. Carlone, F. Dellaert, and D. Scaramuzza, "Imu preintegration on manifold for efficient visual-inertial maximum-a-posteriori estimation," *Robotics: Science and Systems (RSS)*, 2015.

[44]   ——, "On-manifold preintegration theory for fast and accurate visual-inertial navigation," *IEEE Transactions on Robotics*, pp. 1–18, 2015.

[45]   F. Dellaert, "Factor graphs and gtsam: A hands-on introduction," Georgia Institute of Technology, Tech. Rep., 2012.

[46]   M. Kaess, H. Johannsson, R. Roberts, V. Ila, J. J. Leonard, and F. Dellaert, "iSAM2: Incremental smoothing and mapping using the bayes tree," *The International Journal of Robotics Research*, vol. 31, no. 2, pp. 216–235, 2012.

[47]   N. Gelfand, L. Ikemoto, S. Rusinkiewicz, and M. Levoy, "Geometrically stable sampling for the ICP algorithm," in *Fourth International Conference on 3-D Digital Imaging and Modeling, 2003. 3DIM 2003. Proceedings.*, 2003, pp. 260–267.

[48]   S. Bonnabel, M. Barczyk, and F. Goulette, "On the covariance of ICP-based scan-matching techniques," in *2016 American Control Conference (ACC)*, 2016, pp. 5498–5503.

[49]   K. Ebadi, Y. Chang, M. Palieri, A. Stephens, A. Hatteland, E. Heiden, A. Thakur, N. Funabiki, B. Morrell, S. Wood, L. Carlone, and A. Agha-mohammadi, "LAMP: Large-Scale Autonomous Mapping and Positioning for exploration of perceptually-degraded subterranean environments," in *2020 International Conference on Robotics and Automation (ICRA)*, 2020.

[50]   A. Rosinol, M. Abate, Y. Chang, and L. Carlone, "Kimera: an open-source library for real-time metric-semantic localization and mapping," in *2020 IEEE International Conference on Robotics and Automation (ICRA)*, 2020, pp. 1689–1696.

[51]   K. Ebadi, M. Palieri, S. Wood, P. Curtis, and A. Agha-mohammadi, "DARE-SLAM: DegeneracyAware and Resilient Loop Closing in Perceptually-Degraded Environments," *Journal of Intelligent and Robotic Systems*, vol. 102, no. 1, pp. 1–25, 2021.

[52]   S. Choudhary, L. Carlone, C. Nieto, J. Rogers, H. I. Christensen, and F. Dellaert, "Distributed mapping with privacy and communication constraints: Lightweight algorithms and object-based models," *The International Journal of Robotics Research*, vol. 36, no. 12, pp. 1286–1311, 2017.

[53]   J. G. Mangelson, D. Dominic, R. M. Eustice, and R. Vasudevan, "Pairwise consistent measurement set maximization for robust multi-robot map merging," in *2018 IEEE International Conference on Robotics and Automation (ICRA)*, 2018, pp. 2916–2923.

[54]   P.-Y. Lajoie, B. Ramtoula, Y. Chang, L. Carlone, and G. Beltrame, "Door-slam: Distributed, online, and outlier resilient slam for robotic teams," *IEEE Robotics and Automation Letters*, vol. 5, no. 2, pp. 1656–1663, 2020.

[55]   N. Funabiki, B. Morrell, J. Nash, and A. Agha-mohammadi, "Range-aided pose-graph-based slam: Applications of deployable ranging beacons for unknown environment exploration," *IEEE Robotics and Automation Letters*, vol. 6, no. 1, pp. 48–55, 2020.

[56]   A. akbar Agha-mohammadi, E. Heiden, K. Hausman, and G. Sukhatme, "Confidence-rich grid mapping," *The International Journal of Robotics Research*, vol. 38, no. 12-13, pp. 1352–1374, 2019. [Online]. Available: https://doi.org/10.1177/0278364919839762

[57]   E. Heiden, K. Hausman, G. S. Sukhatme, and A.-a. Agha-mohammadi, "Planning high-speed safe trajectories in confidence-rich maps," in *2017 IEEE/RSJ International Conference on Intelligent Robots and Systems (IROS)*, 2017, pp. 2880–2886.

[58]   B. Morrell, M. Palieri, N. Funabiki, A. Thakur, A. Agha, and J. G. Blank, "Robotic localization and multi-sensor, semantic 3d mapping for exploration of subsurface voids," in *AGU Fall Meeting 2020*. AGU, 2020.

[59]   E. Terry, X. Lei, B. Morrell, S. Daftry, and A. Agha-mohammadi, "Object and gas source detection with robotic platforms in perceptually-degraded environments," in *RSS Workshop: Robots in the Wild: Challenges in Deploying Robust Autonomy for Robotic Exploration*, 2020.

[60]   V. Agrawal, "Ground up design of a multi-modal object detection system," Master's thesis, Carnegie Mellon University, Pittsburgh, PA, December 2019.

[61]   V. L. Orekhov and T. H. Chung, "The DARPA subterranean challenge: A synopsis of the circuits stage," *Submitted to the Journal of Field Robotics*, 2021.

[62]   J. Redmon and A. Farhadi, "Yolov3: An incremental improvement," *arXiv preprint arXiv:1804.02767*, 2018.

[63]   A. Bochkovskiy, C.-Y. Wang, and H.-Y. M. Liao, "Yolov4: Optimal speed and accuracy of object detection," *arXiv preprint arXiv:2004.10934*, 2020.

[64]   Y. Xiong, H. Liu, S. Gupta, B. Akin, G. Bender, P.-J. Kindermans, M. Tan, V. Singh, and B. Chen, "Mobiledets: Searching for object detection architectures for mobile accelerators," *arXiv preprint arXiv:2004.14525*, 2020.

[65]   B. Ramtoula, A. Caccavale, G. Beltrame, and M. Schwager, "Msl-raptor: A 6dof relative pose tracker for onboard robotic perception," *arXiv 2012.09264*, 2020.

[66]   R. Arandjelovic, P. Gronat, A. Torii, T. Pajdla, and J. Sivic, "Netvlad: Cnn architecture for weakly supervised place recognition," in *Proceedings of the IEEE conference on computer vision and pattern recognition*, 2016, pp. 5297–5307.

[67]   R. Thakker, N. Alatur, D. D. Fan, J. Tordesillas, M. Paton, K. Otsu, O. Toupet, and A. Aghamohammadi, "Autonomous off-road navigation over extreme terrains with perceptually-challenging conditions," in *17th International Symposium on Experimental Robotics (ISER)*, 2020.

[68]   D. D. Fan, K. Otsu, Y. Kubo, A. Dixit, J. Burdick, and A.-A. Agha-Mohammadi, "Step: Stochastic traversability evaluation and planning for safe off-road navigation," *arXiv preprint arXiv:2103.02828*, 2021.

[69]   H. Kalita, S. Morad, A. Ravindran, and J. Thangavelautham, "Path planning and navigation inside off-world lava tubes and caves," in *2018 IEEE/ION Position, Location and Navigation Symposium (PLANS)*, 2018, pp. 1311–1318.

[70]   R. J. L´eveill´e and S. Datta, "Lava tubes and basaltic caves as astrobiological targets on earth and mars: a review," *Planetary and Space Science*, vol. 58, no. 4, pp. 592–598, 2010.

[71]   S. Ahmad, Z. N. Sunberg, and J. S. Humbert, "Apf-pf: Probabilistic depth perception for 3d reactive obstacle avoidance," in *2021 American Control Conference (ACC)*, 2021, pp. 32–39.

[72]   T. Hines, K. Stepanas, F. Talbot, I. Sa, J. Lewis, E. Hernandez, N. Kottege, and N. Hudson, "Virtual surfaces and attitude aware planning and behaviours for negative obstacle navigation," *IEEE Robotics and Automation Letters*, vol. 6, no. 2, pp. 4048–4055, 2021.

[73]   M. Himmelsbach, F. V. Hundelshausen, and H.-J. Wuensche, "Fast segmentation of 3d point clouds for ground vehicles," in *Intelligent Vehicles Symposium (IV), 2010 IEEE*, 2010, pp. 560–565.

[74]   D. D. Fan, J. Nguyen, R. Thakker, N. Alatur, A. Agha-mohammadi, and E. A. Theodorou, "Bayesian learning-based adaptive control for safety critical systems," in *2020 IEEE International Conference on Robotics and Automation (ICRA)*, 2020, pp. 4093–4099.

[75]   D. D. Fan, A. Agha-mohammadi, and E. A. Theodorou, "Deep learning tubes for tube mpc," *Robotics Science and Systems (RSS)*, 2020.

[76]   S.-K. Kim∗, A. Bouman∗, G. Salhotra, D. D. Fan, K. Otsu, J. Burdick, and A. Agha-mohammadi, "PLGRIM: Hierarchical value learning for large-scale exploration in unknown environments," in *Proceedings of the International Conference on Automated Planning and Scheduling (ICAPS)*, vol. 31, 2021.

[77]   A. Bouman∗, M. Ginting∗, N. Alatur∗, M. Palieri, D. D. Fan, T. Touma, T. Pailevanian, S. Kim, K. Otsu, J. Burdick, and A. Agha-Mohammadi, "Autonomous Spot: Long-Range Autonomous Exploration of Extreme Environments with Legged Locomotion," in *2020 IEEE/RSJ International Conference on Intelligent Robots and Systems (IROS)*, 2020.

[78]   L. Kaelbling, M. Littman, and A. Cassandra, "Planning and acting in partially observable stochastic domains," *Artificial Intelligence*, vol. 101, pp. 99–134, 1998.

[79]   J. Pineau, G. Gordon, and S. Thrun, "Point-based value iteration: An anytime algorithm for POMDPs," in *International Joint Conference on Artificial Intelligence (IJCAI)*, Acapulco, Mexico, 2003, pp. 1025–1032.

[80]   A. Agha-mohammadi, S. Agarwal, S.-K. Kim, S. Chakravorty, and N. M. Amato, "SLAP: Simultaneous localization and planning under uncertainty via dynamic replanning in belief space," *IEEE Transactions on Robotics*, vol. 34, no. 5, pp. 1195–1214, 2018.

[81]   S.-K. Kim, R. Thakker, and A.-A. Agha-Mohammadi, "Bi-directional value learning for risk-aware planning under uncertainty," *IEEE Robotics and Automation Letters*, vol. 4, no. 3, pp. 2493–2500, 2019.

[82]   L. P. Kaelbling and T. Lozano-P´erez, "Planning in the know: Hierarchical belief-space task and motion planning," in *Workshop on Mobile Manipulation, IEEE Intl. Conf. on Robotics and Automation*, 2011.

[83]   S.-K. Kim, O. Salzman, and M. Likhachev, "POMHDP: Search-based belief space planning using multiple heuristics," in *Proceedings of the International Conference on Automated Planning and Scheduling (ICAPS)*, vol. 29, 2019, pp. 734–744.

[84]   A. Agha-mohammadi, S. Chakravorty, and N. Amato, "FIRM: Sampling-based feedback motion planning under motion uncertainty and imperfect measurements," *International Journal of Robotics Research (IJRR)*, vol. 33, no. 2, pp. 268–304, 2014.

[85]   M. L. Littman, A. R. Cassandra, and L. P. Kaelbling, "Learning policies for partially observable environments: Scaling up," in *Machine Learning Proceedings 1995*. Elsevier, 1995, pp. 362–370.

[86]   D. Silver and J. Veness, "Monte-Carlo planning in large POMDPs," in *Advances in neural information processing systems*, 2010, pp. 2164–2172.

[87]   S.-K. Kim, R. Thakker, and A. Agha-Mohammadi, "Bi-directional value learning for risk-aware planning under uncertainty," *IEEE Robotics and Automation Letters*, vol. 4, no. 3, pp. 2493–2500, 2019.

[88]   K. Otsu, S. Tepsuporn, R. Thakker, T. S. Vaquero, J. A. Edlund, W. Walsh, G. Miles, T. Heywood, M. T. Wolf, and A. Agha-mohammadi, "Supervised autonomy for communication-degraded subterranean exploration by a robot team," in *IEEE Aerospace Conference*, 2020.

[89]   H. Umari and S. Mukhopadhyay, "Autonomous robotic exploration based on multiple rapidly-exploring randomized trees," in *IEEE/RSJ International Conference on Intelligent Robots and Systems (IROS)*, 2017, pp. 1396–1402.

[90]   M. F. Ginting, K. Otsu, J. A. Edlund, J. Gao, and A. Agha-mohammadi, "CHORD distributed data-sharing via hybrid ros 1 and 2 for multi-robot exploration of large-scale complex environments," *IEEE Robotics and Automation Letters*, 2021.

[91]   M. F. Ginting, T. Touma, J. A. Edlund, A. Buscicchio, , K. Otsu, and A. Agha, "Deployable Mesh Network for Enabling Reliable Communication from within Subsurface Voids to the Planetary Surface," in *AGU Fall Meeting*, 2020.

[92]   T. S. Vaquero, M. Saboia da Silva, K. Otsu, M. Kaufmann, J. A. Edlund, and A. Agha-mohammadi, "Traversability-aware signal coverage planning for communication node deployment in planetary cave exploration," in *Artificial Intelligence, Robotics and Automation in Space*, 2020.

[93]   M. Kaufmann, T. S. Vaquero, G. J. Correa, K. Otsu, M. F. Ginting, G. Beltrame, and A. Aghamohammadi, "Copilot mike: An autonomous assistant for multi-robot operations in cave exploration," in *2021 IEEE Aerospace Conference*. IEEE, 2021, pp. 1–9.

[94]   M. Fox and D. Long, "Pddl+: Modelling continuous time-dependent effects," 2002.

[95]   J. Benton, A. Coles, and A. Coles, "Temporal planning with preferences and time-dependent continuous costs," in *Proceedings of the International Conference on Automated Planning and Scheduling*, vol. 22, no. 1, 2012.

[96]   J.-P. de la Croix, G. Lim, J. Vander Hook, A. Rahmani, G. Droge, A. Xydes, and C. Scrapper Jr, "Mission modeling, planning, and execution module for teams of unmanned vehicles," in *Unmanned Systems Technology XIX*, vol. 10195. International Society for Optics and Photonics, 2017, p. 101950J.

[97]   I. D. Miller, F. Cladera, A. Cowley, S. S. Shivakumar, E. S. Lee, L. Jarin-Lipschitz, A. Bhat, N. Rodrigues, A. Zhou, A. Cohen, and et al., "Mine tunnel exploration using multiple quadrupedal robots," *IEEE Robotics and Automation Letters*, vol. 5, no. 2, p. 2840–2847, 2020.

[98]   F. Jenelten, T. Miki, A. E. Vijayan, M. Bjelonic, and M. Hutter, "Perceptive locomotion in rough terrain – online foothold optimization." *IEEE Robotics and Automation Letters*, vol. 5, no. 4, p. 5370–5376, 2020.

[99]   S. Jung, H. Lee, D. H. Shim, and A. akbar Agha-mohammadi, "Robust collision-free lightweight aerial autonomy for unknown area exploration," *arXiv preprint arXiv:2103.05798*, 2021.

[100]   L. Meier, D. Honegger, and M. Pollefeys, "Px4: A node-based multithreaded open source robotics framework for deeply embedded platforms," in *2015 IEEE international conference on robotics and automation (ICRA)*, 2015, pp. 6235–6240.

[101]   D. D. Fan, R. Thakker, T. Bartlett, M. B. Miled, L. Kim, E. Theodorou, and A.-a. Agha-mohammadi, "Autonomous hybrid ground/aerial mobility in unknown environments," in *2019 IEEE/RSJ International Conference on Intelligent Robots and Systems (IROS)*. IEEE, 2019, pp. 3070–3077.

[102]   A. Kalantari and M. Spenko, "Modeling and performance assessment of the hytaq, a hybrid terrestrial/aerial quadrotor," *IEEE Transactions on Robotics*, vol. 30, no. 5, pp. 1278–1285, 2014.

[103]   CoSTAR Team, "Rollocopter early versions," https://youtu.be/XHltzQv3cTE, NASA-JPL, 2018.

[104]   A. Agha-mohammadi, A. Tagliabue, S. Schneider, B. Morrell, M. Pavone, J. Hofgartner, I. A. Nesnas, R. B. Amini, A. Kalantari, A. Babuscia, *et al.*, "The shapeshifter: a morphing, multiagent, multi-modal robotic platform for the exploration of titan (preprint version)," *arXiv preprint arXiv:2003.08293*, 2020.

[105]   A. Tagliabue, S. Schneider, M. Pavone, and A. a. Agha-mohammadi, "Shapeshifter: A multi-agent, multi-modal robotic platform for exploration of titan," in *2020 IEEE Aerospace Conference*, 2020, pp. 1–13.

[106]   A. Kalantari, T. Touma, L. Kim, R. Jitosho, K. Strickland, B. T. Lopez, and A. Agha-Mohammadi, "Drivocopter: A concept hybrid aerial/ground vehicle for long-endurance mobility," in *2020 IEEE Aerospace Conference*, 2020, pp. 1–10.

[107]   H. C. Choi, I. Wee, M. Corah, S. Sabet, T. Kim, T. Touma, D. H. Shim, and A. Agha-mohammadi, "BAXTER: Bi-modal Aerial-Terrestrial Hybrid Vehicle for Long-endurance Versatile Mobility," *International Symposium on Experimental Robotics*, 2020.

[108]   S. Sabet, M. Poursina, P. E. Nikravesh, P. Reverdy, and A.-A. Agha-Mohammadi, "Dynamic modeling, energy analysis, and path planning of spherical robots on uneven terrains," *IEEE Robotics and Automation Letters*, vol. 5, no. 4, pp. 6049–6056, 2020.

[109]   S. Sabet, A. Agha-Mohammadi, A. Tagliabue, D. S. Elliott, and P. E. Nikravesh, "Rollocopter: An energy-aware hybrid aerial-ground mobility for extreme terrains," in *IEEE Aerospace Conference*, 2019, pp. 1–8.

[110]   DARPA, "SubT Tech Repo," https://www.subtchallenge.world/models, 2018.

[111]   R. Chase and S. Kitchen, "How we won the DARPA SubT Challenge: Urban circuit virtual track," https://spectrum.ieee.org/darpa-subt-challenge-urban-circuit-virtual, 2020.

[112]   CoSTAR Team, "Scout tunnel experiment," https://www.youtube.com/watch?v=MdYXu ImXik, NASA-JPL, 2018.

[113]   M. Tranzatto, F. Mascarich, L. Bernreiter, C. Godinho, M. Camurri, S. M. K. Khattak, T. Dang,

[114]   V. Reijgwart, J. Loeje, D. Wisth, S. Zimmermann, H. Nguyen, M. Fehr, L. Solanka, R. Buchanan, M. Bjelonic, N. Khedekar, M. Valceschini, F. Jenelten, M. Dharmadhikari, T. Homberger, P. De Petris, L. Wellhausen, M. Kulkarni, T. Miki, S. Hirsch, M. Montenegro, C. Papachristos, F. Tresoldi, J. Carius, G. Valsecchi, J. Lee, K. Meyer, X. Wu, J. Nieto, A. Smith, M. Hutter, R. Siegwart, M. Mueller, M. Fallon, and K. Alexis, "CERBERUS: Autonomous legged and aerial robotic exploration in the tunnel and urban circuits of the DARPA subterranean challenge," *Submitted to the Journal of Field Robotics*, 2021.

[115]   J. Issacs, K. Knoedler, A. Herdering, M. Beylik, and H. Quintero, "Teleoperation for urban search and rescue applications," *Submitted to the Journal of Field Robotics*, 2021.

[116]   N. Hudson, F. Talbot, M. Cox, J. Williams, T. Hines, A. Pitt, B. Wood, D. Frousheger, K. L. Surdo,

[117]   T. Molnar, R. Steindl, M. Wildie, I. Sa, N. Kottege, K. Stepanas, E. Hernandez, G. Catt, W. Docherty, B. Tidd, B. Tam, S. Murrell, M. Bessell, L. Hanson, L. Tychsen-Smith, H. Suzuki, L. Overs, F. Kendoul, G. Wagner, D. Palmer, P. Milani, M. O'Brien, S. Jiang, S. Chen, and R. C. Arkin, "Heterogeneous ground and air platforms, homogeneous sensing: Team CSIRO data61's approach to the DARPA subterranean challenge," *Submitted to the Journal of Field Robotics*, 2021.

[118]   T. Rouček, M. Pecka, P. Cížek, T. Petříček, J. Bayer, V. Salanský, D. Heřt, M. Petrlík, T. Baca, V. Spurny, V. Krátky, P. Petráček, D. Baril, M. Vaidis, V. Kubelka, F. Pomerleau, J. Faigl, K. Zimmermann, M. Saska, T. Svoboda, and T. Krajník, "System for multi-robotic exploration of underground environments CTU-CRAS-NORLAB in the DARPA subterranean challenge," *Submitted to the Journal of Field Robotics*, 2021.

[119]   S. Scherer, V. Agrawal, G. Best, C. Cao, K. Cujic, R. Darnley, R. DeBortoli, E. Dexheimer, B. Drozd,

[120]   R. Garg, I. Higgins, J. Keller, D. Kohanbash, L. Nogueira, R. Pradhan, M. Tatum, V. K. Viswanathan, S. Willits, S. Zhao, H. Zhu, D. Abad, T. Angert, G. Armstrong, R. Boirum, A. Dongare, M. Dworman, S. Hu, J. Jaekel, R. Ji, A. Lai, Y. Hsuan Lee, A. Luong, J. Mangelson, J. Maier, J. Picard, K. Pluckter, A. Saba, M. Saroya, E. Scheide, N. Shoemaker-Trejo, J. Spisak, J. Teza, F. Yang, A. Wilson, H. Zhang, H. Choset, M. Kaess, A. Rowe, S. Singh, J. Zhang, G. A. Hollinger, and M. Travers, "Resilient and modular subterranean exploration with a team of roving and flying robots," *Submitted to the Journal of Field Robotics*, 2021.

[121]   M. T. Ohradzansky, E. R. Rush, D. G. Riley, A. B. Mills, S. Ahmad, S. McGuire, H. Biggie, K. Harlow, M. J. Miles, E. W. Frew, C. Heckman, and J. S. Humbert, "Multi-agent autonomy: Advancements and challenges in subterranean exploration," *Submitted to the Journal of Field Robotics*, 2021.

[122]   C.-L. Lu, C.-I. Huang, J.-T. Huang, C.-C. Hsu, P.-K. Chang, Z. L. Ewe, P.-J. Huang, Y.-Y. Huang, S.-C. Huang, P.-L. Li, B.-H. Wang, L.-S. Yim, S.-W. Huang, Z.-Y. Liu, M.-H. Bai, and H.-C. Wang, "A heterogeneous unmanned ground vehicle and blimp robot team for search and rescue using data-driven autonomy and communication-aware navigation," *Submitted to the Journal of Field Robotics*, 2021.

[123]   A. Dixit and J. Burdick, "The kinematics of tracked vehicles via the power dissipation method," 2020.

[124]   J. G. Blank, T. L. Roush, C. L. Stoker, A. Colaprete, S. Datta, U. Wong, M. Deans, T. Fong, R. Léveillé, D. E. Northup, *et al.*, "Planetary caves as astrobiology targets," in *AGU Fall Meeting 2018*. AGU, 2018.

[125]   J. G. Blank, A. Agha-mohammadi, E. R. J. Bell, D. A. Crown, M. B. J., C. J. Patterson, K. Uckert, and P. L. Whelley, "Volcanic caves as priority sites for astrobiology science," *A White Paper submitted to the Decadal Survey on Planetary Science & Astrobiology*, 2020.

7. Conclusion

In this PhD dissertation, we delve into the innovative developments across advanced manufacturing, origami-inspired solar panels and robotics across space exploration landscape.

The first paper introduces FRET (Flexible Reinforced Electronics Textile), a technology enabler for deployable, origami-inspired aerospace systems. By combining rigid-flex PCB electronics and Nomex®, FRET addresses design challenges, providing robustness and resilience for reliable lightweight origami-inspired deployable structures. The research has been targeting manufacturing and testing of the FRET prototypes, where traction test have been performed to evaluate the quality of the FRET's prototypes. Although the first results had shown room for improvement, especially on the bonding and the adhesive material selection, more work is on the way to validate material selection and bonding quality. The latest FRET samples can be seen in Figure 7-1. In future work, these samples will be tested in space-grade conditions such as ATOX contamination, UV radiation, and Thermo-vacuum.

Figure 7-1 FRET latest mechanical samples for material characterization.

Future work related to FRET includes investigation into applications that may benefit of FRET's unique electro-mechanical properties, such as: Astronaut's spacesuit, origami-inspired deployable antennas and integrated sensors into inflatable modules.

Moving on, the second paper presents SolarCube, an origami-inspired, lightweight solar panel designed for nanosatellites. Fueled by the innovative FRET technology, SolarCube achieves an exceptional stowed-to-deployed surface ratio, promising advancements in lightweight, efficient solar panels. At the time of writing, SolarCube is at TRL 4 (the latest SolarCube solar panel substrate can be seen in Figure 7-2), and a fully functional prototype is expected by the summer of 2024.
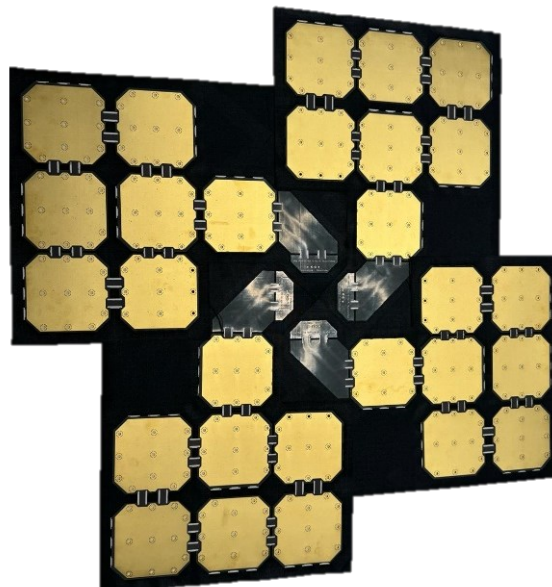

Figure 7-2 SolarCube prior to solarcells integration.

Although the author's main contribution to the development of SolarCube has been mainly focused in the development of the origami-inspired solar panel, in collaboration with Astradyne, a startup with the goal of transferring the FRET's technology into commercial applications, the other aspects of the SolarCube have been developed. In fact, a deployment system and a power distribution board are currently under development by Astradyne. FRET's technology has gained enough traction that two PhD doctorates are currently deeply investigating the modelling of FRET technology applied to origami-inspired applications. Future plans involve extensive testing, collaborations with launch providers, and in-orbit demonstrations of SolarCube by 2025.

The third paper focus on advancing the modelling of both FRET and SolarCube. For FRET modelling, the validation of key parameters in the PATRAN simulation environment involved a comparison with benchmark values derived from experimental traction tests on FRET samples. This validation process also incorporated a key performance index (KPI). Subsequently, the dynamic characteristics of SolarCube were explored by determining the first ten natural frequencies of the solar array, both in its closed and open configurations. The results revealed values within the anticipated range, aligning with the requirements specified in the user manual of the Ariane 5 spacecraft used as a reference. These analyses marked a significant advancement in modeling FRET, a challenging task given the limited prior studies on this technology. Future work, some of which is already in progress as shown in Figure 7-3, will focus on the unfolding dynamics of the SolarCube during deployment and its interaction with the deployment system.
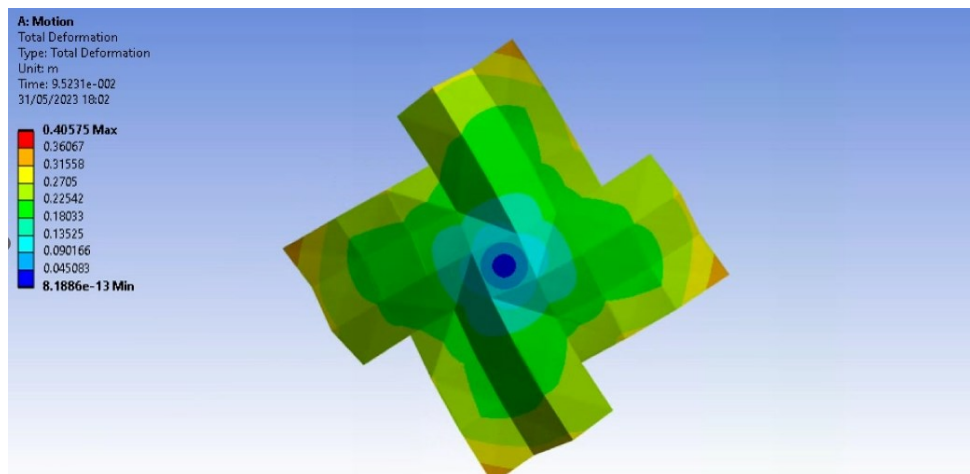

Figure 7-3 Modelling SolarCube solar array deployment using Ansys.

The forth paper highlights the author contribution in the development of the Electrical Ground Support Equipment (EGSE), also known as the "Blue Box", used for testing the Sampling Caching System of the Mars 2020 Perseverance rover. This modular EGSE system, deployed in various venues, proved vital in identifying and resolving anomalies, providing valuable insights for future implementations and reinforcing its role in the Verification and Validation (V&V) campaign. The paper presents circuit design, lesson learned and troubleshooting activities. In particular, the inductor compensation has been of particular interest for the author since many motor control anomalies were found to be related to this topic. In many scenarios, discrepancies between the behavior of the BlueBox and the Flight Controller were experienced. Future work will focus on improving the behavior of the motor controller to match the performance and behavior of the flight grade electronics.

Finally, the fifth paper discusses the research on autonomous robotics performed within the NASA-JPL Team CoSTAR achievements for the DARPA Subterranean Challenge, showcasing the NeBula autonomy solution. This uncertainty-aware framework has shown resilience and intelligent decision-

making capabilities. NeBula's platform-agnostic components offer promising solutions for autonomous exploration in extreme environments, with ongoing efforts focused on future missions and applications beyond our planet. The author contribution in this research has been mainly on the hardware side, focusing on the development of the embedded electronics and software for the CoSTAR robots. The challenges of designing electronics for heterogeneous platforms were overcome by using ROS (Robotic Operative System) also at the hardware level using the rosserial libraries. It is also interested to noted that, although these robots have been used for terrestrial applications, their applicability to the exploration of other celestial objects, such as Mars and the Moon remains valid.

Collectively, these papers contribute to the advancement of robotics technology, origami-inspired structures, and space exploration, showcasing innovations in manufacturing, deployable mechanisms, solar panels, testing equipment, and autonomy solutions. The future trajectory involves addressing challenges, refining designs, and pushing the boundaries of technology for practical applications in space exploration and robotics.

Among the proposed research topic, definitely the SolarCube shines for its innovativeness. In the context of the new space economy, SolarCube has indeed the potential to revolutionize the satellite space sector. Although the research has been focused on 3U CubeSats, the technology has the potential to be scaled up to bigger platform such as 6-12U CubeSat and even small satellites.
Future work in this research will focus on several key areas. Firstly, there will be an emphasis on further enhancing the modeling of origami deployable structures for space applications. This will involve delving deeper into the analysis of compatibility between flexible structures and electronic components such as flexible rigid PCBs, solar cells, or antennas. To achieve this, integrating the finite element Carrera Unified Formulation (CUF) with classical reduced degrees of freedom models will be explored. This integration will enable a more refined analysis of local behavior at critical points like folds and interface points with bonded rigid-flexible elements, while maintaining computational efficiency.

Additionally, controlled deployment methods will be investigated to improve system reliability and morphing capabilities. Experimental validation of the developed models will be conducted through test campaigns, including deployment tests of structures with origami or classic folding patterns, as well as cyclic thermal fatigue tests. By comparing the results of these tests with numerical simulations, the robustness of the numerical model will be enhanced, providing a predictive tool for complex behaviors in deployable structures. Overall, this future work aims to advance the understanding and reliability of origami deployable structures in space applications.